DOCTORAL THESIS

Experimental and Computational Magnetic Resonance Studies of Selected Rare Earth and Bismuth Complexes

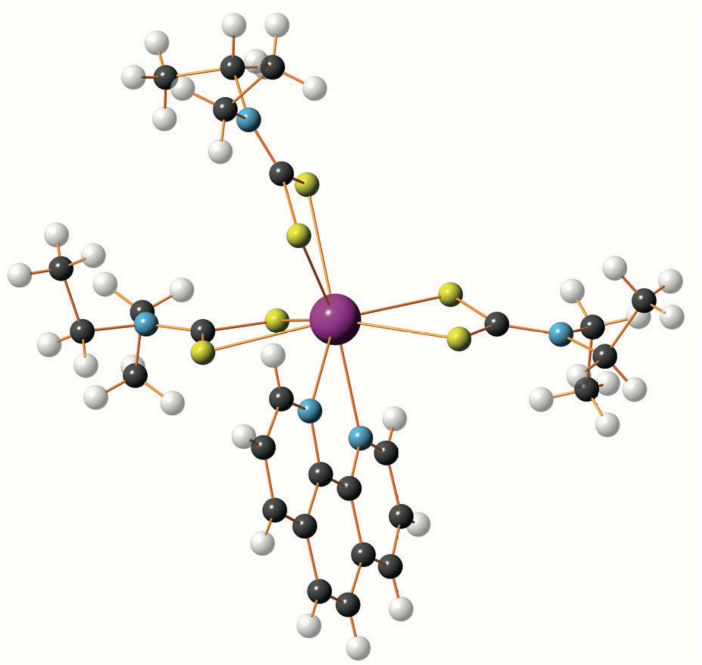

Vasantha Gowda

Chemistry of Interfaces (LTU)
NMR spectroscopy, Physics (UO)

This thesis is the result of a collaboration between Luleå University of Technology (LTU) and University of Oulu (UO) that aims toward a double degree

UNIVERSITY OF OULU

LULEÅ UNIVERSITY OF TECHNOLOGY

DOCTORAL THESIS

Experimental and Computational Magnetic Resonance Studies of Selected Rare Earth and Bismuth Complexes

VASANTHA GOWDA

Chemistry of Interfaces
Department of Civil, Environmental and Natural Resources Engineering
Luleå University of Technology
SWEDEN

and

NMR Research Unit, Faculty of Science
University of Oulu
FINLAND

CAMM
CENTRE OF ADVANCED MINING AND METALLURGY

OULU MINING SCHOOL

Opponent
Professor Guido Pintacuda
Institute of Analytical Sciences, France

Reviewers
Associate Professor Ulla Gro Nielsen
University of Southern Denmark, Denmark

Associate Professor Elina Inkeri Sievänen
University of Jyväskylä, Finland

Custos
Docent, Associate Professor Perttu Lantto
University of Oulu, Finland

Printed by Luleå University of Technology, Graphic Production 2017

ISSN 1402-1544
ISBN 978-91-7583-947-9 (print)
ISBN 978-91-7583-948-6 (pdf)

Luleå 2017

www.ltu.se

Abstract

The rare-earth elements (REEs) and bismuth, being classified as the 'most critical raw materials' (European Raw Materials Initiatives, 2017), have a high economic importance to the EU combined with a high relative supply risk. REEs are highly important for the evolving technologies such as clean-energy applications, high-technology components, rechargeable batteries, permanent magnets, electric and hybrid vehicles, and phosphors monitors.

This scientific research work aims at building a fundamental knowledge base concerning the electronic/molecular structure and properties of rare-earth element (REE) and bismuth complexes with dithiocarbamate (DTC) and 1,10-phenanthroline (PHEN) by employing state-of-the-art experimental techniques such as nuclear magnetic resonance (NMR) spectroscopy and X-ray diffraction (XRD) techniques together with *ab initio* quantum mechanical computational methods. This combination of methods has played a vital role in analysing the direct and significant effect of the heavy metal ions on the structural and magnetic resonance properties of the complexes, thereby, providing a framework of structure elucidation. This is of special importance for REEs, which are known to exhibit similar chemical and physical properties. The objectives of the work involve i) a systematic investigation of series of REE(III) as well as bismuth(III) complexes to get a profound understanding of the structure-properties relationship and ii) to find an appropriate theoretical modelling and NMR calculation methods, especially, for heavy metal systems in molecular and/or solid-state. This information can later be used in surface interaction studies of REE/bismuth minerals with DTC as well as in design and development of novel ligands for extraction/separation of metal ions.

The REE(III) and bismuth(III) complexes with DTC and PHEN ligands have all provided a unique NMR fingerprint of the metal centre both in liquid and solid phase. The solid-state ^{13}C and ^{15}N NMR spectra of the diamagnetic REE(III) and bismuth(III) complexes were in accord with their structural data obtained by single crystal XRD. The density functional theory (DFT) methods were used to get complementary and refined structural and NMR parameters information for all diamagnetic complexes in the solid-state. The relativistic contributions due to scalar and spin-orbit correlations for the calculated $^{1}H/^{13}C/^{15}N$ chemical shifts of REE complexes were analysed using two-component zeroth-order regular approximation (ZORA)/DFT while the 'crystal-lattice' effects on the NMR parameters were calculated by combining DFT calculations on molecular and periodic solid-state models. The paramagnetic REE complexes display huge differences in their ^{1}H and ^{13}C NMR spectral patterns. The experimental paramagnetic NMR (pNMR) chemical shifts, as well as the sizable difference of the ^{1}H and ^{13}C NMR shifts for these isoelectronic complexes, are well reproduced by the advanced calculations using *ab initio*/DFT approach. The accuracy of this approach is very promising for further applications to demanding pNMR problems involving paramagnetic *f*-block elements.

The results presented in this thesis demonstrate that a multidisciplinary approach of combined experimental NMR and XRD techniques along with computational modelling and property calculations is highly efficient in studying molecular complexes and solids containing heavy metal systems, such as rare-earths and bismuth.

Keywords: nuclear magnetic resonance spectroscopy, rare-earth elements, bismuth complexes, dithiocarbamates, X-ray diffraction, density functional theory, paramagnetic nuclear magnetic resonance

Acknowledgements

I would like to thank my principal supervisors Prof. Oleg N. Antzutkin (LTU) and Assoc. Prof. Perttu Lantto (UO); assistant supervisors Assoc. Prof. Anna-Carin Larsson (LTU) and Assoc. Prof. Ville-Veikko Telkki (UO) for giving me an opportunity to start my research career, for their encouragement and help in planning my research work, theoretical calculations and scientific discussions.

I am grateful to the reviewers of this thesis, Assoc. Prof. Ulla Gro Nielsen and Assoc. Prof. Elina Inkeri Sievänen for their valuable comments and finding many typos and mistakes in the texts.

This scientific research has been financed by Centre of Advanced Mining and Metallurgy (CAMM), Oulu Mining School (OMS), and Academy of Finland. The computational resources were provided by the Centre for Scientific Computing (CSC)-The Finnish IT center for science (Espoo, Finland).

I would like to thank Prof. Sven Öberg (LTU), Dr. Bipul Sarma (Tezpur University, India) Prof. Risto. S. Laitinen (UO), Prof. Alexander Ivanov (Russian Academy of Sciences), Prof. Juha Vaara (UO), Dr. Jiri Mares (UO), and Dr. Dinu Iuga for the scientific collaboration. I also want to thank Jonas Helmerius (LTU) for helping in placing orders for chemicals.
Dr. Anuttam Patra and family, Assoc. Prof. Faiz Ullah Shah, Dr. Andrei Filippov, Dr. Manish P Shimpi and family, Dr. Shubhankar Bhattacharyya, Dr. Rashi Gusain and all other department friends at LTU and Oulu are thanked for their direct or indirect help during my pursuit of PhD studies.

The administrative staffs both at LTU and UO have done a great amount of paperwork in making the Double Doctoral Program run smoothly.

My special thanks go to my dearest friend Ms. Veena Hegde for her constant encouragement and all the motivations she has given to me.

Thank you, Mom, Dad and brothers, for all your love, support, and inspiration. I couldn't have made it without you.

List of papers and manuscripts

The present thesis consists of an introductory part and the following original papers and manuscripts:

I. **V. Gowda**, B. Sarma, S. Öberg, V.-V. Telkki, A.-C. Larsson, P. Lantto, O. N. Antzutkin, *Structure Elucidation of an Yttrium Diethyldithiocarbamato-Phenanthroline Complex by X-ray Crystallography, Solid-state NMR and ab-initio Quantum Chemical Calculations.* European Journal of Inorganic Chemistry, **20**, 3278-3291 (2016). DOI: 10.1002/ejic.201600059

II. **V. Gowda**, R. S. Laitinen, V.-V. Telkki, A.-C. Larsson, O. N. Antzutkin, P. Lantto, *DFT calculations in the assignment of solid-state NMR and crystal structure elucidation of a lanthanum(III) complex with dithiocarbamate and phenanthroline.* Journal of Chemical Society, Dalton Transactions, **45**, 19473-19484 (2016). DOI: 10.1039/C6DT03705D

III. **V. Gowda**, J. Mareš, A.-C. Larsson, O. N. Antzutkin, V.-V. Telkki, J. Vaara, P. Lantto, *Ab initio calculation of ^{1}H and ^{13}C chemical shifts in paramagnetic Nd(III), Eu(III), Er(III), and Yb(III) complexes.* (Manuscript).

IV. **V. Gowda**, A.-C. Larsson, V.-V. Telkki, P. Lantto, O. N. Antzutkin, *Synthesis and structural investigations by NMR and DFT calculations of Bi(III) diethyldithiocarbamate complexes with phenanthroline and/or nitrate.* (Manuscript)

V. **V. Gowda**, B. Sarma, R. S. Laitinen, A.-C. Larsson, A. V. Ivanov, D. Iuga, P. Lantto, O. N. Antzutkin, *Structural insights into the polymorphism of bismuth(III) di-n-butyldithiocarbamate by X-ray diffraction, solid-state ($^{13}C/^{15}N$) CP-MAS NMR and DFT calculations, Solid-State ($^{13}C/^{15}N$) CP-MAS NMR, and DFT Calculations.* Polyhedron, **129**, 123-132 (2017). DOI: 10.1016/j.poly.2017.03.018

The author of this thesis participated in the planning of all the experimental as well as the quantum chemical calculations, in cooperation with the other authors, and carried out all the synthetic work, NMR and powder XRD experiments, and most of the computational work in Papers I–V. The single crystal XRD measurements were done by the co-authors. Practically, all the DFT calculations at the ZORA (SR and SO) levels of theory in Papers I and II and periodic DFT calculations in Papers I, II, IV, and V were done by the author. Some part of the correlated *ab initio* calculations of the pNMR chemical shifts in Paper III were done in collaboration with other authors. The analysis of the results in all Papers I–V was performed in collaboration with the other authors. The first versions of all manuscripts I-V, including the computational sections, were drafted by the author. The articles were revised many times and the final versions were prepared in cooperation with the other authors.

Abbreviations

ADF	Amsterdam Density Functional (software)
COSMO	conductor-like screening model
CSA	chemical shift anisotropy
CPMAS	cross-polarisation magic-angle-spinning
CI	configuration interaction (CI)
CASSCF	complete active space self-consistent field (theory)
DEDTC	diethyldithiocarbamate
DFT	density functional theory
DKH	Douglas-Kroll-Hess
DTC	dithiocarbamate
ECP	effective core potential
EPR	electron paramagnetic resonance
FID	free induction decay
GGA	generalized gradient approximations
GIPAW	gauge-including projector augmented wave
HF	Hartree-Fock (theory)
KS	Kohn-Sham (theory)
LDA	local density approximation
mDKS	matrix Dirac-Kohn-Sham (theory)
MP*n*	*n*th-order Moller-Plesset many body perturbation theory
*n*BuDTC	di-*n*-butyldithiocarbamate
NMR	nuclear magnetic resonance
PAS	principal axis system
PBE	Perdew-Burke-Ernzerhof
PHEN	1,10-phenanthroline
PT	perturbation theory
PW	plane wave
PXRD	powder X-ray diffraction
REE	rare earth elements
SO	spin-orbit (interaction)
SR	scalar relativistic
TZVP	triple-ζ valence plus polarisation
XRD	X-ray diffraction
WFT	wavefunction theory
ZORA	zeroth-order regular approximation (theory)

1 Introduction

This chapter introduces the area of research and its possible importance for the development of mineral industry as well as in academics. The chapter also contains the goals and objectives, research challenges and the research approach and methodology for this thesis.

1.1 Background

A group of elements called rare-earths (or REEs), as defined by the International Union of Pure and Applied Chemistry (IUPAC)[1], includes fifteen lanthanides (i.e., lanthanum to lutetium) plus scandium and yttrium. The REEs that we see on Earth today were born in a supernova explosion nearly ten billion years ago[2] (Table 1). In contrast to their name, REEs are not especially 'rare' (except for the radioactive promethium) but they account for about 10 parts per million (ppm) of the mass of all the elements found in the Earth's crust.[3,4] Despite billions of years being subjected to the physical extremes of geological processes such as repeated melting and solidifying, mountain formation, erosion, and immersion in sea water, geochemical separation of REEs into individual lanthanide minerals have only rarely progressed. This is a strong testament to the similarity of many of their physical and chemical properties (oxidation state, ionic radii, etc.).[5] The rare-earths never occur in pure forms but always together with other REEs in a variety of minerals having different concentrations of the individual REEs. However, the REE minerals can be split into two broad groups, i.e. minerals containing light REEs (LREE) (La to Gd) and heavy REE (HREE) (Tb to Lu, and Y). This classification is based on the electronic configuration of the individual REE, where the LREE have in common increasing unpaired *f*-electrons (0 to 7) and no 'paired' *f*-electrons whereas the HREE have 'paired' *f*-electrons. Scandium, due to its much smaller ionic radius, is generally not included as being either LREE or HREE.

REEs and Bismuth have been placed in the list of the most critical raw materials[6,7] (by European Raw Material Initiative, 2017) as they are facing higher demand and supply risk.[8,9] The REEs highly important for evolving technologies.[10,11] For example, Eu, Tb, and Y are the main REEs used in energy efficient applications such as light-emitting diodes (LEDs), plasma, liquid crystal displays (LCDs), compact fluorescent lamps (CFLs);[12,13] Nd, Y, La, Ce, Pr are used as the anode in rechargeable nickel-metal hydride (NiMH) batteries;[14,15] Nd, Pr, Sm, and Tb are used in high-powered magnets in computer hard drives, magnetic resonance imaging (MRI) machines, electric and hybrid vehicles.[13,16,17] Ce forms part of the catalyst used in catalytic converters[18] and La is used as a fluid-cracking catalyst in oil industry.[19] Due to the impact of varying global economic and environmental policies in recent years, the European mineral industry is unable to meet with the rising demand for REEs. This has mainly to do with the fact that 97% of the global supply of REEs is currently from China, which (since 2010) has reduced its exports by 40-60 %, apparently to protect the environment and to secure own production of Hi-Tech devices.[8] This fact has greatly increased the prices of REEs, causing tension and uncertainty among the world high technology markets.

Bismuth metal has been known since ancient times but its abundance in Earth's crust is estimated to be relatively low at about 8 parts per billion (ppb).[20] As with REEs, China accounts for about 75% of the global supply of bismuth.[21,22] Due to its brittle nature, bismuth is usually mixed with other metals such as lead, tin, iron, and cadmium to make it useful. Bismuth compounds are used in various medications, pharmaceuticals, cosmetic products, bullets, fire and electrical technologies, etc.[21,23]

1.2 Mineral processing and beneficiation

The rare-earth minerals are usually beneficiated by employing either gravity separation, magnetic separation, electrostatic separation or froth flotation, or any combination of the former.[24] The concentrated minerals are subsequently leached with either aqueous inorganic acids, such as HCl, H_2SO_4, or HNO_3 or bases such as NaOH or KOH. Through the 1950s, the solution containing REEs as chlorides or nitrates is separated into different groups by employing techniques such as fractional crystallisation and ion exchange techniques. These methods could produce pure REE metals but in small scales. For large scale production, solvent extraction has been a preferred route; however, this method is low in selectivity and produces large amounts of wastes.[25,26,27] On the other hand, ionic liquid (IL) extraction techniques[13,28] and the molecular recognition techniques[29] have gained much interest as both of these methods are considered as green separation processes. Alongside the development of better methods for extraction and separation, recovery of REEs from wastes and mining tailings is fastly becoming of significant interest globally.[8,17,30,31] Tanaka *et al.*[32] present an overview of the current recycling technologies used for the treatment of REE wastes (phosphor, permanent magnets, batteries, etc.) as well as the use of alternative solvents such as ILs for solvent extraction and separation of REEs.

Bismuth sulphide minerals are beneficiated by froth flotation techniques.[33,34] Due to technology limitations and scattered nature of its use in production, recycling of bismuth is almost impossible. Therefore, bismuth metal is obtained usually as the sub-product in other metallurgical processes and very little percentage comes from the processing of minerals where bismuth is the main metal.[21,33]

Modern research and development programs towards the optimisation of recovery of REE and Bi minerals have been lacking. Therefore, development of more reliable, nontoxic, and eco-friendly methods of extraction and/or recycling of REEs and Bi is of utmost importance to overcome the challenges. This in turn requires a rational molecular design based on the knowledge of the physicochemical and structural properties of the collectors or ligands that can leach out REE minerals or can selectively bind to a specific REE.

1.3 Coordination chemistry of REE(III)s and Bi(III)

Both REEs and bismuth are known to adopt a wide variety of coordination numbers and geometries depending on the ligands and reaction environments.[35,36] It is well known that, being strong Lewis acids, REE(III)s prefer to bond with hard bases or ligands with highly electronegative donor oxygen or nitrogen atoms. The widely used ligands for REE extraction

Table 1. Electronic configuration (E. C.) of REE(III)s and Bi(III).

Element	E. C. (M^{3+})	Ground State	No. of unpaired electron(s)	Ionic radii (pm)[a]
Sc	$[Ar]3d^0$	$^1S_0$	0	74.5
Y	$[Kr]4d^0$	$^1S_0$	0	90.0
La	$[Xe]4f^0$	$^1S_0$	0	103.2
Ce	$[Xe]4f^1$	$^2F_{5/2}$	1	101.0
Pr	$[Xe]4f^2$	$^3H_4$	2	99.0
Nd	$[Xe]4f^3$	$^4I_{9/2}$	3	98.3
Pm[b]	$[Xe]4f^4$	$^5I_4$	4	97.0
Sm	$[Xe]4f^5$	$^6H_{5/2}$	5	95.8
Eu	$[Xe]4f^6$	$^7F_0$	6	94.7
Gd	$[Xe]4f^7$	$^8S_{7/2}$	7	93.8
Tb	$[Xe]4f^8$	$^7F_6$	6	92.3
Dy	$[Xe]4f^9$	$^6H_{15/2}$	5	91.2
Ho	$[Xe]4f^{10}$	$^5I_8$	4	90.1
Er	$[Xe]4f^{11}$	$^4I_{15/2}$	3	89.0
Tm	$[Xe]4f^{12}$	$^3H_6$	2	88.0
Yb	$[Xe]4f^{13}$	$^2F_{7/2}$	1	86.8
Lu	$[Xe]4f^{14}$	$^1S_0$	0	86.1
Bi	$[Xe]4f^{14}\,5d^{10}\,6s^2$	$^1S_0$	0	103.0

[a] For complexes with coordination number 6.[37] [b] radioactive.

Table 2. Important minerals for REEs and bismuth.

Mineral	Main components
Monazite	Phosphates of lighter REEs (Ce, La, Nd, Sm) (PO_4)
Xenotime	Phosphates of heavier REEs (Y, Dy, Er, Tb, Yb) (PO_4)
Bastnasite	Fluorcarbonates (Y, La, Ce) (CO_3F)
Allanite	Hydrous silicates $(Ce, Ca, Y, La)_2(Al, Fe)_3(SiO_4)_3(OH)$
Gadolinite	Silicates $(Ce, La, Nd, Y)_2FeBe_2Si_2O_{10}$
Euxenite	Oxides $(Y, Ca, Ce, U, Th)\,(Nb,Ta,Ti)_2O_6$
Bismuthinite	Sulphide (Bi_2S_3)
Bismite	Oxide (Bi_2O_3)

include β-diketones, carboxylates, 1,10-phenanthroline (PHEN), hydroxamic acids, phosphoric acids, fatty acids, etc.[24,38–41] However, compounds of REEs with weak Lewis acids, such as dithiocarbamates (DTC) are not uncommon.[40,41] On the other hand, Bi(III), being one of the weak Lewis acids prefers soft bases such as the ligands bearing sulphur binding sites, for example, DTC, xanthates etc.[36] Some of these ligands are well-known for their industrial applications as flotation collectors. It has been shown in literature that derivatives of both

DTC and N-donating PHEN have high potential to be used as reagents for the separation of actinides from lanthanides.[42–44] However, accurate information about the relationship between electronic/molecular structures and key properties of materials require extensive experimental and theoretical data. To make it more systematic, we have considered the complexes of both REE(III)s and Bi(III) with DTC and PHEN ligands.

Although there are similarities between bismuth and some REEs in terms of a common oxidation state (+3), ionic radii, coordination number, heavier mass, etc., the physicochemical properties of their compounds can display striking variations. Detailed insight into the relationship between the structure and properties of materials or molecules necessitates the exploitation of various advanced and state-of-the-art experimental as well as theoretical methods. In this thesis work, nuclear magnetic resonance spectroscopy (NMR) and X-ray diffraction (XRD) techniques have been used as the main experimental methods while *ab initio* electronic structure methods were used for calculating the theoretical structures and NMR properties.

1.4 Challenges

It can be safely said that due to various scientific and technical challenges, the study involving REEs (or the *f*-block elements) is comparatively less feasible than that of the *d*-block metals. In the lanthanide series, inner 4*f* orbitals are progressively filled up with increasing atomic numbers. Hence, the number of outer shell electrons is essentially unchanged and, since this influences on the chemical behaviour, the result is a series of elements, in which the chemical properties of adjacent members are very similar. This poses a great challenge for their extraction from the minerals as well as for separation processes. The chemistry of a metal complex is defined by the structure of the complex and the bonding therein. The local structure and bonding of the metal atom itself within a molecule is of importance in determining its physicochemical properties. There is a vast number of experimental (spectroscopic) techniques available to determine the structure of molecules or materials as well as to study their physicochemical properties at the atomic level. One of the common issues with REEs is that, due to a higher charge density and affinity for polar groups of their cations, they are quite sensitive to moisture or water contents in the media and get hydrolysed easily. Often, due to hydrolysis, it becomes difficult to grow fine (single) crystals suitable for X-ray crystallography as the crystallisation process may take a few weeks, if not months, during which the molecule may break up. This problem is usually seen when dealing with ligands having soft-donating atoms and long alkyl chains.

The computational chemistry can act as a bridge between theory and experiments. Moreover, it can give reasonable explanations for experiments by elucidating the structure of the complexes that are formed in solutions and in solid-state. From the theoretical point of view, REEs (or *f*-block elements) are probably the most challenging group of elements for electronic structure calculations. The REEs are comparatively heavy elements, thus the macroscopic properties, reactive behaviour, as well as geometries of REE containing molecules are subjected to relativistic quantum-mechanical effects.[45–48] The influence of

relativistic effects on chemistry can be seen through shifts of spectroscopic properties with respect to nonrelativistic expectations. In addition, most REEs or their compounds have unpaired electrons, i.e. they are paramagnetic, which results in large electron correlation effects.[49,50] The two challenges mentioned above necessitate the requirement of advanced electronic structure methods to obtain accurate and reliable predictions of electronic as well as molecular properties pertinent to heavier REEs. However, with the rapid pace of increasing computer power and the widespread availability of cutting-edge electronic structure theory packages, researchers in academia and industry can study systems with ever-increasing complexity and make predictions of new materials and phenomena. In recent years, quantum chemistry has become a powerful tool in the design and development of new materials, and it shows the way to numerous experimental possibilities. Moreover, computations guide us through experiments, giving insights into what is going on, and helping to push forward the frontiers. In other words, computational methods offer the real promise of being able to complement experimental results to uncover and explore new chemistry and one can probably see the unravelling of umpteen new properties and applications of REEs in the near future.

1.5 Research methodology

This research aims at building a fundamental knowledge base concerning the electronic/molecular structure and properties of rare earth and bismuth metal complexes by employing state-of-the-art experimental and computational methods. The information gathered can be used to target the development of novel and suitable ligands for recovery, extraction, and separation of REEs. The main goals of the thesis are: (i) To gain a deeper insight into the structural characteristics of a series of REEs and bismuth metal complexes and thereby to shed light on the underlying chemistry in order to get a profound understanding of the structure-properties relationship; (ii) The examination of systematics of the properties of REEs and their compounds is of particular value in improving our knowledge of these metals[51]; (iii) Comparison of the experimental studies to those calculated by theoretical methods at different levels in order to set the base for future studies; (iv) To see through which method works and which does not, how accurate the results would be if the computations done at a certain level of theory and what experimental and theoretical methods are suitable for REEs and bismuth to get reasonably good results at a nominal expense.

A multidisciplinary approach is employed in undertaking this work. A series of metal complexes of REEs viz. Y(III), La(III), Nd(III), Eu(III), Er(III), Yb(III), and Lu(III) with diethyldithiocarbamate (DEDTC) and PHEN, and Bi(III) with diethyl- or di-*n*-butyl-dithiocarbamate, were prepared in solid form. As a major part of the research methodology, experimental NMR and XRD methods were combined with *ab initio* calculations, which has often been referred to as the "Smarter Crystallography" approach,[52–55] in order to gain deeper insights into the structure and properties of the complexes. The solution-state structures of the complexes were characterised by solution-state one-dimensional (1D) $^{1}H/^{13}C$ NMR as well as by two-dimensional (2D) heteronuclear (^{1}H-^{13}C/^{1}H-^{15}N) HSQC (Heteronuclear Single Quantum Coherence) and HMBC (Heteronuclear Multiple Bond Correlation) NMR

techniques. On the other hand, structural characterisation of the polycrystalline solids was done by solid-state ^{1}H-^{13}C and ^{1}H-^{15}N cross-polarisation (CP) magic-angle-spinning (MAS) NMR and powder-XRD (PXRD) methods, whereas crystal structures of the complexes were obtained by single crystal X-ray crystallography method.

The relativistic effects are extremely important in the accurate modelling of complexes containing *f*-block elements. The structure and property calculations of the molecular crystals of the closed-shell systems were done at the scalar- and/or spin-orbit relativistic density functional theory (DFT) level using the zeroth order regular approximation (ZORA)[56,57] and all-electron basis sets. The electronic structures of periodic closed-shell systems were modelled within a planewave-pseudopotential DFT framework,[58] including the scalar-relativistic effects, followed by the calculations of the NMR parameters by gauge-including projected augmented wave (GIPAW)[59–61] method. For the open-shell molecular systems, the computations of electron paramagnetic resonance (EPR) *g*- and zero-field splitting (ZFS) *D*-tensors were done using complete active space self-consistent field (CASSCF)[62] wavefunction theory (WFT) methods at the second order Douglas-Kroll-Hess (DKH2)[63] scalar-relativistic level, employing segmented all-electron relativistically contracted (SARC) basis sets,[64] whereas the hyperfine coupling (HFC) ***A***-tensor was calculated using the four-component relativistic all-electron matrix Dirac-Kohn-Sham (mDKS)[65,66] approach with hybrid density functionals.

1.6 Outline of the thesis

The research work presented in this Doctor of Philosophy (PhD) thesis has primarily been carried out during the years 2012-2017 at Luleå University of Technology (Chemistry of Interfaces, Division of Chemical Engineering) and at University of Oulu (NMR Research Unit, Faculty of Science). The purpose of this thesis work is to explore by various experimental and theoretical methods the molecular electronic structure and magnetic resonance properties of some selected REE(III)s and Bi(III) coordination complexes in solution and/or molecular solids. A series of heteroleptic REE complexes with DEDTC and PHEN ligands (3:1), which are either diamagnetic [Y(III), La(III), and Lu(III)] or paramagnetic [Nd(III), Eu(III), Er(III), and Yb(III)] were investigated. In case of Bi(III), the studies include homoleptic complexes with DEDTC and di-*n*-butyldithiocarbamate (*n*BuDTC) ligands. In addition, heteroleptic complexes of Bi(III) with DEDTC and PHEN and/or nitrate were also investigated.

The thesis is based on five scientific publications/manuscripts. In general, Paper I and II contain a detailed account of the molecular, crystal, and electronic structure, chemical bonding, and magnetic properties of Y(III) and La(III) complexes, respectively, as obtained by the combination of solid-state ^{13}C and ^{15}N CP-MAS NMR, XRD, PXRD, and NMR chemical shift calculations by GIPAW[59–61] method. Paper I emphasises on the modelling of a 3D structure for the Y(III)-complex by employing periodic DFT/PBE (Perdew-Burke-Ernzerhof) methods, the accuracy of which was indicated by the excellent agreements between the calculated and experimental NMR chemical shifts and PXRD pattern. As detailed in Paper II, the crystal structure of La(III) complex was *not* isostructural to the

previously reported analogous REE compounds. In both Paper I and II, the relativistic heavy atom effect of yttrium and lanthanum, respectively, on the chemical shifts of the neighbouring light atoms i.e., ^{1}H, ^{13}C, and ^{15}N were investigated at the DFT/ZORA level of theory. Paper III focuses on a theoretical *ab initio* approach to investigate and assign ^{1}H and ^{13}C NMR chemical shifts in selected paramagnetic REE complexes viz. Nd(III), Eu(III), Er(III), and Yb(III). The accuracy of the $\boldsymbol{D}$- and $\boldsymbol{g}$-tensors using the *ab initio* CASSCF methods in the DKH2 realm as well as $\boldsymbol{A}$-tensor at the mDKS approach with different DFT functionals are discussed. Manuscript IV discusses the structural and magnetic resonance properties of homo- and heteroleptic Bi(III) complexes, both in solution- and solid-state, which are being compared with the isoelectronic REE complexes. Paper V presents a study on two crystalline polymorphs of a bismuth(III) complex with nBuDTC wherein the interaction of mononuclear molecular units of the complex via secondary Bi···S bonds yielding binuclear formations of compositions $[Bi_2\{S_2CN(n\text{-}C_4H_9)_2\}_6]$ is thoroughly discussed. In both Paper IV and V, the accuracy of structure/property calculations for the periodic solids were analysed within the planewave-pseudopotential DFT framework.

2 Theoretical background of the experimental techniques used

This chapter gives a brief theoretical background for the experimental techniques used in this thesis, i.e. XRD and liquid- and solid-state NMR.

The physicochemical characterisation of molecules or materials is one of the most important aspects of physical sciences. This may involve combinations of various experimental as well as computational methods of structure and property determination at the atomic or molecular level. Many experimental techniques, for example XRD and NMR, are widely used to correlate the structure of materials to their properties.

2.1 X-ray diffraction

Solids are broadly classified into two groups: amorphous and crystalline.[67] This classification is based on the degree of order to which the atoms or molecules are arranged in the three-dimensional space. The amorphous state is characterised by having very short degree of order extending only up to a few atomic/molecular dimensions. The crystalline solids can be further categorised into two groups: polycrystalline and single-crystalline solids. In polycrystalline state, the atoms are in ordered arrays, but these arrangements are short, which may extend up to few molecules and do not recur at regular intervals. On the other hand, the single-crystals have a regular geometrical shape and high a degree of order throughout the material.

Powder samples of crystalline materials can be characterised by PXRD method.[68] The diffraction pattern can be used to determine and refine the lattice parameters of a crystal structure. Since every material has its unique PXRD pattern, it can be used to identify unknown materials by comparing them with the database for known materials. Powder patterns represent the property of the bulk material rather than of a single crystal. However, the major limitation of the PXRD technique is that no direct information about the positions of atoms and chemical bonding in a molecule can be obtained unlike by the single-crystal XRD, which offers detailed structural information, such as internal lattice of crystalline substances, including unit cell dimensions, bond-lengths, bond-angles, molecular orientation, and weak intermolecular interactions. Although, Rietveld refinement technique[69] is often used for structural analysis or to make final structural models of crystalline materials using simulated PXRD patterns, solution of crystal structures directly from a PXRD pattern has many intrinsic difficulties.[70] For single-crystal measurements, one needs neat and optically clear crystals of 50-250 microns in size.

The basic theoretical and practical concepts of XRD techniques have been thoroughly explained by Suryanarayana *et al.*[71] The well-known Bragg's law is used to identify the structures of molecules and crystals using XRD methods (Fig. 1). The law states that the crystal will appear to reflect the X-rays incident onto it if the path difference (DE+EF) between the scattered X-rays from different planes of the crystal are in phase (or constructive interference) i.e., equal to a whole number, n, of wavelength (λ):

$$n\lambda = 2d\,sin\theta \quad (1)$$

where θ and d represents the diffraction angle and the lattice spacing, respectively.

The diffracted X-rays are detected, processed, and counted for all possible diffraction directions of the lattice by changing the angle of the incident rays and orientations of the crystal. The spatial arrangement of the unique reflections is referred to as a diffraction pattern. Indices (*hkl*) are assigned to each reflection, indicating its position within the diffraction pattern. This pattern has a reciprocal Fourier transform relationship to the crystalline lattice and the unit cell in real space. This step is referred to as the solution of the crystal structure. Finally, the data generated from the X-ray analysis is interpreted and refined to obtain the crystal structure.

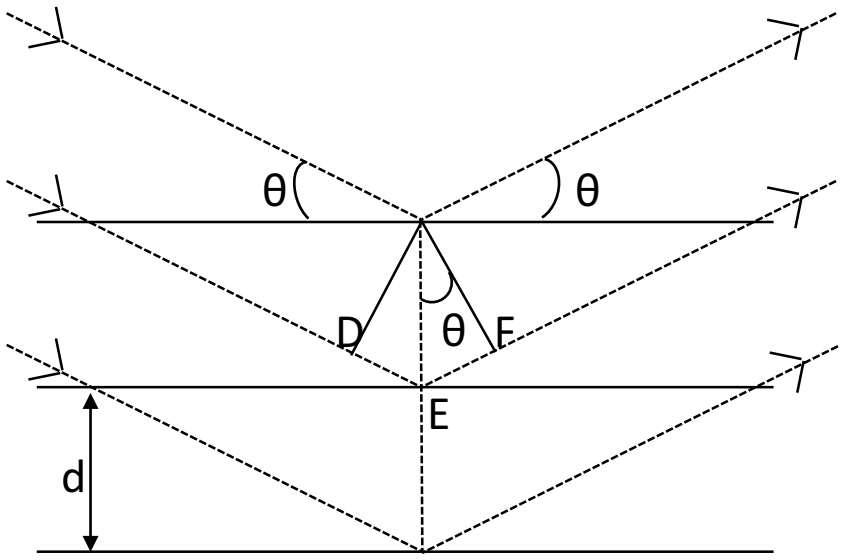

Fig. 1 Deriving Bragg's Law using reflection geometry and applying trigonometry. [$n\lambda = 2DE$ where $DE = d\,sin\theta$]

2.2 Nuclear magnetic resonance spectroscopy

NMR (nuclear magnetic resonance) is a physical phenomenon in which a nucleus with a permanent magnetic moment placed in a magnetic field is excited by electromagnetic radiation causing transitions between the nuclear Zeeman energy levels. The theory of NMR has been described in several text books.[72–74] All isotopes of an atom with spin quantum number $I \geq \frac{1}{2}$ interact with an external magnetic field $\mathbf{B}(> 0)$, due to which the spin I will attain $2I+1$ orientations, also called spin-states. These spin eigenstates are characterised by magnetic quantum number m which can have values from $-I$ to I in integer steps i.e., the energy levels are quantised. The nuclear magnetic moment of K^{th} nuclei ($\boldsymbol{\mu}_K$) is related to the nuclear spin $\boldsymbol{I}_K$ of the nucleus by $\boldsymbol{\mu}_K = \gamma_K \hbar \boldsymbol{I}_K$, where γ_K is the gyromagnetic ratio that is specific to each isotope and $\hbar = h/2\pi$ with h being the Planck's constant. The Hamiltonian

(H) representing the interaction between the magnetic moment and the magnetic field ($\boldsymbol{B}$) is given by:

$$H = -\boldsymbol{\mu}_K \cdot \boldsymbol{B} = -\gamma_K \hbar I_z B_0 \tag{2}$$

where the static field $\boldsymbol{B}_0$ is chosen to be along z direction.
For a spin-half nucleus ($I = 1/2$), the wave functions associated with the two spin states ($m = \pm\frac{1}{2}$) can be written as $|+\frac{1}{2}\rangle$ (or $|\alpha\rangle$) and $|-\frac{1}{2}\rangle$ (or $|\beta\rangle$), and the solutions of Hamiltonian (H) in Eq. (2) gives the energies of the respective states as $\mp\frac{1}{2}\gamma_K \hbar B_0$.
where α and β are the "parallel" ($m = +\frac{1}{2}$) and "antiparallel" ($m = -\frac{1}{2}$) orientations of the spin states. The population difference of spin states is governed by the Boltzmann distribution function:

$$\frac{N_\alpha}{N_\beta} = e^{\Delta E / k_\beta T} \tag{3}$$

where $N_{\alpha,\beta}$ are the populations of each spin state, k_β is the Boltzmann constant, $\Delta E = E_\beta - E_\alpha$, and T is the temperature.

At equilibrium, there will be a small preferential orientation of magnetic moments parallel to the applied field and hence an excess of nuclear spins in α state.
The resonance condition for a transition between α and β spin states by electromagnetic radiation of frequency is ν is met when the energy gap (in J) is:

$$\Delta E = h\upsilon = \gamma_K \hbar B_0 \tag{4}$$

where $-\gamma_K B_0$ is the Larmor (angular) frequency of the nucleus (in rads^{-1}).

2.2.1 Chemical shift

The chemical shift (δ) can be considered to be the chemical diagnostic of the local electron environment of a nucleus. It is the resonance frequency of a nucleus of interest relative to a reference. The induced magnetic field due to the motion of electrons around the nucleus in a molecular orbital will be added to or subtracted from the external field ($\boldsymbol{B}$) depending on the local environment of the nucleus and thereby resulting in a variation in the resonance frequency. The magnitude of such induced field is proportional to the strength of the applied field ($\mathbf{B}$), so that the effective field $\boldsymbol{B}_{\text{eff}}$ at the nucleus K is given as:

$$\boldsymbol{B}_{\text{eff}} = (\mathbf{1} - \boldsymbol{\sigma}_K) \cdot \boldsymbol{B} \tag{5}$$

where $\boldsymbol{\sigma}_K$ is the 3×3 nuclear shielding tensor and $\mathbf{1}$ is the unit matrix.
Therefore, considering the formal correction for nuclear shielding, the Hamiltonian becomes:

$$H = -\gamma_K \hbar \boldsymbol{I}_K \cdot (\mathbf{1} - \boldsymbol{\sigma}_K) \cdot \boldsymbol{B} \tag{6}$$

In normal NMR experiments $\boldsymbol{B}$ is a uniform field along the z-axis and for isotropic measurements:

$\sigma_K = \sigma_{iso} = Tr(\overline{\sigma_K})/3$, so that

$$\boldsymbol{B} = [0,0,\boldsymbol{B}_0] \text{ and } \boldsymbol{B}_{\text{eff}} = (\mathbf{1} - \boldsymbol{\sigma}_K)\boldsymbol{B}_0 \quad (7)$$

Eq. (6) implies,

$$H = -\gamma_K \hbar(\mathbf{1} - \boldsymbol{\sigma}_K)\boldsymbol{B}_0 \boldsymbol{I}_K \quad (8)$$

The resonance frequency υ_K (in Hz) of K^{th} nucleus can be defined as:

$$\upsilon_K = \gamma_K \hbar(\mathbf{1} - \boldsymbol{\sigma}_K)\boldsymbol{B}_0 \quad (9)$$

where γ_K is the magnetogyric ratio of K^{th} nucleus.
The chemical shift of a nucleus of interest (δ) can be defined as:

$$\delta = \frac{\upsilon_K - \upsilon_{ref}}{\upsilon_{r\ f}} \quad (10)$$

where υ_{ref} is the resonance frequency of the reference sample. The chemical shift is rather small so the final values are quoted in parts per million (ppm). The advantage of using 'ppm' scale over frequency is that the chemical shifts are independent of magnetic field strength while the resonance frequency differences between non-equivalent nuclei is field dependent. The effective nuclear spin Hamiltonian (in frequency unit, E/h) taking into account, in addition to the Zeeman terms (Eqn. 6), terms such as indirect spin-spin or *J*-coupling (J_{KL}), direct spin-spin or dipolar coupling (D_{KL}), and quadrupolar coupling (Q_K), is:

$$H = -\frac{1}{2\pi}\sum_K \gamma_K \boldsymbol{I}_K \cdot (\mathbf{1} - \boldsymbol{\sigma}_K) \cdot \boldsymbol{B}_0 + \sum_{K<L} \boldsymbol{I}_K \cdot (\boldsymbol{D}_{KL} + \boldsymbol{J}_{KL}) \cdot \boldsymbol{I}_L + \sum_K \boldsymbol{I}_K \cdot \boldsymbol{Q}_K \cdot \boldsymbol{I}_K \quad (11)$$

The second and third terms in Eqn. (11) contribute to the fine structure of the NMR spectrum where *K* and *L* denote two different nuclei. The last term appears only when $I_K \geq 1$.

2.3 Paramagnetic NMR

The magnetic moment of the electron ($\boldsymbol{\mu}_e$) is related to its spin angular momentum ($\hbar\boldsymbol{S}$) by[75]

$$\boldsymbol{\mu_e} = \hbar\gamma_e \boldsymbol{S} = -g_e \beta_e \boldsymbol{S} \quad (12)$$

where γ_e is the magnetogyric ratio of the electron, the Bohr magneton $\beta_e = -e\hbar/2m$ with - *e* and *m* are the charge and mass of the electron, g_e the free electron *g*-value =2.0023. The energy of interaction between $\boldsymbol{\mu}_e$ and an external magnetic field $\boldsymbol{B}_0$ is given by

$$E = -\boldsymbol{\mu_e} \cdot \boldsymbol{B}_0 = g_e \beta_e B_0 m_s \quad (13)$$

For a free electron, the energy levels of the degenerate spin states split depending on the spin magnetic quantum number, $m_s = \pm\frac{1}{2}$, the energy difference between the spin states can be written as follows:

$$\Delta E = g_e \beta_e B_0 \tag{14}$$

The major difference between Eqs. (4) and (14) comes from the fact that the energy scale is 658.23 (the ratio of magnetic moments of the electron and proton) times greater for the free electron for the same B_0 value. Also, the energy levels further split due to proton nuclear spin ($I = \frac{1}{2}$). The wave functions corresponding to $S_z = \pm\frac{1}{2}$ can be written as $|+\frac{1}{2}\rangle$ and $|-\frac{1}{2}\rangle$. Therefore, the final wave functions can be written as $|S_z, I_z\rangle$.

The corresponding Hamiltonian for the free electron can be written, based on the assumption that there is no interaction between the electron and nuclear spins, as follows:

$$H = g_e \beta_e B_0 \cdot S_Z - \gamma_K \hbar B_0 \cdot I_Z \tag{15}$$

The interaction between the nuclear and electronic magnetic moments, often referred as the 'hyperfine interaction' are represented by two terms: i) Fermi contact term and ii) dipolar or pseudocontact term. Henceforth, the overall paramagnetic contributions to the observed chemical shifts in paramagnetic systems are referred to as 'hyperfine shift', while the contribution due to terms (i) and (ii) as 'Fermi contact shift' and 'dipolar' or 'pseudocontact shift', respectively.

2.3.1 Fermi contact term

This term arises from the interaction between the nuclear magnetic moment and the electric currents emanating from the electron density at the nucleus and can be written as:

$$H_i = a\boldsymbol{S} \cdot \boldsymbol{I} \tag{16}$$

where $a = (8\pi/3)\hbar\gamma_k g_e \beta_e |\Psi(0)|^2$, and $|\Psi(0)|$ represents the electronic wave function at the nucleus. This quantity is non-zero for electrons with *s* character.

2.3.2 Dipolar term

This term results from the 'through space' interactions between the magnetic moments of the unpaired electron(s) and the nuclei and the Hamiltonian takes the form:

$$H_{ii} = \gamma_K \hbar g_e \beta \{\frac{3(\boldsymbol{r}\cdot\boldsymbol{S})(\boldsymbol{r}\cdot\boldsymbol{I})}{r^5} - \frac{\boldsymbol{S}\cdot\boldsymbol{I}}{r^3}\} \tag{17}$$

where **r** represent the location of the electron relative to the nucleus.

2.4 Solution-state NMR

Solution-state NMR is one of the most widely used techniques for determining the liquid-state structures of a variety of molecules including bio-, organic, and inorganic molecules. In

gas and liquid phases of matter, due to fast isotropic tumbling motion of molecules, the observed properties are rotational averages over all orientations. This implies that in a purely isotropic media one can measure only an average, or scalar NMR parameters, such as the isotropic chemical shifts. One-dimensional (1D) NMR measurements of ^{1}H or X-nuclei (X = ^{13}C, ^{15}N, ^{19}F, etc.) are routinely performed on molecules for structure determination, however, two- and three-dimensional (2D and 3D) experiments are especially useful in solving more complex structures either by removing the overlapped resonance lines in 1D NMR spectra or by correlating the homonuclear or heteronuclear chemical shifts.

In the Fourier transform NMR experiments, a pulse sequence describes the pattern of radiofrequency (RF) pulses and delays applied to the sample to excite the nuclear spins ($I \neq 0$) and detect the signal. The RF pulses are characterised by the pulse duration (pulse length),

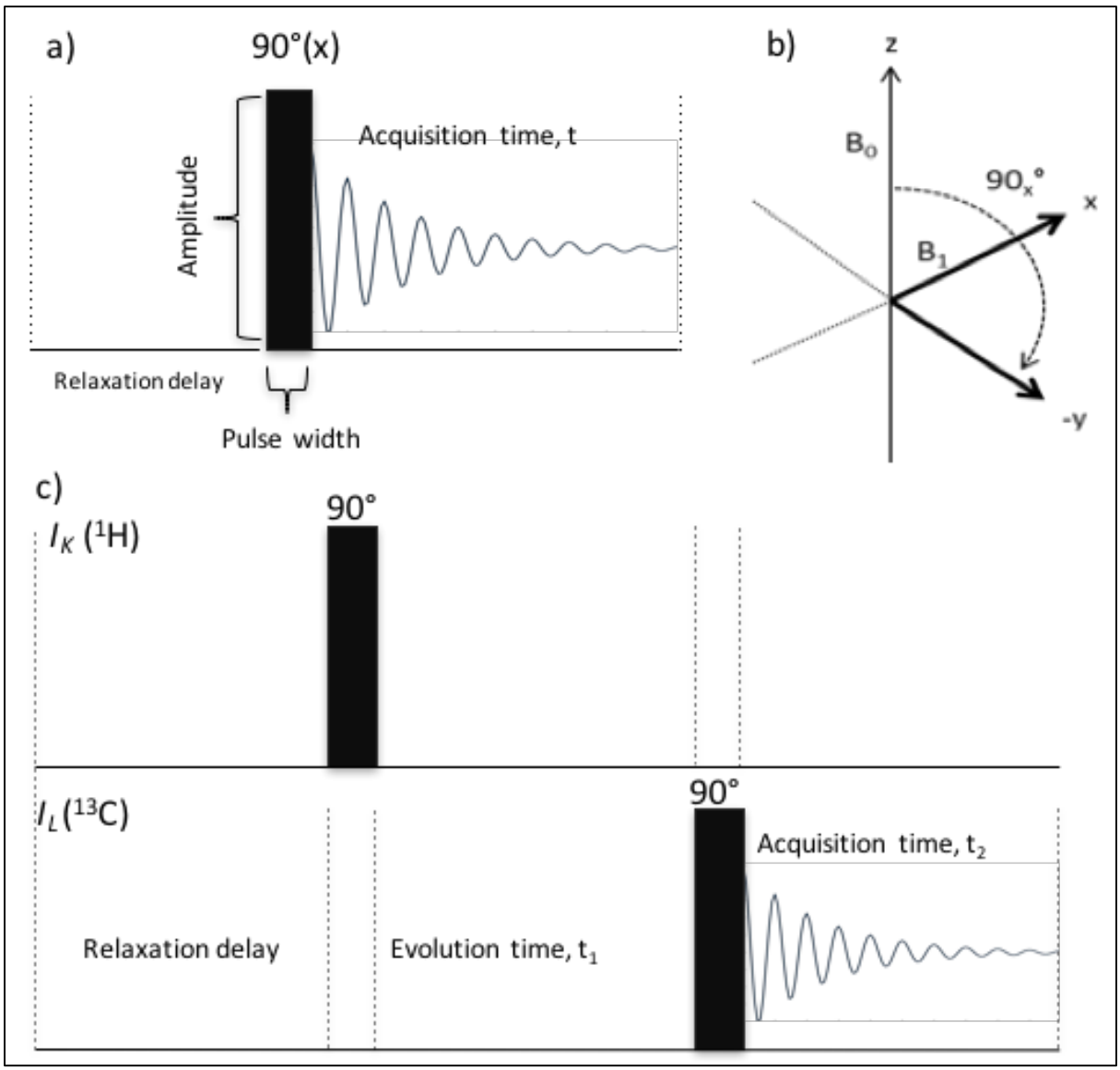

Fig. 2 a) A representative pulse sequence for (a) 1D experiment, (b) Vector diagram showing a 90° RF pulse of strength B_1 along the x-axis, tilting the magnetization to (–y) axis, (c) A representative 2D pulse sequence for heteronuclear (^{1}H-^{13}C) correlation.

amplitude (strength), and the pulse phase. Figs. 2a and 2b describe a 90° pulse applied along the x-direction of the RF coil, which tilts the magnetization vector towards –y axis. In a 1D-NMR experiment the data acquisition stage (t) takes place right after the excitation by the 90° pulse. When the pulse is off, the magnetization vector starts to precess in the x-y plane. A changing magnetic field induces current in the coil, which is then amplified. The digitized signals are then recorded as a function of time, known as the free induction decay (FID) (Fig. 2a). The Fourier transformation gives the resonance lines in the frequency domain. The plot of intensity as a function of frequency is the NMR spectrum. In 2D-NMR experiments, the acquisition stage is separated from the excitation state by intermediate stages called evolution and mixing (Fig. 2c). The acquisition is carried out many times, incrementing the delay (evolution time) between the two pulse groups. The evolution time is labelled t_1 and the acquisition time, t_2.

2.5 Solid-state NMR

Solid-state NMR spectroscopy is a powerful tool used for the study of molecular structures of simple organic/inorganic compounds as well as more complex systems, such as organometallics, clathrates, composites, polymers, and biomolecules in solid phase.[76–80] The nuclear spin interactions, which affect solid-state NMR spectra, include nuclear shielding, homo- and heteronuclear dipole-dipole coupling, and quadrupolar coupling. All these interactions are anisotropic i.e., they dependent on orientation of the crystallites with respect to the external magnetic field. Since different crystallites in a powdered sample can occupy all possible orientations, the resultant NMR spectrum may contain broad lines or powder patterns. Therefore, it is necessary to apply techniques, such as cross-polarisation (CP) magic-angle-spinning (MAS) with high-power homo- or heteronuclear decoupling to achieve high resolution in the NMR spectra. In materials chemistry, solid-state NMR is extensively used in identifying the number of non-equivalent chemical sites, phenomenon of polymorphism, structural disorder, surface chemistry, etc.[55,74,76,81,82]

2.5.1 Chemical shielding anisotropy (CSA)

As the molecular motion is constrained in solids, the observed NMR parameters, such as the nuclear shielding, become anisotropic. The nuclear shielding tensor can be decomposed into a symmetric ($\boldsymbol{\sigma}^s$) and antisymmetric components ($\boldsymbol{\sigma}^{as}$), the latter part of which does not affect the NMR spectrum, and can thus be neglected:[74]

$$\boldsymbol{\sigma}_K = \boldsymbol{\sigma}_K^s + \boldsymbol{\sigma}_K^{as} \tag{18}$$

$$\text{where } \boldsymbol{\sigma}^s = \begin{bmatrix} \sigma_{xx} & \frac{1}{2}(\sigma_{xy}+\sigma_{yx}) & \frac{1}{2}(\sigma_{xz}+\sigma_{zx}) \\ \frac{1}{2}(\sigma_{xy}+\sigma_{yx}) & \sigma_{yy} & \frac{1}{2}(\sigma_{yz}+\sigma_{zy}) \\ \frac{1}{2}(\sigma_{xz}+\sigma_{zx}) & \frac{1}{2}(\sigma_{yz}+\sigma_{zy}) & \sigma_{zz} \end{bmatrix}$$

The components of the anisotropic shielding tensor in a frame of reference defined by axes *X*, *Y*, and *Z* in the principal axis system (PAS) can be obtained by a transformation of the shielding tensor in an arbitrary coordinate system $\sigma_{i,j}$ (where i,j = x,y,z). This coordinate transformation diagonalises the matrix ($\boldsymbol{\sigma}_K^S$) to give the three principal components (σ_{XX}, σ_{YY}, σ_{ZZ}). The following conventions are used for calculation of nuclear shielding parameters [σ_{iso}, η, and σ_{aniso}] from shielding eigenvalues.[84]

Isotropic chemical shielding: $\sigma_{iso} = \frac{1}{3}(\sigma_{XX} + \sigma_{YY} + \sigma_{ZZ})$ (19)

Chemical shielding anisotropy: $\sigma_{aniso} = \sigma_{ZZ} - \sigma_{iso}$ (20)

Asymmetry: $\eta = \frac{(\sigma_{XX} - \sigma_{YY})}{\sigma_{aniso}}; (0 \leq \eta \leq 1)$ (21)

where $|\sigma_{ZZ} - \sigma_{iso}| \geq |\sigma_{XX} - \sigma_{iso}| \geq |\sigma_{YY} - \sigma_{iso}|$ (i.e., σ_{ZZ} is the principal component farthest from σ_{iso}, and σ_{YY} is the component closest to σ_{iso}).
The corresponding principal components of chemical shift tensors, δ_{ZZ}, δ_{YY}, and δ_{XX} are defined as follows:

$$|\delta_{ZZ} - \delta_{iso}| \geq |\delta_{XX} - \delta_{iso}| \geq |\delta_{YY} - \delta_{iso}| \quad (22)$$

where δ_{iso} is the isotropic chemical shift.
The ZZ component of the chemical shift (δ_{ZZ}) is related to the principal components δ_{11}, δ_{22}, and δ_{33} in the molecular PAS frame by (Mehring notation)[85],

$$\delta_{ZZ} = \lambda_1^2\delta_{11} + \lambda_2^2\delta_{22} + \lambda_3^2\delta_{33} \quad (23)$$

where $\lambda_1 = \cos\alpha \sin\beta$; $\lambda_2 = \sin\alpha \sin\beta$; $\lambda_3 = \cos\beta$; α and β are two of the three Euler angles which rotate the arbitrary laboratory frame (x,y,z) into the molecular PAS (X,Y,Z) frame (Fig. 3).

The principal components are labelled as $\delta_{33} \leq \delta_{22} \leq \delta_{11}$ with δ_{11} and δ_{33} representing the largest and smallest chemical shift, respectively (Fig 4).

2.5.2 Powder pattern NMR

In the solid-state, the NMR signals from powdered samples arise from the sum of all possible contributions of crystallites randomly oriented relative to the applied magnetic field (B_0). Thus, depending on the orientation of the crystallites, resonance lines produced by each crystallite will have different frequencies. Therefore, the sum spectrum produced by all the crystallites in the powdered sample, known as powder pattern, spreads out to a wide range of frequencies. The three principal values of the chemical shift tensor (δ_{11}, δ_{22}, and δ_{33}) can be obtained by the analysis of the powder pattern spectrum (see Fig. 4). However, when there are several non-equivalent chemical sites in a powder sample, the powder patterns from each

of them may overlap. This can result in a very poorly resolved NMR spectrum. Several solid-state NMR techniques have been developed to overcome such signal overlaps and to minimize the large chemical shift anisotropy and to increase the signal to noise ratio in the NMR spectra of dilute spins, i.e. the spins with a low natural abundance e.g. ^{13}C (1.1 %) and ^{15}N (0.36 %).[74]

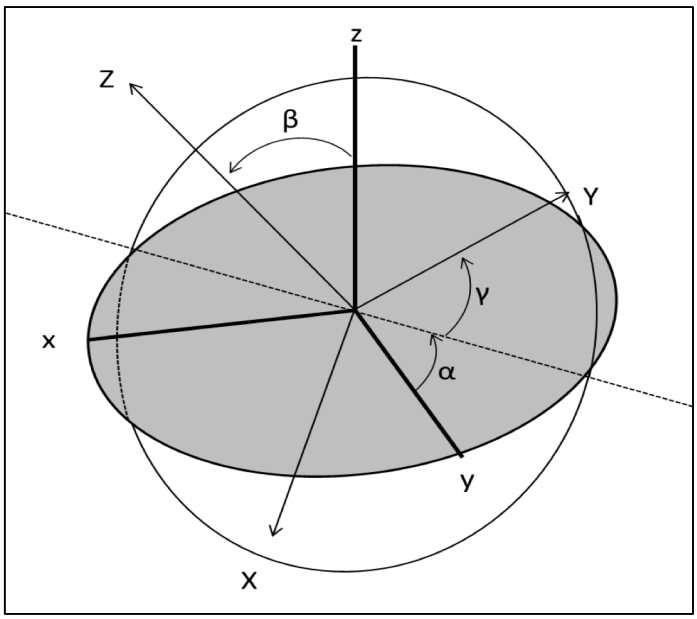

Fig. 3 Euler angles, which transform the laboratory frame (x, y, z) in a molecule, where z is taken along the direction of the applied field, into the principal axis system (X, Y, and Z (PAS)).

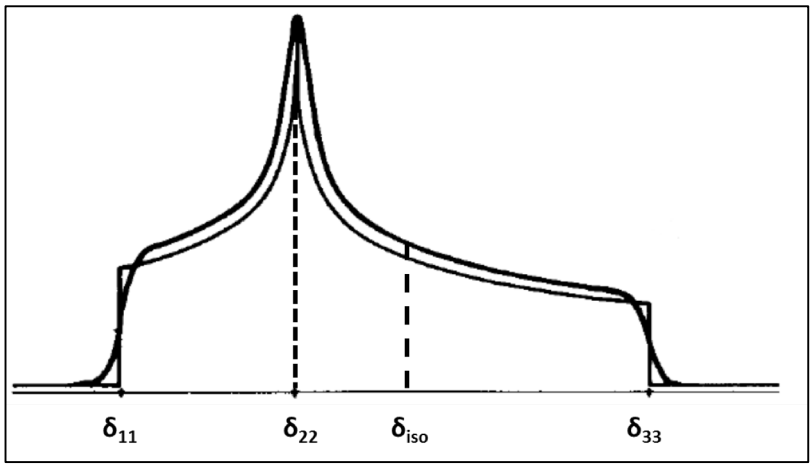

Fig. 4 Powder pattern for a non-axially symmetric chemical shift tensor.

2.5.3 Magic-angle-spinning (MAS)

In solution NMR, due to the rapid isotropic tumbling of the molecules orientation-dependent anisotropic interactions, such as chemical shift anisotropy, dipole-dipole couplings, and quadrupolar coupling interactions ($I > 1/2$) are all averaged to zero. In static solids, the effects of the above mentioned interactions do not get averaged like in solution NMR spectra. Andrew and Lowe[86] showed that some of these anisotropic interactions can be either removed

or minimized by introducing artificial motions on the solid sample. The MAS technique achieves the same result for solids, i.e. the chemical shift anisotropy and heteronuclear dipole-dipole couplings, quadrupolar couplings (first order), and homonuclear dipole-dipole couplings (at very high spinning frequencies for abundant spins, such as ^{1}H) are removed. This simplification of solid-state NMR spectra by MAS is due to the fact that the isotropic parts of the dipole-dipole coupling tensor and the electric field gradient (EFG) tensor are zero.

By spinning the sample around a given axis (see Fig. 5), the average orientation-dependence of the spin interactions become:

$$\langle 3\cos^2\theta - 1\rangle = \frac{1}{2}(3\cos^2\theta_R - 1)(3\cos^2\beta - 1) \quad (25)$$

where β is the angle between the principal z-axis of the chemical shift tensor and the rotor axis; θ_R, is the angle between the applied magnetic field B_0 and the rotor axis, and θ is the angle between the principal z-axis of the chemical tensor and B_0 field. Angle β is fixed for a given spin site; however, both θ and β can take all possible values in a powder sample. Note that θ_R is the same for all crystallites in the sample. When θ_R is set to 54.74° and the spinning rate is high enough, then the orientation-dependence of the spin interactions above is removed, i.e. $3\cos^2\theta_R - 1 = 0$ and the average $\langle 3\cos^2\theta - 1\rangle$ is zero. The angle 54.74 ° is called, the magic angle.

2.5.4 Cross-polarisation (CP)

Cross-polarisation[87] in combination with magic-angle-spinning (CP-MAS) is one of the most widely used solid-state NMR techniques for observing low abundant nuclei. A schematic diagram of the CP pulse sequence, which works on the principle of a polarisation transfer from the high abundant nucleus (^{1}H) to a low abundant X nucleus via dipolar coupling between ^{1}H and X, is depicted in Fig. 6.

At the laboratory frame, the resonance frequencies of the two spins ^{1}H and X can be written as:

$$\omega_{0H} = -\gamma_H B_0(^1\text{H}) \text{ and } \omega_{0X} = -\gamma_X B_0(\text{X}) \quad (26)$$

When the resonant fields are applied to ^{1}H and X nuclei, they precess with a nutation frequency (ω_1) (in the rotating frame)

$$\omega_{1H} = -\gamma_H B_1(^1\text{H}) \text{ and } \omega_{1X} = -\gamma_X B_1(\text{X}) \quad (27)$$

When the precession frequencies are matched (so called Hartmann-Hahn condition)[83], then one gets a "resonance" exchange of magnetisations between the ^{1}H and X spin reservoirs driven by the heteronuclear ^{1}H-X dipole-dipole interactions. Experimentally, the (H-H) matching condition is achieved in two steps: (i) A 90° excitation pulse is applied along the x-

axis on ^{1}H, which creates transverse magnetisation along –y axis and (ii) A contact pulse is applied (along –y) simultaneously to both ^{1}H and X spins so that,

$$\gamma_H B_1(^1\mathrm{H}) = \gamma_X B_1(\mathrm{X}) \tag{28}$$

where $B_1(^1\mathrm{H})$ and $B_1(\mathrm{X})$ are the spin-lock fields during ^{1}H and X contact pulses (along –y), respectively.

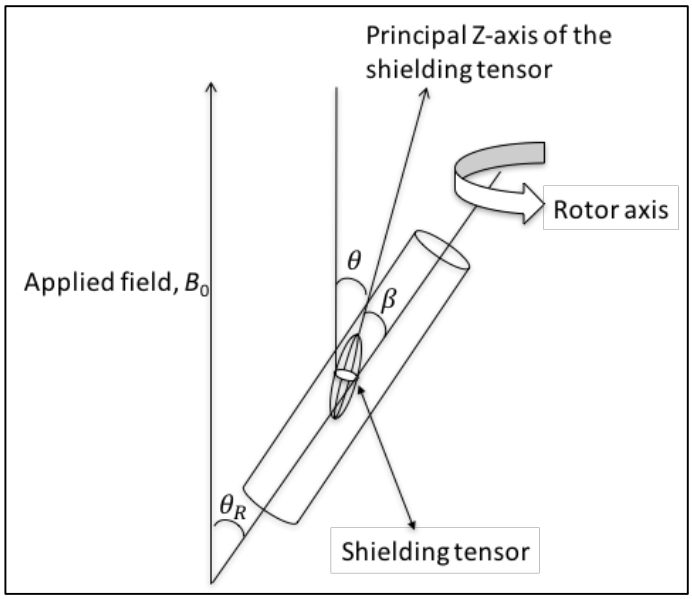

Fig. 5 Schematic representation of Magic-angle spinning experiment, in which a sample is spun at high speed in a rotor at the magic-angle (θ_R = 54.74°) with respect to B_0.

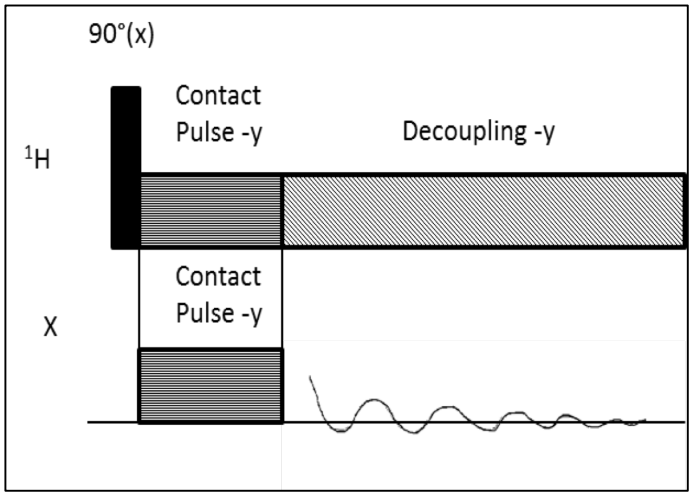

Fig. 6 Cross-polarisation pulse sequence showing initial 90°(x) pulse on protons and a contact pulse (–y) on both nuclei. Proton decoupling is switched on during signal acquisition to remove heteronuclear ^{1}H–X couplings.

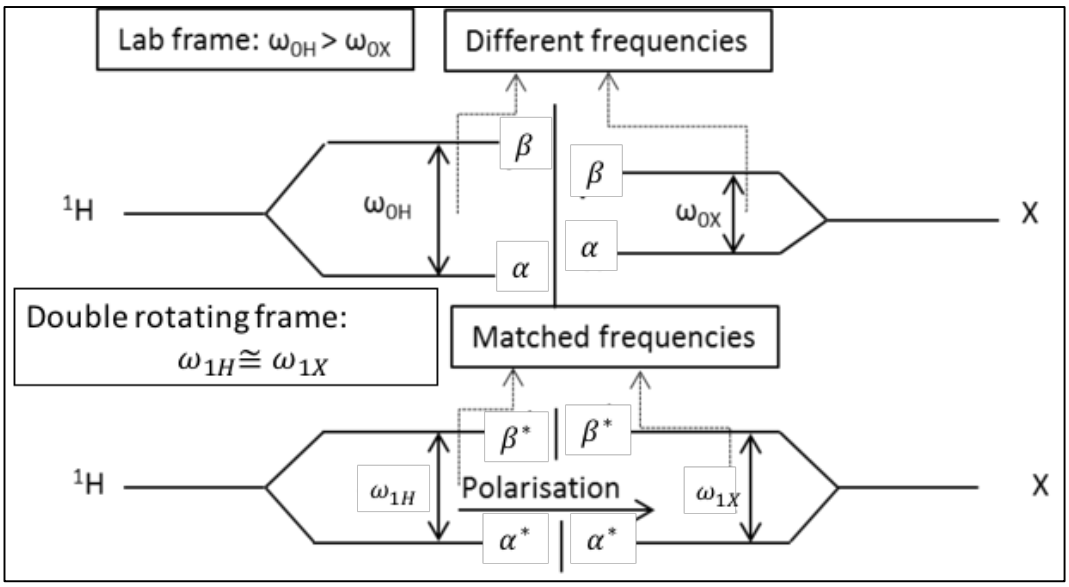

Fig. 7 Schematic representation of Hartmann-Hahn matching condition. The ^{1}H and X magnetisations precess in the rotating frame at the same rate, allowing transfer of the abundant spin (^{1}H) polarisation to the less abundant (X) spins. (α^* and β^* are spin states of ^{1}H and X nuclear spins; $\omega_{1H}$and ω_{1X} are the nutation frequencies for proton and X nuclei in the double rotating frame, respectively).

During the H–H matching condition, the energy gaps between ^{1}H and X spins become equal and the energy redistribution between ^{1}H–X spin states occur (see Fig. 7). The large ^{1}H magnetization thus reduces because of the ^{1}H spin state transitions ($\alpha^* \rightarrow \beta^*$). At the same time X spin transitions ($\beta^* \rightarrow \alpha^*$) occur to conserve energy ($*$ in the double rotating frame). Finally, a large X magnetisation in the direction of the B_1(X) field is created.

3 Quantum chemical methods in structure calculations

This chapter includes brief theoretical background consisting of concepts and some definitions together with appropriate references to scholarly literature.

Quantum chemistry has become an essential tool in the study of structures and properties of atoms and molecules. It has found a wide range of applications impacting almost every aspect of physical as well as biological science. Quantum chemical models of real materials enable not only the interpretation of experimental results but also predict properties over and above that of experimental measurements. The electronic structure of arbitrary atoms and molecules is a prerequisite to predict their spectral or any other electronic properties.

3.1 The nonrelativistic many-body problem

The primary goal of most approaches in quantum chemistry is the solution of the time-independent Schrödinger equation:[88]

$$H\Psi_i(\boldsymbol{r}_1, \boldsymbol{r}_2 \ldots \boldsymbol{r}_N, \boldsymbol{R}_1, \boldsymbol{R}_2 \ldots \boldsymbol{R}_n) = E_i\Psi_i(\boldsymbol{r}_1, \boldsymbol{r}_2 \ldots \boldsymbol{r}_N, \boldsymbol{R}_1, \boldsymbol{R}_2 \ldots \boldsymbol{R}_n) \quad (29)$$

where Ψ_i is the many-body wavefunction of the quantum system, E_i is the energy of the state Ψ_i, H is the Hamiltonian, and r_i and R_i, respectively, represent the electronic and nuclear degrees of freedom.

This many-body wavefunction[89] cannot be solved exactly even for the simplest molecular systems. So, it is necessary to have accurate approximations to the wavefunctions to move forward. The Born-Oppenheimer approximation[90] is one such basic concept of quantum mechanics, which is based on the assumption that the motion of atomic nuclei and electrons in a molecule can be separated. This means that for a system of N nuclei and n electrons, the total wavefunction can be written as a product of the nuclear (nuc) and electronic (elec) wave functions (in the field of fixed nuclei) i.e., $\Psi_{tot}(nuc, elec) = \Psi(nuc)\,\Psi(elec)$. This implies that the total energy of the system can be decoupled as:

$$E_{tot} = E(nuc - nuc) + E(nuc - elec) + E(elec - elec) \quad (30)$$

The Hamiltonian can be written as follows:[91]

$$H = -\frac{\hbar^2}{2m_e}\sum_{i=1}^{n}\nabla_i^2 - \sum_{i=1}^{n}\sum_{K=1}^{N}\frac{Z_K e^2}{4\pi\varepsilon_0 r_{iK}} + \frac{1}{2}\sum_{i=1}^{n}\sum_{j>1}^{n}\frac{e^2}{4\pi\varepsilon_0 r_{ij}} = \boldsymbol{T}_i + \boldsymbol{V}_i + \boldsymbol{V}_{ij} \quad (31)$$

where i and j denote the n electrons while K denotes the nucleus, $\nabla_i^2 = \partial^2/\partial {q_i}^2$ with ($q_i = (x, y, z)$, Z_K is the nuclear charge, r_{iK} is the distance between electron i and nucleus K, r_{ij} is the distance between electrons i and j, $\boldsymbol{T}_i$ is the kinetic energy operator, and $\boldsymbol{V}_i$ is the external (nuclear) potential energy operator. The operator describing electron-electron interaction ($\boldsymbol{V}_{ij}$) is the most difficult to handle, due to its many-body nature. The

nature of electron correlation, which includes both Coulombic repulsion of the charges and the purely quantum-mechanical exchange interaction, leads in principle to the treatment of 3^n coordinates for an *n*-electron system.

There exist many methods, differing by how the interaction term $\boldsymbol{V}_{ij}$ is analysed, for solving the wavefunction of the system (Eq. 31). One of the possible approximations is derived from neglecting interaction of electrons with each other (i.e., $\boldsymbol{V}_{ij} = 0$). This enables one to separate the Hamiltonian and the total wavefunction. For example, $\Psi_{H_2}(r_1, r_2)$, describing the motions of two electrons of a hydrogen molecule, would be the product of two hydrogen atom wavefunctions $\Psi_H(r_1)\,\Psi_H(r_2)$. However, considering the antisymmetric requirement of the wavefunction, forbids the use of such simple product. Instead, for a two-electron system, we can satisfy the antisymmetric principle by a wavefunction of the form:

$$\Psi(x_1, x_2) = \frac{1}{\sqrt{2}}[\chi_1(x_1)\chi_2(x_2) - \chi_1(x_2)\chi_2(x_1)] = \frac{1}{\sqrt{2}}\begin{vmatrix}\chi_1(x_1) & \chi_2(x_1)\\ \chi_1(x_2) & \chi_2(x_2)\end{vmatrix}, \tag{32}$$

where $\chi(x)$ denotes the *spin orbitals* with x_1, x_2 denoting the *spatial-spin* coordinates. When generalised for a system of *N* electrons, the result is a Slater determinant:

$$\Psi = \frac{1}{\sqrt{2}}\begin{vmatrix}\chi_1(x_1) & \chi_2(x_1) & \cdots & \chi_N(x_1)\\ \chi_1(x_2) & \chi_2(x_2) & \cdots & \chi_N(x_2)\\ \vdots & \vdots & & \vdots\\ \chi_1(x_N) & \chi_2(x_N) & \cdots & \chi_N(x_N)\end{vmatrix} \tag{33}$$

3.2 Self-consistent field or Hartree-Fock method

The *ab initio* wavefunction methods are by far the most promising electronic structure methods developed in quantum mechanics. The Hartree-Fock (HF) approximations[91] are fundamental to much of the *ab initio* wavefunction based electronic structure theories. The HF wavefunction will have the form of a Slater determinant (Eq. 33) in which the molecular orbitals are formulated through variational minimization of the total energy of the system. Essentially, the many-body Schrödinger Eq. (29) involving an *n*-electron wavefunction is replaced with a set of effective one-electron functions (spin-orbitals). In this way, the original instantaneous electron-electron Coulombic interactions are replaced with an average interaction for each electron. However, this approximation overestimates the Coulombic repulsion interaction energy. The very best HF wave function, obtained with a large and flexible basis set, is called the "HF limit" or complete basis set (CBS) limit. The difference in energy between the exact result and the HF limit energy is called the "correlation energy". The HF method is computationally inexpensive but it does not account for electron correlation effects. However, it is still used as either a qualitative approximation, or as a basis for advanced computational methods. More sophisticated post-HF methods are available for the accurate treatment of Coulombic interactions.[92] The major limitation with these methods is the huge computational difficulty of performing calculations on large molecules, especially with large basis sets.

3.3 Kohn-Sham density functional theory (KS DFT)

DFT provides an alternative to the *ab initio* HF methods. The electron probability density (ρ) is the central quantity in DFT, where the electronic ground state energy is a functional of the electron density, $E(\rho)$. The total ground-state electronic energy expression, including exchange and correlation contributions, for *n*-electron systems can be written as follows:[93]

$$E(\rho) = -\frac{\hbar^2}{2m_e}\sum_{i=1}^{n}\int \Psi_i^*(r_1)\,\nabla_1^2\,\Psi_i(r_1)d\boldsymbol{r} + \frac{1}{2}j_0\int\frac{\rho(\boldsymbol{r}_1)\rho(\boldsymbol{r}_2)}{r_{12}}\,d\boldsymbol{r}_1 d\boldsymbol{r}_2 + E_{XC}\,(\rho) - j_0\sum_{A=1}^{N}\frac{Z_K}{r_{1K}}\rho(r_1)dr_1 \quad (34)$$

where the one-electron spatial orbitals Ψ_i $(i = 1, 2, \cdots, n)$ are the KS orbitals; the first term represents the kinetic energy of electrons; the second term is the Coulomb interaction between the total charge distribution at r_1 and r_2; the third term, $E_{XC}(\rho)$, represents the exchange-correlation energy of the system; and the last term is the electron-nucleus attraction where the sum is over all N nuclei with index K and atomic number Z_K.

It is necessary to determine the set of wave functions Ψ_i that minimise the KS energy functional, which can be obtained from Eq. (34) by applying the variational principle to the electronic energy:

$$h_{KS}\Psi_i = \varepsilon_i\Psi_i,$$
$$h_{KS} = -\frac{1}{2}\nabla^2 + \int\frac{\rho(\boldsymbol{r}_2)}{r_{12}}\,d\boldsymbol{r}_2 + V_{XC}\,(\boldsymbol{r}_1) + V_N \quad (35)$$

where ε_i represents the KS orbital energies and V_N is the nuclear potential. The exchange-correlation potential (V_{XC}) which can be expressed as the functional derivative of E_{XC} with respect to ρ, i.e.:

$$V_{XC}(\rho) = \frac{\delta E_{XC}(\rho)}{\delta\rho} \quad (36)$$

The exact form of E_{XC} is unknown, so approximate expressions must be used. Local Density Approximations (LDA), Generalised Gradient Approximation (GGA), or hybrid functional approach, in which part of the exact HF exchange is mixed in the functional, etc. are the few schemes that have been developed for obtaining approximate forms for the exchange-correlation energy. The downside of DFT methods is in choosing the proper density functional, because it is not yet possible to do systematic improvements of the calculations. Therefore, calculations done using the contemporary DFT methods should be calibrated against the results of more accurate post-HF methods or experimental results.

3.4 Treatment of relativistic effects

A well established fact that the core electrons in heavy atoms can attain a substantial fraction of speed of light and hence shows sizable relativistic effects. It is also known that the valence

electrons do exhibit relativistic effects of the same order as core orbitals, which causes significant changes in the chemical properties of heavy element compounds. An early distinction can be made between the *scalar-relativistic (SR)* and the *spin-orbit (SO) effects*, with the former referring to the relativistic mass increase of the electron due to its high speed near the nuclei, and the later referring to the interaction between the electron spin and the magnetic field induced by the electron orbital motion in the electrostatic field of the proton. The theoretical treatment of the relativistic effects for a many-body system requires solution of an extended form of one-particle Dirac (or Dirac-Coulomb) equation rather than the nonrelativistic Schrödinger equation.[94–96] The four-component Dirac equation is a good approximation for the description of electromagnetic fields and the electrons for smaller systems. However, these calculations are very expensive and, therefore, further approximations are required for applying them in large systems. Several two-component quasi-relativistic approximations have been developed towards that direction. The most common implementations of such methods employ either higher order DKH Hamiltonian[94,97] or ZORA[56,98] approximation, both accounting for most relativistic effects as well as for Coulomb-like potentials. Further approximations in the form of single-component approaches are proposed to treat only the SC effects, while the effects due to SO coupling are incorporated in the later stage if needed. Often, the SC effects are treated using relativistic effective core potentials (RECPs), which replace core electrons with an appropriate potential experienced by the valence electrons.

3.5 Complete active space self-consistent field theory (CASSCF)

As described in Section 3.1.1., the limitations with HF approximation is that it does not incorporate the effects of Coulomb correlation, which can be further divided into two classes, the static and dynamical correlations. According to the aufbau principle for a N-electron closed-shell system, the $N/2$ lowest energy orbitals are occupied, which give rise to energetically low-lying configurations. The rest of the orbitals are unoccupied, or virtual orbitals, giving rise to the higher-lying configurations. Post-HF methods such as Moller-Plesset perturbation theory (MPn, n = 2, 3, …),[99,100] configuration interaction (CI),[101] and coupled-cluster (CC)[102] theories have been developed to incorporate mainly the dynamical correlation effect, in which the HF approximation serves as the starting point. In full CI (FCI) methods, the $\boldsymbol{n}$-electron wavefunction is expressed exactly as a linear combination of all possible $\boldsymbol{n}$-electron Slater determinants formed from a complete set of spin orbitals. However, the computational cost of FCI is so high that it is practical only for systems with a very small number of orbitals and electrons.

In general, the *f*-block elements experience weak crystal field effects, which results in energetic near-degeneracy occupations of the 4f/5f orbitals. This is a manifestation of static correlation and, therefore, the application of a multi-configurational method is critical to the accurate modelling of open-shell *f*-element complexes. The CASSCF[103,104] is one of the two variations of a multi-configurational self-consistent field (MCSCF) approximation, which provides a framework for treating those systems that cannot be properly described by a single

Slater determinant resulting in failure of the SCF methods. In the CAS technique, the molecular orbitals are divided into three parts: i) inactive space (consisting of doubly occupied orbitals), ii) active space (consisting of both doubly and/or singly occupied orbitals), and iii) external space (consisting of unoccupied orbitals). In the CASSCF approach, the FCI is performed within the active space, which encompasses, in addition to the valence region of the system of interest, several virtual orbitals. One of the main advantages of the CAS method is that it can handle smoothly, in contrast to the other methods, open-shell or nearly degenerate systems.

3.6 Basis set

Quantum chemical calculations are performed using a finite set of functions, called basis functions, for forming molecular orbitals. These basis functions can be atomic orbitals centered on atoms, linear combination of Kohn-Sham orbitals, or just plane waves (PWs), which are delocalised periodic basis functions.

In our gas phase calculations, we have used the all-electron Slater-type orbitals (STO's) as basis functions.[105,106] Slater basis functions resemble the true atomic orbital, where the centre of the function is at the nucleus. The quality of such STO's ranges from single-zeta (SZ) to quadruple-zeta (QZ) sets with various diffuse and polarisation functions.

Basis set size of plane waves depends on the volume of the box and cut-off energy. In principle, an infinite PW basis set is required to expand the electronic wave functions. However, the PW basis sets can be truncated to include only the PWs that have kinetic energy less than some cutoff energy. Truncation of a PW basis set leads to an error in the total energy. The quality of a basis set can be adjusted using a single parameter, by increasing the cut off energy if the basis set is small.

Since the CASSCF approach depends on linear combinations of different electronic configurations, the chosen basis set must allow for many configurations to be constructed. For this reason, quantitatively correct simulations typically require basis sets of at least 'triple-ζ' quality, meaning that each atomic valence orbital is constructed as a linear combination of three contracted Gaussian basis functions. Using such a basis set ensures that the configurational space is sufficiently large and flexible for correlation effects to be accurately modelled. When considering anionic systems, where valence electrons may be only loosely bound, the incorporation of diffuse functions is also recommended.

4 Computational NMR

This chapter includes brief theoretical background for computational NMR methods consisting of concepts and some definitions together with appropriate references to scholarly literature.

Quantum chemical methods have been used to calculate NMR shielding tensors for nuclei in a variety of molecules. [91,107–109] These calculations have proven to be very useful for providing insights into the underlying mechanism of nuclear shielding, including molecular conformational changes and intermolecular interactions, such as hydrogen bonding, structural disorder, etc. The accuracy of such calculated nuclear shielding constants and the orientations of the principal axes strongly depends on the quantum chemical calculations used, for example semi-empirical, *ab initio*, or DFT methods. Nuclear shielding is very sensitive to the electronic and geometrical structure of a compound and hence it is somewhat difficult to be computed accurately.

4.1 Diamagnetic systems

The energy expression of the closed-shell diamagnetic systems can be derived from the second order perturbation theory (PT2) where the interactions between the external magnetic field ($\boldsymbol{B}_0$) and nuclear magnetic moments $\boldsymbol{\mu} = \{\boldsymbol{\mu}_K\}$ are taken as small perturbations of the Zeeman energy levels:[49]

$$E(\boldsymbol{B}_0, \boldsymbol{\mu}) = E_0 + \boldsymbol{E}_{\boldsymbol{B}_0} \cdot \boldsymbol{B}_0 + \sum_K \boldsymbol{E}_{\boldsymbol{\mu}_K} \boldsymbol{\mu}_K + \frac{1}{2} \boldsymbol{B}_0 \cdot \boldsymbol{E}_{\boldsymbol{B}_0,\boldsymbol{B}_0} \cdot \boldsymbol{B}_0 + \sum_K \boldsymbol{\mu}_K \cdot \boldsymbol{E}_{\boldsymbol{\mu}_K,\boldsymbol{B}_0} \cdot \boldsymbol{B}_0 + \sum_{K,L} \boldsymbol{\mu}_K \cdot \boldsymbol{E}_{\boldsymbol{\mu}_K,\boldsymbol{\mu}_L} \boldsymbol{\mu}_L \quad (37)$$

where the terms corresponding to higher order (n>2) are neglected. The first-order terms do not contribute for closed-shell systems. Also, further perturbations are required to be able to include relativistic effects or open-shell systems.

Within the Born-Oppenheimer approximation, the NMR shielding property of nuclear spins can be expressed as second derivatives of the total molecular energy $E(\boldsymbol{B}_0, \boldsymbol{\mu}_\mathrm{K})$ with respect to two perturbations i.e., ($\boldsymbol{B}_0$) and ($\boldsymbol{\mu}_\mathrm{K}$):

$$\boldsymbol{\sigma}_K = \frac{1}{\gamma_K \hbar} \frac{\partial^2 E(\boldsymbol{\mu}_K, \boldsymbol{B}_0)}{\partial \boldsymbol{\mu}_K \partial \boldsymbol{B}_0} + 1 \Big|_{\boldsymbol{\mu}_K = 0, \boldsymbol{B}_0 = 0} \quad (38)$$

4.2 Paramagnetic systems

In open-shell paramagnetic systems, as compared to the closed-shell systems, the range of NMR chemical shifts range is usually large but in some cases, it may be reduced depending on the nature of the paramagnetic centre. These surprises basically result from the interaction of the nuclear spins with the comparatively large magnetic moment(s) of the unpaired electron(s).

The total observed chemical shift (δ_{tot}) in a paramagnetic system can be decomposed into the following terms:

$$\delta_{tot} = \delta_{orb} + \delta_{con} + \delta_{pc}, \tag{39}$$

where δ_{orb} is the diamagnetic contribution to the total shift. The chemical shift due to paramagnetic centre, i.e. hyperfine shift, is the sum of Fermi contact (δ_{con}) and pseudocontact shift (δ_{pc}).

The Kurland-McGarvey theory[110] for the NMR shielding of paramagnetic molecules, subject to a ZFS interaction of the form $S \cdot D \cdot S$, can be calculated as follows: [111–113]

$$\sigma = \sigma_{orb} - \frac{\mu_B}{\gamma \hbar k} \boldsymbol{g}.\langle SS \rangle.\boldsymbol{A}, \tag{40}$$

where μ_B, γ, k and T are the Bohr magneton, gyromagnetic ratio of the observed nuclei, Boltzmann constant, and temperature (in Kelvin), respectively. $\boldsymbol{g}$ is the EPR g-tensor and $\boldsymbol{A}$ is the hyperfine coupling term. The dyadic, $\langle SS \rangle$, is evaluated with the $2S+1$ thermally populated states. The $\boldsymbol{g}$ and $\boldsymbol{A}$ tensors may be analysed in terms of relativistic corrections due to spin-orbit interactions.

4.3 Periodic systems

Periodic or extended molecular systems, such as crystals, contain large number of electrons, which makes it impossible to solve the electronic structure as they scale in powers of number of electrons (i.e., 3^N). Instead, good approximations to the wavefunction can be obtained by treating the periodic systems as an infinite repetitions of a finite unit cell. This is done by using the periodic boundary conditions and the Bloch theorem[114], according to which, the one electron wave function of a periodic solid can be written as a linear combination of plane waves:

$$\psi_{n,\boldsymbol{k}}(r) = \sum_G c_{n,\boldsymbol{k}+\boldsymbol{G}} e^{i(\boldsymbol{k}+\boldsymbol{G})\cdot \boldsymbol{r}}, \tag{41}$$

where the sum is over all the reciprocal lattice vectors **G**, defined by $\boldsymbol{G} \cdot \boldsymbol{l} = 2\pi m$ for all lattice vectors $\boldsymbol{l}$ of the crystal, and m is an integer.

In DFT, the coefficients $c_{n,k+G}$ are the one-electron KS equations. Bloch's theorem implies that only the electronic states at a finite number of k-points in the first Brillouin zone are required to calculate the electronic potential and the total energy of solid. The computed total energy will converge as the density of k-points increases. Integration over k is performed on a mesh of points, the density of which needs to to be high enough to obtain converged properties. In this thesis, equidistant meshes were generated by using the common method of Monkhorst and Pack[115].

A drawback of the plane wave basis set is that in all-electron calculations, a very large basis set is required, because of the oscillating wave functions. They are caused by the radial nodes of the orbitals. The generally used approximation is based on the pseudopotential

theory, which allows one to describe the nucleus and core electrons with effective function form for valence electrons, i.e. effective nucleus-valence and core-valence interactions. In this method, the valence pseudo orbitals are treated in the effective potential replacing the explicit core electron and bare nucleus contributions. This allows the simplification of solution of the Schrödinger equation by making the expansion of the wave function in a relatively small set of plane waves or molecular orbitals.

The projector-augmented wave (PAW) method introduced by Blöchl[116] is used to reconstruct the all-electron density in the region close to the nucleus from the pseudowave function. The magnetic property calculations of the periodic systems presented in this thesis are carried out by the well-known gauge-including projector augmented wave (GIPAW) method[59,117], in which the nuclear shielding is represented as the ratio between induced and external field, where the former is calculated from the Biot-Savart law for the induced current.

5 Experimental details

This chapter includes a description of synthesis of the ligands and the metal complexes, growth of single crystals, details of the solution- and solid-state NMR experiments, powder- and single crystal XRD methods and the computational calculations.

5.1 Synthetic procedures

A summary of the molecules synthesised and the characterization methods used are listed in Table 3.

5.1.1 Sodium diethyldithiocarbamate and sodium di-*n*-butyldithiocarbamate

The sodium salts of DEDTC [$Na\{S_2CN(C_2H_5)_2\}$] and nBuDTCs [$Na\{S_2CN(n\text{-}C_4H_9)_2\}$] were obtained by the reaction of diethylamine and dibutylamine, respectively, with carbon disulphide (1:1 eq.) in an alkaline medium in ethanol at a temperature below 5 °C. The solids thus obtained were purified by recrystallising from ethanol and characterised by solution-state ^{1}H and ^{13}C NMR.

5.1.2 Tris(diethyldithiocarbamato)(phenanthroline)REE(III)

REE(III) complexes of formula [$REE\{S_2CN(C_2H_5)_2\}_3$ (PHEN)] (where REE = Y(III), La(III), Nd(III), Eu(III), Er(III), Yb(III), or Lu(III)) were prepared by allowing solutions of sodium DEDTC and PHEN (3:1) in acetonitrile or ethanol (20 mL) to react with the solution of the respective $REE(NO_3)_3$ in acetonitrile (5 mL) for about 10-15 minutes at room temperature.[118] The precipitates of the REE complexes were filtered and purified by repeatedly washing with small portions of ethanol and acetonitrile. The purity of the synthesised REE complexes was tested by solution-state ^{1}H and ^{13}C NMR spectroscopy. In some cases, crystals suitable for X-ray crystallography were obtained by a 'slow evaporation' method of the solvent from a saturated solution of the REE complex in chloroform/ethanol mixture (90:10 by vol.) at room temperature over a period of 4-6 weeks.

5.1.3 Tris(di-*n*-butyldithiocarbamato)bismuth(III)

$Bi(n\text{BuDTC})_3$ complex of formula [$Bi\{S_2CN(n\text{-}C_4H_9)_2\}_3$] was prepared by allowing a curdy solution of bismuth trinitrate (1 eq.) in ethanol to react with a solution of the sodium salt of *n*BuDTC (3 eq.) in ethanol for about four hours at room temperature. The precipitate thus obtained was washed with ethanol, dried and extracted with chloroform. The compound was crystallised in the triclinic system ($P\bar{1}$) upon recrystallisation from acetonitrile at room temperature over a few days (polymorph I). On the other hand, the compound was crystallised in monoclinic system ($P2_1/n$) upon recrystallisation from dichloromethane (polymorph II). Melting point: Polymorph I 101-102 °C and polymorph II 96-97 °C.

5.1.4 Tris(diethyldithiocarbamato)bismuth(III)

$Bi(DEDTC)_3$ complex of formula $[Bi\{S_2CN(C_2H_5)_2\}_3]$ was obtained by allowing a clear solution of bismuth trinitrate (1 eq.) in aqueous mannitol (1 eq.) at 40 °C to react with an aqueous solution of sodium diethyldithocarbamate (3 eq.) for about four hours at room temperature.[119] The precipitate thus obtained was washed with ethanol, dried at temperature below 50 °C, and extracted with chloroform.

5.1.5 Bis(diethyldithiocarbamato)(nitrato)(phenanthroline)bismuth(III)

$Bi(DEDTC)_2$(nitrato)(PHEN) complex of formula $[Bi\{S_2CN(C_2H_5)_2\}_2(NO_3)(PHEN)]$ was obtained by allowing a clear solution bismuth nitrate (1 eq.) in aqueous mannitol (1 eq.) at 40 °C to react with sodium DEDTC (2 eq.) and PHEN (1 eq.) in water/ethanol for about 12 hours.[120] The precipitate formed was extracted with acetonitrile and dried at room temperature.

5.1.6 Tris(diethyldithiocarbamato)(phenanthroline)bismuth(III)

$Bi(DEDTC)_3$ complex of formula $[Bi\{S_2CN(C_2H_5)_2\}_3(PHEN)]$ was obtained by allowing solutions of tris(diethyldithiocarbamato)bismuth(III) (1 eq.) and PHEN (1.1 eq.) to react in acetonitrile for 12 hours. The precipitate formed was extracted with acetonitrile and dried at room temperature.

5.2 Experimental analytical methods

5.2.1 Powder X-ray diffraction (PXRD)

PXRD patterns of polycrystalline complexes were collected using a PANalytical Empyrean X-ray diffraction spectrometer (45 kV and 40 mA) and Cu Kα radiation with λ=1.54 Å. Data collection was performed over the range 2θ=5-50° with a scan interval of θ=0.013°. The calculated PXRD pattern for the experimental structures was obtained with the Mercury crystal visualisation software.

5.2.2 Single crystal X-ray diffraction

The X-ray reflections of the single crystals of yttrium(III), lanthanum(III) and bismuth(III) (polymorphs I and II) complexes were collected on a Bruker APEX-II/Nonius Kappa CCD diffractometer using Mo Kα (λ = 0.71073 Å) radiation. The data reduction was performed using Bruker SAINT software, while the intensities for absorption were corrected using SADABS.[121] Structures were solved and refined using SHELXL-2008[122] with anisotropic displacement parameters for non-H atoms. The H-atoms were positioned geometrically (methyl groups 0.96 Å and methylene groups 0.97 Å) and refined using riding models in which the isotropic thermal parameters of the H-atoms are proportional to those of the carbon atoms to which they are attached. A symmetry check of the final CIF file was done using PLATON.[123]

Table 3. Summary of the synthesised compounds and the characterisation performed.

Complexes	Space group	Magnetic properties	Methods used	Results
$Y\{S_2CN(C_2H_5)_2\}_3(PHEN)]$	$P2_1/c$	Diamagnetic	$^1H/^{13}C/^{15}N$ solution NMR, $^{13}C/^{15}N$ CP–MAS NMR, PXRD, SC-XRD	Paper I
$La\{S_2CN(C_2H_5)_2\}_3(PHEN)]$	$P\bar{1}$	Diamagnetic	$^1H/^{13}C/^{15}N$ solution NMR, $^{13}C/^{15}N$ CP–MAS NMR, PXRD, SC-XRD	Paper II
$Lu\{S_2CN(C_2H_5)_2\}_3(PHEN)]$	$P2_1/c$	Diamagnetic	$^1H/^{13}C/^{15}N$ solution NMR	Paper III
$Nd\{S_2CN(C_2H_5)_2\}_3(PHEN)]$	$P2_1/c$	Paramagnetic	$^1H/^{13}C$ solution NMR	Paper III
$Eu\{S_2CN(C_2H_5)_2\}_3(PHEN)]$	$P2_1/c$	Paramagnetic	$^1H/^{13}C$ solution NMR	Paper III
$Er\{S_2CN(C_2H_5)_2\}_3$ (PHEN)]	$P2_1/c$	Paramagnetic	$^1H/^{13}C$ solution NMR	Paper III
$Yb\{S_2CN(C_2H_5)_2\}_3(PHEN)]$	$P2_1/c$	Paramagnetic	$^1H/^{13}C$ solution NMR	Paper III
$[Bi\{S_2CN(C_2H_5)_2\}_3]$	$P2_1/c$	Diamagnetic	$^1H/^{13}C$ solution NMR, $^{13}C/^{15}N$ CP–MAS NMR, PXRD	Paper IV
$[Bi\{S_2CN(C_2H_5)_2\}_2(NO_3)$ (PHEN)]	$P2_1/n$	Diamagnetic	$^1H/^{13}C$ solution NMR, $^{13}C/^{15}N$ CP–MAS NMR, PXRD	Paper IV
$[Bi\{S_2CN(C_2H_5)_2\}_3(PHEN)]$	-	Diamagnetic	$^1H/^{13}C$ solution NMR, $^{13}C/^{15}N$ CP–MAS NMR, PXRD	Paper IV
$[Bi\{S_2CN(n\text{-}C_4H_9)_2\}_3]$	$P2_1/c$ and $P\bar{1}$	Diamagnetic	$^1H/^{13}C$ solution NMR, $^{13}C/^{15}N$ CP–MAS NMR, PXRD, SC-XRD	Paper V (two polymorphs)

5.2.3 Solution-state NMR

The ^1H and ^{13}C solution NMR spectra were obtained on Chemagnetics InfinityPlus CMX (360 MHz) or Bruker Avance III (400/600 MHz) spectrometers whereas the 2D ^1H-$^{13}C/^{15}N$ HSQC, and ^1H-$^{13}C/^{15}N$ HMBC experiments were carried out on a Bruker Avance III (600 MHz) spectrometer. The samples were dissolved in deuterated chloroform ($CDCl_3$). The ^1H $\pi/2$ pulse length was optimised for each sample, whereas the ^{13}C and ^{15}N $\pi/2$ pulse lengths were previously optimised for standard samples. All ^1H and ^{13}C NMR spectra were referenced to TMS (0.0 ppm), while ^{15}N NMR spectra were referenced to neat CH_3NO_2 (381.7 ppm), and reported relative to liquid NH_3 (0.0 ppm).

5.2.4 Solid-state NMR

The ^{13}C and ^{15}N CP-MAS NMR spectra were recorded on Chemagnetics InfinityPlus CMX (360 MHz) or Bruker Avance III (400/850 MHz) spectrometers. The polycrystalline samples were packed in Zirconia rotors of varying diameters (3.2/4.0/7.0 mm). The CP-MAS data acquisition parameters were optimised for each sample. ^{13}C NMR chemical shifts were externally referenced to the downfield peak of powder adamantane (38.48 ppm with respect to TMS) whereas ^{15}N chemical shifts were referenced to ammonium chloride (^{15}N enriched) (39.2 ppm with respect to liquid NH_3).

5.3 Computational details

5.3.1 *Ab initio* calculations of diamagnetic periodic systems

The crystal structures were described as extended solids using periodic boundary conditions. Geometry optimisations were carried out by a DFT based CASTEP code using the Perdew-Burke-Ernzerhof (PBE) functional. For geometry optimisation, ultra-soft pseudopotentials were used to describe the interaction of the valence electrons with the nuclei and core electrons. In all the cases, the positions of hydrogen atoms were optimized since it is difficult to determine the accurate proton positions from X-ray diffraction data. The wave functions were expanded using a plane wave (PW) basis set with optimised kinetic energy cut-offs of 400-550 eV. For the atomic relaxation, a force tolerance parameter of 0.01-0.03 eV/Å was used, while for the whole cell optimisation, variation in the ionic forces between consecutive iterations to be less than 0.05 eV/Å and a stress tolerance parameter of 0.1 GPa was imposed. For the calculation of NMR shielding constants, the all-electron information was reconstructed using a GIPAW method as implemented in the NMR CASTEP code. The wave functions were expanded using a PW basis set with a kinetic energy cut-off of 440-550 eV for NMR calculation. The self-consistent field (SCF) calculations were converged when the total energy of the system was stable within 10^{-5} eV.

5.3.2 *Ab initio* calculations of diamagnetic molecular systems

Gas phase calculations of molecular units of experimental structures, for which the hydrogen atoms were optimised using the CASTEP code, were performed with an ADF program package. The S type orbitals (STOs) basis sets from the standard ADF basis set library such as the valence triple-ζ basis set with two polarisation functions (TZ2P) were used. ^{1}H, ^{13}C, and ^{15}N chemical shifts were calculated as the difference between the absolute shielding constant for reference compounds and the shielding constant of each nucleus on the sample molecule where the reference molecule is TMS for ^{1}H and ^{13}C, and NH_3 for ^{15}N. The valence triple-ζ basis set with two polarisation functions (TZ2P) at the PBE level of theory was used for the geometry optimisation of all reference molecules unless otherwise mentioned. Reference shielding values were calculated with the same level of theory as the complex.

5.3.3 *Ab initio* calculations of paramagnetic molecular systems

The experimental structures of all four paramagnetic REE complexes were taken from the literature.[118,124,125] The geometry optimisation of one molecular unit of the complexes were performed in two ways: i) either relaxing the positions of only hydrogen atoms ("H-opt") or ii) optimisation of the positions of all atoms ("full-opt"). The optimisations were performed in Turbomole 6.5 code[126] using either GGA/BP86 or hybrid PBE-25%HF (with added D3 dispersion correction energy term) functional. To mimic the experimental conditions of NMR measurements, the full structural optimisations were done by employing the well-known conductor-like screening model (COSMO)[127,128] of solvents where the solute molecule forms a cavity within the dielectric continuum of permittivity, which represents the solvent ($CDCl_3$). For the paramagnetic centre, scalar-relativistic energy-consistent small-core (ECP28MWB) and the appropriate (14s13p10d8f1g/ 10s8p5d4f1g) (in the primitive/contracted notation) valence basis set were used. Ligand atoms were treated with an all-electron def2-TZVP (triple-ζ valence plus polarisation) basis set.

The terms needed for computing the pNMR chemical shifts were calculated by three different software packages, i.e., orbital contributions to the chemical shifts (σ_{orb}) by GAUSSIAN 09,[129] EPR $\boldsymbol{g}$- and $\boldsymbol{D}$-tensors with ORCA (version 3.0.1)[130] and the $\boldsymbol{A}$-tensor with ReSpect (version 3.3.0).[131] The computations of $\boldsymbol{g}$- and $\boldsymbol{D}$-tensors were done using CASSCF *ab initio* WFT methods at the DKH2 relativistic level. On the other hand, 4c-mDKS calculations of the $\boldsymbol{A}$-tensor were done in the ReSpect program with PBE as well as with the customised PBE-xHF functionals (where the exact exchange, x= 25% or 40%). All-electron def2-TZVP basis sets were used in the 4c-mDKS calculations for light elements whereas segmented all-electron relativistically contracted (SARC) for the metal centre. In the 4c-mDKS calculations, an integration grid of ADAPTIVE size for the Lebedev angular points was applied and 110-120 radial grid points were used for all the atoms. For 4c-mDKS calculations, the self-consistent field (SCF) energy convergence criterion was set to 10^{-5} a.u. The electronic ground states of Nd(III), Eu(III), Er(III), and Yb(III) are $^4I_{(9/2)}$, $^7F_0$, $^4I_{(15/2)}$, and $^2F_{(7/2)}$, respectively. The active space in the state-average CASSCF calculations, consisted of three, six, three, and thirteen metal f -electrons in the seven Nd(4f), Eu(4f), Er(4f), and Yb(4f) orbitals, respectively. In case of Nd(III), all 35 quartet and 77 doublet states, for Eu(III) all 35 heptet and 112 quintet states, for Er(III) all 35 quartet and 77 doublet states, and for Yb(III) all 7 doublet states allowed by the CAS(3,7), CAS(6,7), CAS(11,7), and CAS(13,7) calculation, respectively, were included.

6 Summary of Papers

This chapter summarises the main results of the Papers (I, II, and IV) and the manuscripts (III and V). Figures and tables are included to illustrate the main results. The DTC-PHEN complexes of various REE(III)s and Bi(III) are compared.

The REE(III) complexes with DEDTC and PHEN ligands that were synthesised in this research work have the same chemical composition [REE{$S_2CN(C_2H_5)_2$}$_3$(PHEN)]. The structures of all these complexes belong to the monoclinic crystal system (space group $P2_1/n$), except for the La(III) complex which crystallised in the triclinic system (space group $P\bar{1}$). In all these complexes, the REE(III) ions have a coordination number of eight, with the mononuclear molecules attaining a distorted square antiprismatic geometry. However, the bond parameters (bond lengths and bond- and torsional-angles), as observed from their crystal structures, have shown significant differences for these complexes. Since the property of a material is manifested in its electronic and molecular/crystal structure, the structural variations in the REE(III) complexes can lead to variations in the observed electronic and molecular properties. NMR being a sensitive technique to study the local structures of molecules, it was chosen to study the isoelectronic REE(III) complexes, i.e. significant changes in the NMR spectral data for the complexes can be expected when there are variations in the local electronic structure of the molecules. In other words, being able to identify and differentiate the REE-$(DEDTC)_3$-PHEN complexes either in solution- and/or solid-state, indicate that the structure-property relationship of the REE(III) ions can be monitored by using NMR methods. A comparison of the experimental properties of complexes with those obtained from the theoretical modelling methods can be used for analyses of the experimental results as well as to develop a novel model for predictions of the properties of systems not yet studied. A successful theoretical modelling of REE(III) complexes can be useful to design and develop new ligands for REE(III)s.

6.1 Diamagnetic REE systems

The molecular arrangements and assembly guided by intermolecular interactions, such as the van der Waals, dispersion and multipolar forces, and hydrogen bonding are the main factors that determine the bulk physical properties of materials. The understanding of the relationship between structure and properties have long guided the discovery of novel materials. These studies often require a multidisciplinary approach involving both experimental and theoretical techniques. Among several quantitative methods to identify such relationships in crystalline systems and for their structural characterisation, XRD and NMR spectroscopy have been at the forefront. Since the XRD powder pattern is unique for each crystalline form of a material, it is often used to identify different solid-phases, similarities and/or differences between crystal structures, to determine the lattice parameters and to solve crystal structures, etc.[70,71] On the other hand, NMR and X-ray crystallography are complementary methods used to determine

the local structure, composition, and dynamics of materials. The single crystal X-ray crystallography measurements require unfractured and optically clear single crystals of suitable size whereas the NMR measurements require only polycrystalline powder samples. Other notable differences between these two techniques are existing in terms of spatial distribution of molecules in the sample and time scale accessible to each method. Often, it is necessary to use a combination of complementary methods to gain further information of the systems under study.

In this context, Papers I and II investigate molecular, crystal, and electronic structures and spectroscopic properties of mononuclear heteroleptic complexes of two of the diamagnetic REEs, i.e., Y(III) and La(III) with DEDTC and PHEN ligands as probed by a combination of powder- and single crystal-XRD methods, NMR spectroscopy, and quantum chemical methods. The molecular structures, along with crystallographic atom labelling scheme, of Y(III)- and La(III)-complexes are displayed in Figs. 8a and 8b, respectively. In Papers I and II, the solution-state structure of the Y(III)- and La(III)-complexes, respectively, were predicted by ^{1}H, ^{13}C, and ^{15}N NMR data in $CDCl_3$ solution (see Figs. 2S-4S in the ESI of Paper I and S1-S3 in the ESI of Paper II), which confirmed the stoichiometric ratio between the DEDTC and PHEN ligands (3:1) but displayed only one set of signals for both DEDTC and PHEN ligands indicating that all three DEDTC ligands are equivalent. Also, it was observed that the formation of the metal complexes resulted in deshielding of almost all chemical shifts of the ligand atoms but to different extents. On the other hand, ^{13}C and ^{15}N solid-state CP-MAS NMR data of the Y(III)- and La(III)-complexes presented multiple resonance lines for both DEDTC and PHEN ligands. In the case of Y(III), the integrated peak intensities for both ^{13}C (2:1) and ^{15}N (1:2) suggested at least three inequivalent DEDTC ligands in the asymmetric part of its unit cell (see Figs. 9a and 10a and Table 4). For La(III)-complex, five distinct ^{13}C and three ^{15}N resonance lines with integrated intensity ratios of 1:2:1:1:1 and 2:3:1, respectively, both suggesting the presence of at least six DEDTC ligands in the asymmetric part of the unit cell, and hence, implying a non-centrosymmetric packing arrangement of molecules (see Figs. 9b and 10b and Table 5) were observed.

In Paper I, the observed similarities between the PXRD patterns for Y-DEDTC$_3$-PHEN and Nd-DEDTC$_3$-PHEN[118], in terms of their relative peak intensities and peak positions, suggested that both complexes must belong to the same crystal system (i.e., monoclinic, $P2_1/c$) (see Fig. 1 in Paper I). However, since the Nd(III)-complex is paramagnetic in nature one cannot correlate the NMR parameters of the above two complexes with each other. In the absence of a crystal structure, it was motivating to predict and model a theoretical crystal structure for the Y(III)-complex. The crystal structure modelling was done by replacing the Nd^{3+} ion by Y^{3+} in the known crystal structure of the Nd(III)-complex[118], followed by the geometry optimisation using the state-of-the-art density functional theory methods for periodic systems. The experimental ^{13}C and ^{15}N solid-state NMR data showed excellent agreements with the calculated NMR parameters for the modelled Y(III)-complex structure (see Table 4 in Paper I). The single crystal structure of the Y(III)-complex was later solved and compared with the modelled structure, showing good resemblances in terms of molecular orientation, lattice parameters, unit cell volume, bonding parameters, PXRD

Table 4. Comparison of the experimental solid-state ^{13}C and ^{15}N CP-MAS NMR chemical shifts for the DTC carbon and all nitrogen atoms for the Y(III)-complex with the ADF (SO-ZORA) and GIPAW calculated chemical shifts for the fully optimised structure (Expt. = experimental solid-state NMR results).

Site	Atoms	ADF	GIPAW	Expt. (±0.1)
^{13}C Chemical shifts (ppm)				
DTC	C23	206.2	204.2	205.5
	C13	206.0	204.2	205.5
	C18	205.3	203.0	204.0
^{15}N Chemical shifts (ppm)				
PHEN	N2	281.0	281.3	281.2
	N1	279.1	278.9	278.9
DTC	N4	173.2	175.8	176.5
	N5	170.5	171.0	169.6
	N3	168.8	168.9	169.6

Table 5. Experimental solid-state ^{13}C and ^{15}N CP-MAS NMR chemical shifts (of DTC carbon and all nitrogen atoms) for the La(III)-complex compared with the ADF (SO-ZORA) and GIPAW calculated chemical shifts for the fully optimised structure (Expt. = experimental solid-state NMR results).

Site	Atoms	ADF	GIPAW	Expt. (±0.1)
^{13}C Chemical shifts (ppm)				
DTC	C31	208.2	208.5	207.8
	C32	207.3	206.8	206.9
	C12	207.3	206.1	206.9
	C22	206.0	204.5	204.9
	C21	205.0	203.8	203.6
	C11	204.8	201.1	202.1
^{15}N Chemical shifts (ppm)				
Phen	N24	307.4	306.8	286.8
	N25	304.9	306.9	286.8
	N14	302.2	301.6	283.3
	N15	300.2	295.9	280.2
DTC	N11	189.4	190.7	179.4
	N21	185.5	189.5	179.4
	N12	183.3	187.4	176.4
	N22	180.5	187.4	176.4
	N23	180.4	185.9	176.4
	N31	180.1	181.2	172.3

patterns, as well as the NMR chemical shift data (see Tables 1S and 2S in the ESI of Paper I). In Paper II, it was revealed that La-DEDTC$_3$-PHEN complex displayed a substantially different PXRD pattern (see Fig. 1 in Paper II), and ^{13}C and ^{15}N CP-MAS NMR spectra (see Figs. 9b and 10b), indicating that the La(III)-complex is *not* isostructural with the previously reported analogous REE complexes (space group $P2_1/n$)[118,132]. The single crystal X-ray

structure of the La(III)-complex (triclinic, $P\bar{1}$) supported the structural predictions made based on the PXRD and NMR data. The crystal structure of the La(III)-complex also revealed that one of the DEDTC ligands show conformational disorder. The spectral resolution of ^{13}C and ^{15}N solid-state NMR spectra, however, was insufficient to observe this disorder. The GIPAW NMR chemical shift calculations, averaged over disordered ligands, supported the assignment of the experimental ^{13}C and ^{15}N NMR spectral data (see Table 1 in Paper II). The best correspondences were obtained with the structure where the atomic positions in the X-ray unit cell were optimised at the DFT level.

In paper I, the chemical shift tensors (CST) of DTC carbons were experimentally determined by recording the CP-MAS NMR spectra of the complex at two different spinning frequencies and by calculating the intensities of the spinning sidebands (see Figs. 4 and 5 in Paper I). There was a very good correspondence between the GIPAW calculated and experimental CST parameters i.e., three principal components of the CST ($\delta_{XX}, \delta_{YY}, \delta_{ZZ}$), CSA ($\delta_{aniso}$), and asymmetry ($\eta$) (see Table 7 in Paper I). The orientation of the CST is such that the most shielded component (δ_{ZZ}) aligns parallel to the –NCSS- plane along the C-N bond while the least shielded component (δ_{XX}) aligns perpendicular to the C-N bond in the –NCSS- plane (see Fig. 11S in the ESI for Paper I).

It has been established that for molecular systems involving heavy atoms (Z>36), relativistic quantum mechanics must be used to get accurate descriptions of electronic and molecular structures and properties. In that context, the effect of heavy atoms (Y and La) on the calculated chemical shifts of the light atoms (^{1}H, ^{13}C, and ^{15}N) were analysed for one molecular unit of the complex using the DFT theory at both scalar (SR) and spin-orbit plus scalar (SO) ZORA relativistic level. It was observed that the SO corrections deshielded the DTC carbons and all nitrogen atoms by ca. 5.5 and 1.0 ppm, respectively, while for all other light atoms the SO effects were negligibly small (see Table 5 in Paper I and Table 1 in Paper II). Also, a qualitative analysis of a model fragment $[S_2CNC_2H_5]^-$ suggested that the major part of the SO contribution on the DTC carbon atom comes from the delocalised orbitals on the sulphur atom. At the ZORA level, the inclusion of SO corrections have slightly improved the chemical shifts but did not alter either the chemical shift order or the orientation of the CST. Overall, the roles of the SR and SO relativistic effects on NMR shielding suggested that already SR level qualitatively reproduces the experimental chemical shifts.

The chemical shifts of the carbon and nitrogen atoms of the dithiocarbamate (S_2CN) moiety are correlated to the 'mesomeric effect' or π bonding order of the S_2CN fragment[134,135], i.e. π-bond orders of the CS(1), CS(2), and CN bonds. The total π-bond orders will be maximum for equal π bonds while it will decrease with increasing inequality of the three π bonds. A higher CN π-bond order usually results in lower chemical shift value for ^{13}C and vice versa. On the other hand, due to the partial double bond character of CN bonds, a larger δ^+surplus charge appears at these nitrogen atoms, which makes the nitrogen atoms significantly deshielded. However, the chemical shifts of nitrogen atoms are additionally affected by the (+)inductive effect of the alkyl substituents on the nitrogen atoms[135]. Therefore, the observed differences in ^{13}C and ^{15}N chemical shifts of S_2CN groups of various complexes mentioned in

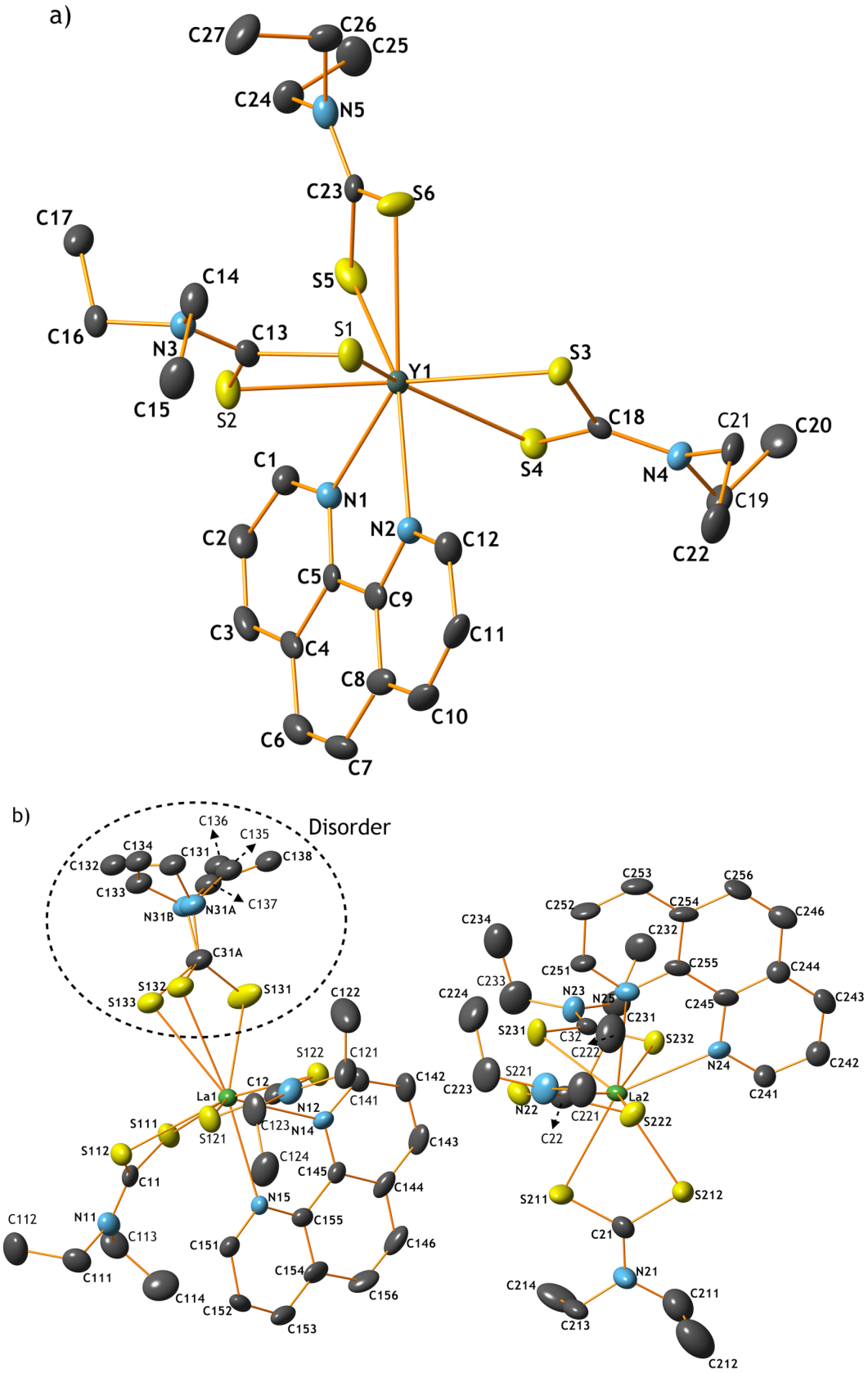

Fig 8. Structures of mononuclear Y-DEDTC$_3$-PHEN (**a**) and La-DEDTC$_3$-PHEN (**b**) complexes as seen from the asymmetric part of the respective unit cells. The atoms represented as thermal ellipsoids at 50% probability. Hydrogen atoms are omitted for clarity.

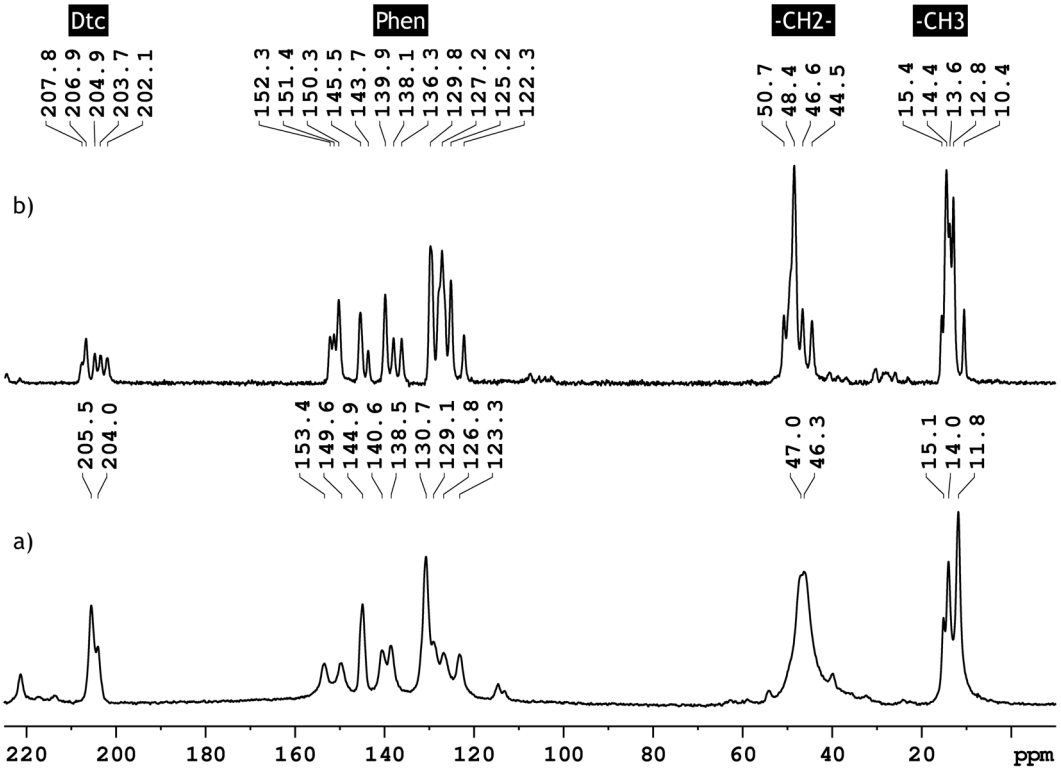

Fig. 9 Solid-state ^{13}C CP-MAS NMR spectra of Y-DEDTC$_3$-PHEN complex (**a**) and La-DEDTC$_3$-PHEN complex (**b**)

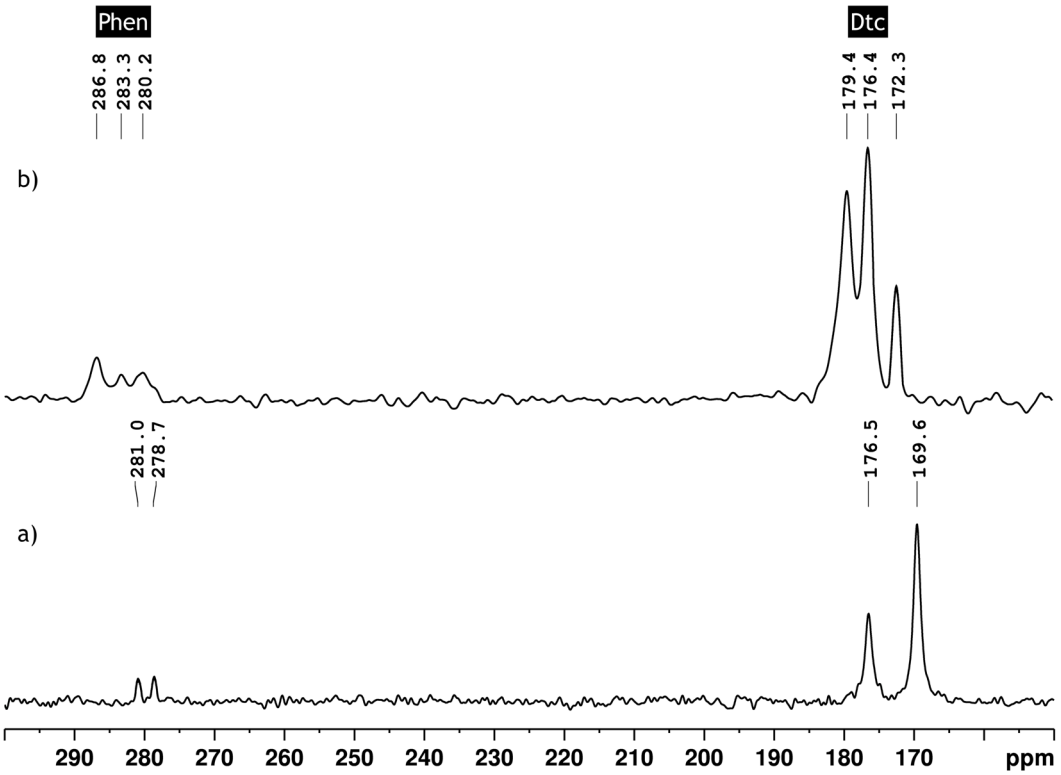

Fig. 10 Solid-state ^{15}N CP-MAS NMR spectra of Y-DEDTC$_3$-PHEN complex (**a**) and La-DEDTC$_3$-PHEN complex (**b**).

this thesis can be attributed to the simultaneous manifestation of the mesomeric effect of the dithiocarbamate ligands and to the inductive effect of the alkyl substituents. In Paper I, the effect of variations in the C-N bond lengths and S-C-S bond angle on the ^{13}C and ^{15}N nuclear shielding values were analysed by uniformly increasing the C-N bond lengths from 1.30-1.40 Å and S-C-S bond angles from 100-130° (see Tables 3S-5S and Figs. 7S and 8S in the ESI of Paper I). Both ^{13}C and ^{15}N isotropic shielding values varied almost linearly with the changes in the bond lengths and angles. For example, a variation of 0.01 Å of the C–N bond length was found to alter the shielding values up to 1.5 ppm for both nuclei, while as the bond-angle was varied from 100 to 130°, the ^{13}C atom became ca. 23 ppm more shielded and the ^{15}N atom ca. 17 ppm less shielded.

In Paper I, the so-called "solid-state" or "crystal lattice effect" on the ^{13}C and ^{15}N chemical shifts and CST parameters was analysed by comparing the results obtained from both solid-state GIPAW and ADF calculations for one molecular unit in vacuum, at the SR level of theory (see Table 7 in Paper I). Absence of "crystal lattice effect" in ADF calculations was found to decrease the chemical shift difference between the crystallographically inequivalent atoms. Although the δ_{aniso} values calculated by GIPAW and ADF are very similar and quite close to the experimental results, the η predicted by ADF showed larger deviations from the experimental values due to neglected solid state effects. The GIPAW calculated values, for one, are very close to the experimental ones. The changes due to inclusion of SO effects are to the same direction as the crystal lattice effects, but they do not fully compensate for the missing "crystal lattice field" in ADF. A very similar "crystal lattice effect" was seen in the GIPAW calculated ^{13}C and ^{15}N chemical shifts of La(III)-complex (see Table 1 in Paper II). As can be seen from Tables 4 and 5, the chemical shift range for DTC carbon and PHEN nitrogen atoms in the La(III)-complex is larger than in the Y(III)-complex, while for DTC nitrogen atoms it remains the same.

6.2 Paramagnetic REE systems

In Paper III, a recently developed methodology for combined DFT and correlated *ab initio* computations[82-84] was applied to investigate the paramagnetic effects on ^{1}H and ^{13}C NMR chemical shifts of four selected rare-earth metal complexes viz. Nd(III), Eu(III), Er(III), and Yb(III) with DEDTC and PHEN (3:1) ligands in $CDCl_3$ solutions. The molecular structure of the representative REE complex along with atom labelling scheme is displayed in Fig. 11. The NMR spectral data presented unique fingerprint regions for the respective paramagnetic centre. The paramagnetic contributions to the total isotropic chemical shifts were expressed in terms of the EPR parameters, such as $\boldsymbol{A}$- and $\boldsymbol{g}$-tensors, and for systems with a total spin $S>1/2$ in terms of the $\boldsymbol{D}$-tensor. The $\boldsymbol{A}$-tensor was calculated using four-component relativistic DFT approach with special attention on hybrid functional while the $\boldsymbol{D}$- and $\boldsymbol{g}$-tensors were calculated using *ab initio* CASSCF methods. The active space of the underlying CASSCF wave function consists of three (S=3/2), six (S=3), eleven (S=3/2), and thirteen (S=1/2) electrons in the seven metal 4*f*-orbitals, respectively, for Nd(III), Eu(III), Er(III), and Yb(III) systems. The so-called "isotropic shift", which is defined as the difference between the

chemical shift of a given nucleus in paramagnetic versus diamagnetic environment, is calculated with respect to the homologous diamagnetic Lu-DEDTC$_3$-PHEN complex (see Table 6). The solution-state ^{1}H and ^{13}C NMR spectra for the Lu(III)-complex are displayed in Figs. S6 and S7, respectively, in the ESI for Paper III. The full assignments of the ^{1}H and ^{13}C NMR signals for the paramagnetic complexes were achieved by comparison of the combined 1D and 2D experimental NMR results with *ab initio* calculated chemical shift values.

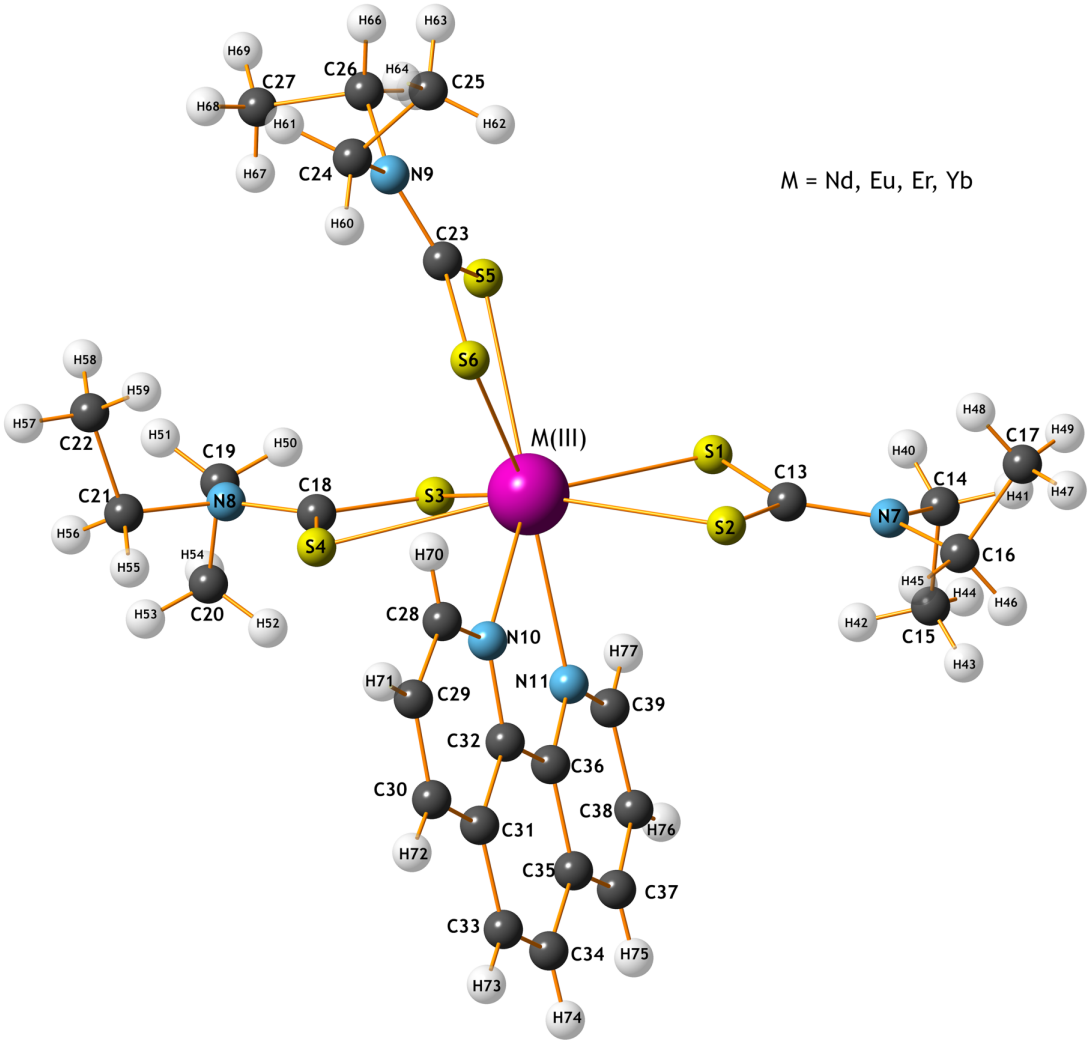

Fig. 11 Molecular structure of the paramagnetic complex (M= Nd, Eu, Er, Yb), showing atom labelling scheme.

6.2.1 Eu(III) system (S=3)

The experimental ^{1}H and ^{13}C solution NMR spectra, showing well-resolved hyperfine-shifted resonance lines with chemical shifts over a range of 0-13 and 0-508 ppm, respectively, are depicted in Figs. 12a and 13a. The theoretical pNMR chemical shifts obtained at the "H-opt" and "full-opt" geometries by combined *ab initio* WFT at the CASSCF/DKH2 level calculations of ***g***- and ***D***-tensors, and four component DFT calculations of ***A***-tensor are compared with the experimental chemical shifts in Table 6. In the ^{1}H NMR spectrum, the PHEN protons that are closest to the paramagnetic centre (H70/77) as well as the methylene

Table 6. Experimental solution-state and *ab initio* calculated ^{1}H and ^{13}C chemical shifts for Eu(III) complex.

Atoms	H-opt[a]	H-opt[b]	Full-opt[b,d]	H-opt[c]	Expt. (±0.01)	Expt. (±0.01)[b]
^{13}C Chemical shifts (ppm)						
C13,C18,C23	856.5	608.5	693.4	597.7	507.87	206.27
C28,C39	262.6	214.0	225.0	221.1	202.69	152.16
C32,C36	177.6	169.2	187.6	177.4	156.18	145.21
C30,C37	166.0	160.5	160.6	165.9	152.04	137.98
C33,C34	122.5	123.3	132.4	125.3	123.42	129.74
C31,C35	89.8	95.7	105.6	95.1	102.05	127.08
C29,C38	90.6	90.2	108.2	88.4	101.98	123.89
$-CH_2$	-84.9	-15.4	-6.5	-4.3	13.45	46.42
$-CH_3$	18.6	15.0	6.4	14.9	8.88	12.70
^{1}H Chemical shifts (ppm)						
H70,H77	9.0	10.0	12.9	8.4	12.78	10.06
H72,H75	2.4	4.9	10.1	5.1	7.76	8.38
H73,H74	6.5	6.3	8.9	7.0	7.11	7.85
H71,H76	5.9	7.6	5.2	8.4	7.09	7.73
$-CH_2$	-7.9	2.1	-1.5	3.3	1.22	3.80
$-CH_3$	2.7	2.4	-0.3	2.7	0.42	1.13

[a] HFC/PBE/mDKS; [b] HFC/PBE0/mDKS; [c] HFC/PBE0-40HF/mDKS; [d] Geometry optimization (DFT/DISP3/PBE-25HF/COSMO). For all above cases the $\boldsymbol{g}$- & $\boldsymbol{D}$- tensors were calculated at the CASSCF level. [b] Experimental ^{1}H and ^{13}C chemical shifts for Lu(III) complex.

protons of the DTC exhibit the largest deshielding and shielding effects, respectively, with an isotropic shift of 2.7 ppm. In the ^{13}C spectrum, most of the carbons show rather large shielding or deshielding effects due to the paramagnetic centre i.e., Eu(III). The DTC carbons are highly deshielded with an isotropic shift of ca. 300 ppm while the PHEN carbons are (alternatively) either shielded or deshielded. Both methylene and methyl carbons are shielded by ca. 33 ppm and 3.8 ppm, respectively. At the "H-opt" geometry, the hybrid DFT functional PBE with 25% and 40% of exact-exchange were evaluated for the calculation of $\boldsymbol{A}$-tensor. It was found that using of DFT(PBE) for $\boldsymbol{A}$-tensor causes a large deviation in the chemical shifts of both ^{1}H and ^{13}C compared to DFT(PBE-xHF) methods. The improvements for HFC calculated using hybrid functionals over PBE are observed because the GGA functionals tend to underestimate the spin-polarisation of the metal s-type core-shells (2s, 3s, etc. for 4*f* centres), while hybrid functionals enhance them to almost correct values depending on the exact-exchange admixture. At "H-opt" geometry, the computed ^{13}C NMR chemical shifts well represent the experimental chemical shift values as well as the relative order of resonance lines on the ppm scale. However, some discrepancies were observed in the ^{1}H chemical shift order, especially, when the chemical shift difference between different protons was very small. There is a significant influence of the geometry on the calculated ^{1}H and ^{13}C chemical shifts. The full

geometry optimisation at the DFT/BP/COSMO level tends to somewhat twist the molecule, while the full optimisation of the geometry at DFT/PBE0-disp3/COSMO level only slightly changes the geometry. The calculated heavy atom root-mean-square deviation (RMSD) between the experimental and the former/latter structure was 0.40 Å/0.12 Å (see Fig. S13a in the ESI of Paper III). The calculated NMR shifts at DFT/BP/COSMO optimised geometry showed larger deviations from the experimental values as compared to those results obtained for the "H-opt" structure.

6.2.2 Nd(III) system (S=3/2)

The solution-state ^{1}H and ^{13}C NMR spectra of Nd(III) complex, with suggested resonance line assignments, are depicted in Figs. 12b and 13b, respectively. The total isotropic pNMR chemical shifts calculated for "H-opt" and "full-opt" geometries, with ***A***-tensor being calculated using PBE and PBE-xHF (x=25% or 40%) functionals, are given in Table 6. The ^{1}H NMR signals of all protons of Nd(III) complex are slightly broadened compared to the signals in the ^{1}H NMR spectrum of Eu(III) complex. Well-resolved signals for all inequivalent protons and carbons were observed; however, in both ^{1}H and ^{13}C NMR spectra, the relative

Table 7. Experimental solution-state and *ab initio* calculated ^{1}H and ^{13}C chemical shifts for Nd(III) complex.

Atoms	H-opt [a]	H-opt [b]	Full-opt [b,d]	H-opt [c]	Expt. (±0.01)
^{13}C Chemical shifts (ppm)					
C13,C18,C23	-163.1	14.5	-30.0	22.0	26.83
C31,C35	164.4	141.5	155.9	144.0	143.60
C32 ,C36	122.1	124.0	149.1	128.2	140.70
C29,C38	131.1	121.3	146.7	122.2	132.76
C30,C37	96.0	119.4	134.4	121.4	131.51
C33,C34	122.6	120.0	136.3	123.4	128.72
C28,C39	86.5	108.2	131.6	101.7	121.97
$-CH_2$	82.1	73.9	71.4	73.5	61.65
$-CH_3$	16.6	17.8	16.1	18.0	14.12
^{1}H Chemical shifts (ppm)					
H72,H75	13.4	6.3	11.6	6.4	8.96
H71,H76	10.2	5.9	9.6	3.5	8.39
H73,H74	3.0	2.7	10.2	3.7	7.69
H70,H77	33.2	19.9	15.4	1.7	6.17
$-CH_2$	8.4	8.1	6.9	7.7	5.55
$-CH_3$	4.9	5.1	3.4	5.0	1.65

[a] HFC/PBE/mDKS; [b] HFC/PBE0/mDKS; [c] HFC/PBE0-40HF/mDKS; [d] Geometry optimisation (DFT/DISP3/PBE-25HF/COSMO). For all above cases, the ***g***- & ***D***- tensors were calculated at the CASSCF level.

separation of PHEN resonance lines has decreased significantly compared to Eu(III) or the diamagnetic Lu(III) complex. Moreover, the chemical shift order of signals in both ^{1}H and ^{13}C NMR spectra differ from that of Eu(III) complex. For example, in contrast to Eu(III) complex, the isotropic shifts for H70/77 and H71/H76 were 3.6 ppm (shielding) and 0.7 ppm (deshielding), respectively. Both methylene and methyl protons were deshielded as compared to Eu(III) complex.

In contrast to the DTC carbon in the Eu(III) complex, which showed the largest hyperfine deshielding effect of ca. 508 ppm, the DTC carbon of Nd(III) complex experiences the largest hyperfine shielding effect of ca. 180 ppm, which results in a broad and low intense peak at 26.83 ppm. Furthermore, the respective PHEN carbons that were shielded in the Eu(III)-complex display deshielding effects in the Nd(III) complex. As with Eu(III) complex, almost similar effects of the chosen DFT method were observed on the structure optimisation of the Nd(III) complex. The heavy atom RMSD between experimental and DFT/BP/COSMO optimised structure was 0.25 Å, while for DFT/PBE0-disp3/COSMO structure it was 0.18 Å (see Fig. S13b in the ESI of Paper III). At the "H-opt" geometry, both ^{1}H and ^{13}C chemical shift calculations at the CASSCF/DFT(PBE) level show large discrepancies compared to those calculated at the CASSCF/DFT(PBE-xHF) level. As can be seen from Table 7, CASSCF/DFT(PBE-40% HF) calculations produce the best comparison with the experiments.

6.2.3 Yb(III) system (S=1/2)

The experimental ^{1}H and ^{13}C NMR spectra (solution in $CDCl_3$) of the Yb(III) complex with suggested atom-wise assignments are depicted in Figs. 12c and 13c. The experimental and *ab initio* calculated isotropic chemical shift data are provided in Table 8. In the ^{1}H NMR spectrum for Yb(III), the spread of resonance lines is significantly large (ca. 0-44 ppm). In comparison with the diamagnetic Lu(III) analogue, the ^{13}C signal corresponding to DTC (242.9 ppm) and one of the PHEN carbon (C28/39) (192.6 ppm) is significantly deshielded while all other PHEN and alkyl carbons are shielded. The chemical shift order of signals for both protons and carbons of PHEN ligand is different from that of both Eu(III) and Nd(III). The heavy atom RMSD between the experimental and optimised structures of the Yb(III)-complex with DFT/BP/COSMO was 0.25 Å whereas with DFT/PBE0-disp3/COSMO it was 0.08 Å (see Fig. S13c in the ESI of Paper III). The calculated ^{1}H and ^{13}C chemical shifts did not correspond to the experiments when the $\boldsymbol{A}$-tensor was calculated with GGA/PBE functional whereas using hybrid PBE functional with 25% exact-exchange greatly improved the results. An increase of the exact-exchange to 40% did not show any significant effect on the overall result.

Table 8. Experimental solution-state and *ab initio* calculated ^{1}H and ^{13}C chemical shifts for Yb(III) complex.

Atoms	H-opt [a]	H-opt [b]	Full-opt [b,d]	H-opt [c]	Expt. (±0.01)
^{13}C chemical shift assignments					
C13,C18,C23	193.0	287.9	220.6	286.1	242.86
C28,C39	156.4	195.6	189.3	197.4	192.60
C30,C37	138.8	137.2	49.7	139.5	138.24
C32,C36	175.3	120.0	96.4	120.3	124.07
C29,C38	126.9	129.5	116.2	129.1	123.89
C33,C34	133.3	121.3	116.2	121.6	121.91
C31,C35	139.6	118.4	85.6	119.0	118.57
$-CH_2$	73.8	47.8	35.6	42.9	41.31
$-CH_3$	13.1	11.5	3.2	11.9	11.70
^{1}H chemical shift assignments					
H70,H77	6.2	56.0	89.8	56.8	43.70
H71,H76	8.7	13.1	15.7	13.3	12.14
H72,H75	11.2	7.0	-2.7	6.9	7.32
H73,H74	11.5	4.1	2.8	4.0	5.25
$-CH_2$	7.3	0.7	1.3	0.4	2.44
$-CH_3$	2.0	0.5	0.5	0.5	0.41

[a] HFC/PBE/mDKS; [b] HFC/PBE0/mDKS; [c] HFC/PBE0-40HF/mDKS; [d] Geometry optimisation (DFT/DISP3/PBE-25HF/COSMO). For all above cases, the ***g***-tensors were calculated at the CASSCF level.

6.2.4 Er(III) system (S=3/2)

The experimental ^{1}H and ^{13}C NMR spectra (solution in $CDCl_3$) of the Er(III)-complex, showing atom-wise assignments, are depicted in Figs. 12d and 13d, respectively. The experimental and *ab initio* calculated isotropic chemical shift data are given in Table 9. The chemical shift spans for both ^{1}H (1-60 ppm) and ^{13}C (10-542 ppm) are significantly large. The DTC carbon is highly deshielded with an isotropic shift of ca. 340 ppm. The PHEN carbon chemical shifts are spread over ca. 135 ppm, whereas both methylene and methyl carbons display almost overlapped signals at ca. 10.6 and 10.5 ppm, respectively. Among the PHEN protons, H70/77 is highly deshielded with an isotropic shift of ca. 50 ppm, while the chemical shifts for all other PHEN protons, as the distance from the paramagnetic centre increases, gradually experience shielding effects. The *ab initio* calculated chemical shifts for PHEN ring atoms in the "full-opt" geometry do not correlate well with the experiments while the calculations with "H-opt" geometry at the same level of theory produce much better results. Except for methylene protons and carbons, the isotropic pNMR chemical shift calculations, with ***A***-tensor being calculated using hybrid functional PBE-40HF, provide the best agreement with the experiments.

Table 9. Experimental and *ab initio* calculated ^{1}H and ^{13}C chemical shifts for Er(III) complex.

Atoms	H-opt [a]	Full-opt [a,b]	H-opt [c]	Expt. (±0.01)
^{13}C Chemical shifts (ppm)				
C13,C18,C23	613.1	520.0	593.1	541.52
C28,C39	260.2	349.1	232.6	220.09
C30,C37	154.7	169.4	152.9	150.36
C33,C34	116.2	128.4	111.9	121.83
C29,C38	106.2	133.8	87.9	115.50
C32,C36	101.2	196.6	86.6	99.12
C31,C35	80.4	115.1	69.2	85.90
$-CH_2$	-3.8	21.9	13.8	10.65
$-CH_3$	-4.7	15	-4.0	10.52
^{1}H Chemical shifts (ppm)				
H70,H77	68.4	18.9	37.4	59.84
H71,H76	14.9	42.7	8.2	13.03
H72,H75	5.2	17.6	-0.2	5.83
H73,H74	2.7	7.9	-1.1	2.87
$-CH_2$	-12.1	4.1	4.3	2.43
$-CH_3$	-12.0	4.0	-12.7	1.45

[a] HFC/PBE0/mDKS; [b] HFC/PBE0-40HF/mDKS; [c] Geometry optimisation (DFT/DISP3/PBE-25HF/COSMO). For all above cases, the ***g***-tensors were calculated at the CASSCF level.

a)

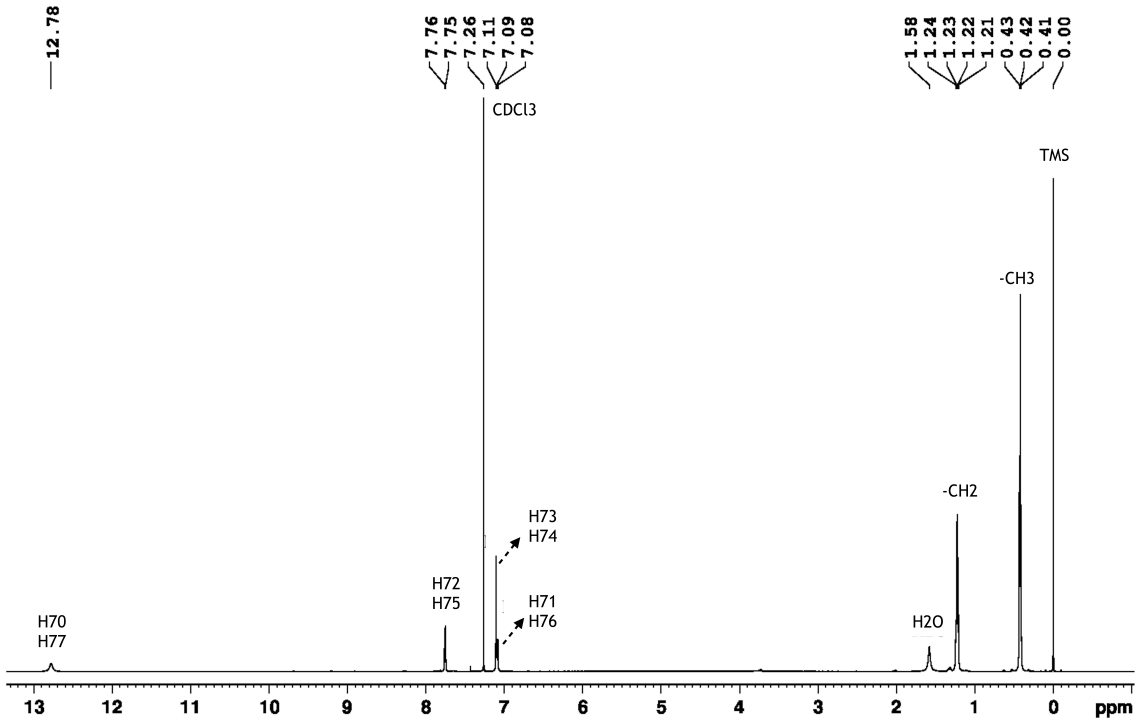
12.78
7.76
7.75
7.26
7.11
7.09
7.08
1.58
1.24
1.23
1.22
1.21
0.43
0.42
0.41
0.00
CDCl3
TMS
-CH3
-CH2
H73
H74
H72
H75
H71
H76
H70
H77
H2O
13
12
11
10
9
8
7
6
5
4
3
2
1
0
ppm

b)

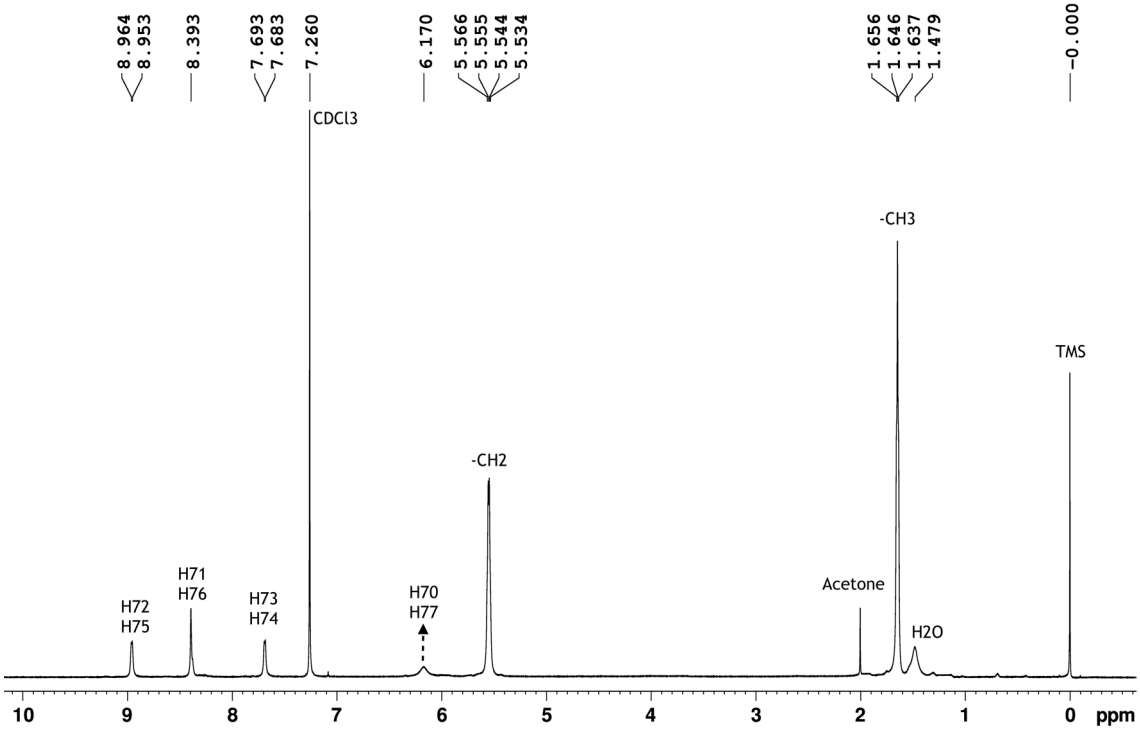
8.964
8.953
8.393
7.693
7.683
7.260
6.170
5.566
5.555
5.544
5.534
1.656
1.646
1.637
1.479
0.000
CDCl3
-CH3
TMS
-CH2
H71
H76
H72
H75
H73
H74
H70
H77
Acetone
H2O
10
9
8
7
6
5
4
3
2
1
0
ppm

c)

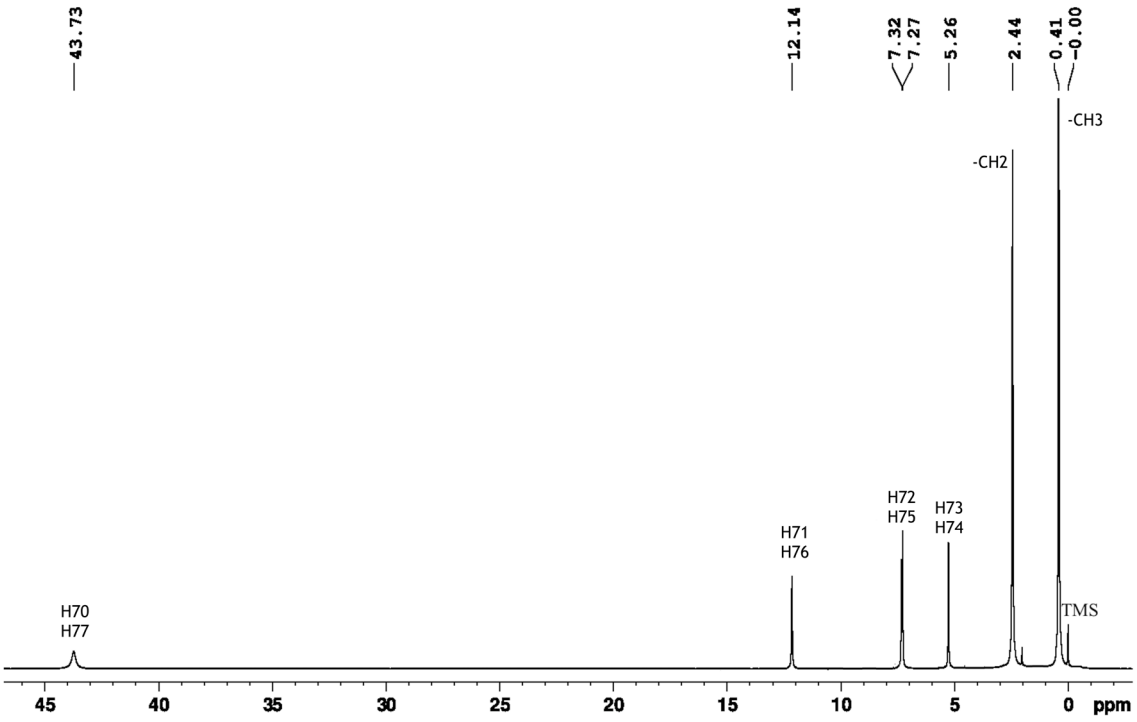

d)

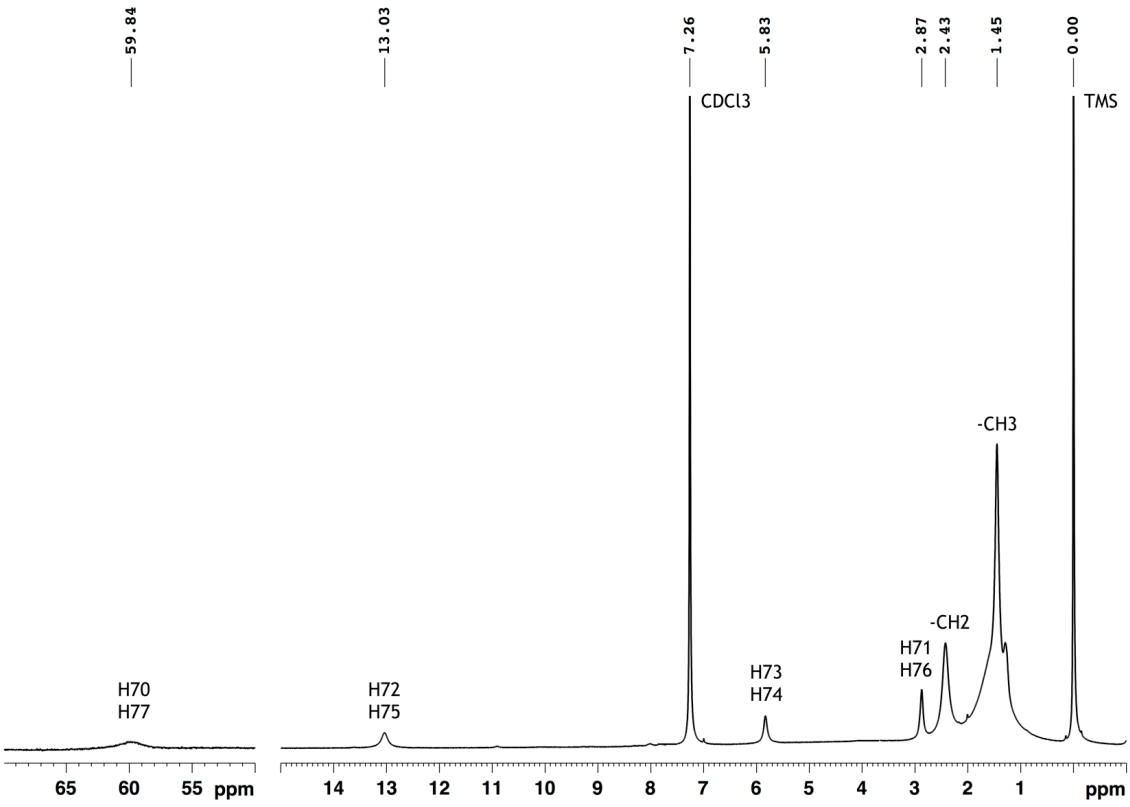

Fig. 12 ^{1}H NMR spectrum of Eu-DEDTC$_3$-PHEN (**a**), Nd-DEDTC$_3$-PHEN (**b**), Yb-DEDTC$_3$-PHEN (**c**), and Er-DEDTC$_3$-PHEN (**d**) complexes in $CDCl_3$ solution at 298 K. The atom-wise assignments are suggested.

a)

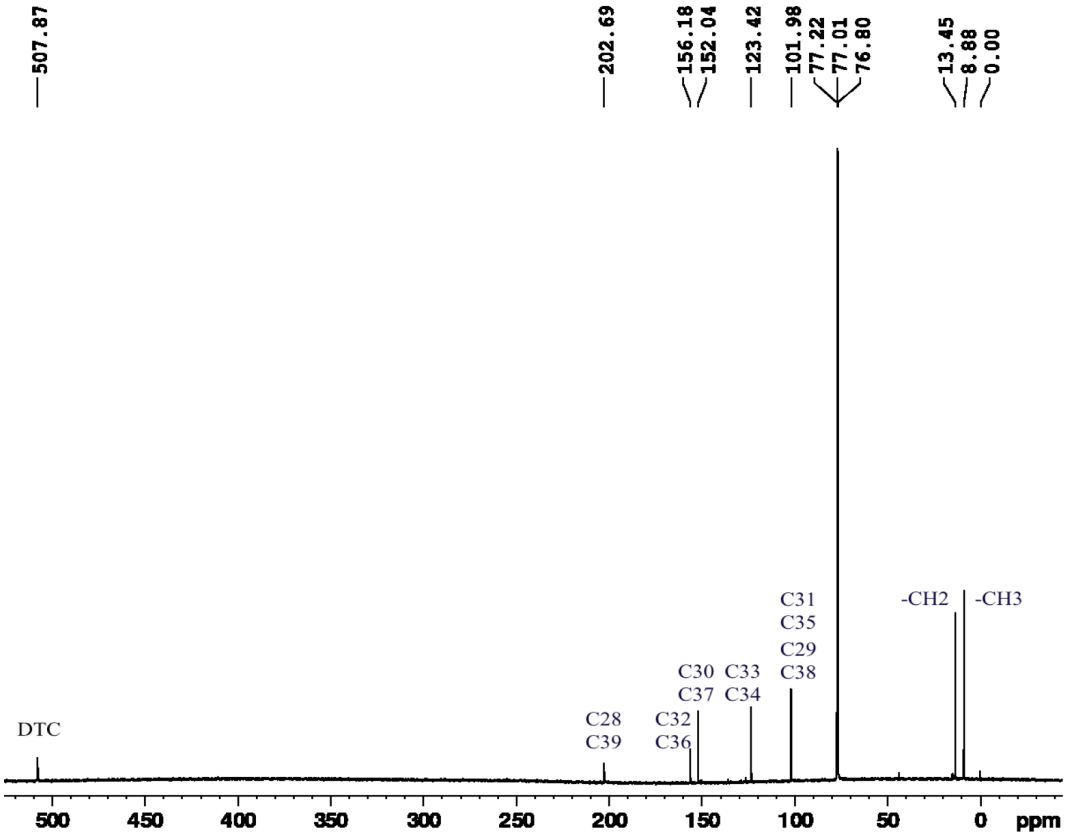
507.87
202.69
156.18
152.04
123.42
101.98
77.22
77.01
76.80
13.45
8.88
0.00
DTC
C28
C39
C32
C36
C30
C37
C33
C34
C31
C35
C29
C38
-CH2
-CH3
500
450
400
350
300
250
200
150
100
50
0
ppm

b)

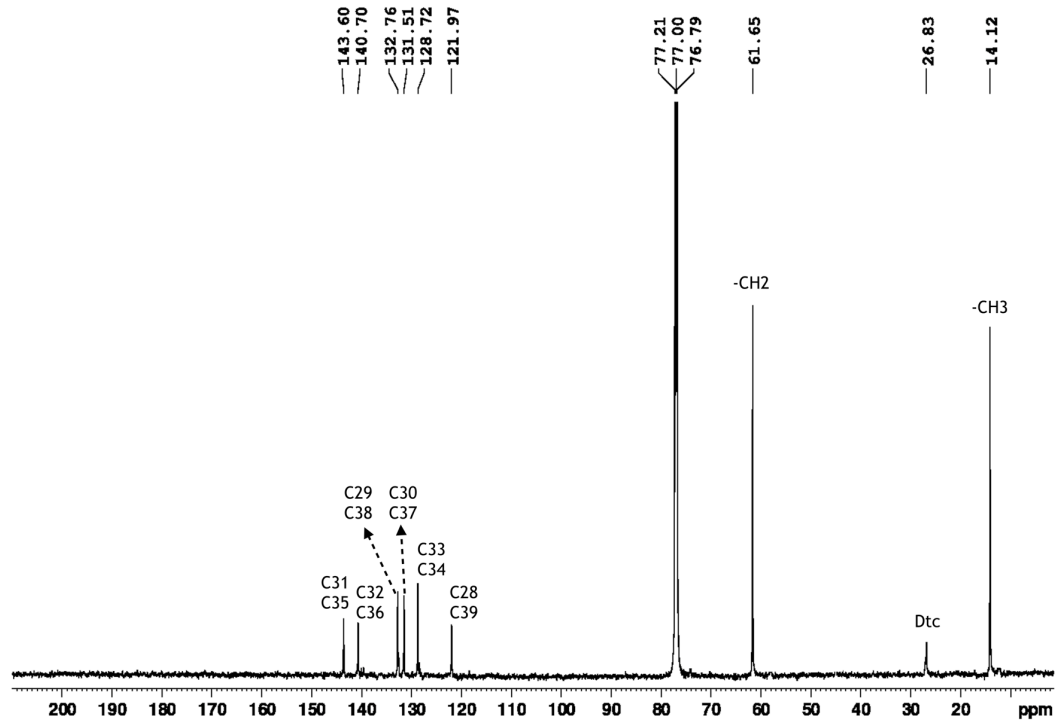
143.60
140.70
132.76
131.51
128.72
121.97
77.21
77.00
76.79
61.65
26.83
14.12
-CH2
-CH3
C29
C38
C30
C37
C33
C34
C31
C35
C32
C36
C28
C39
Dtc
200
190
180
170
160
150
140
130
120
110
100
90
80
70
60
50
40
30
20
ppm

c)

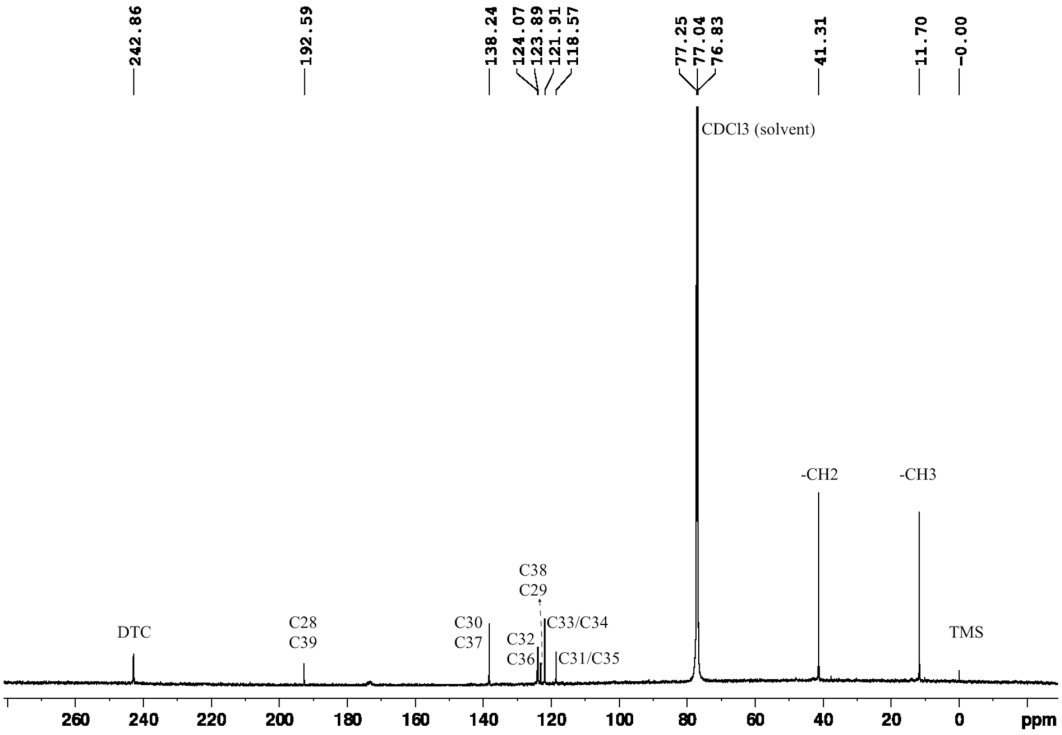

d)

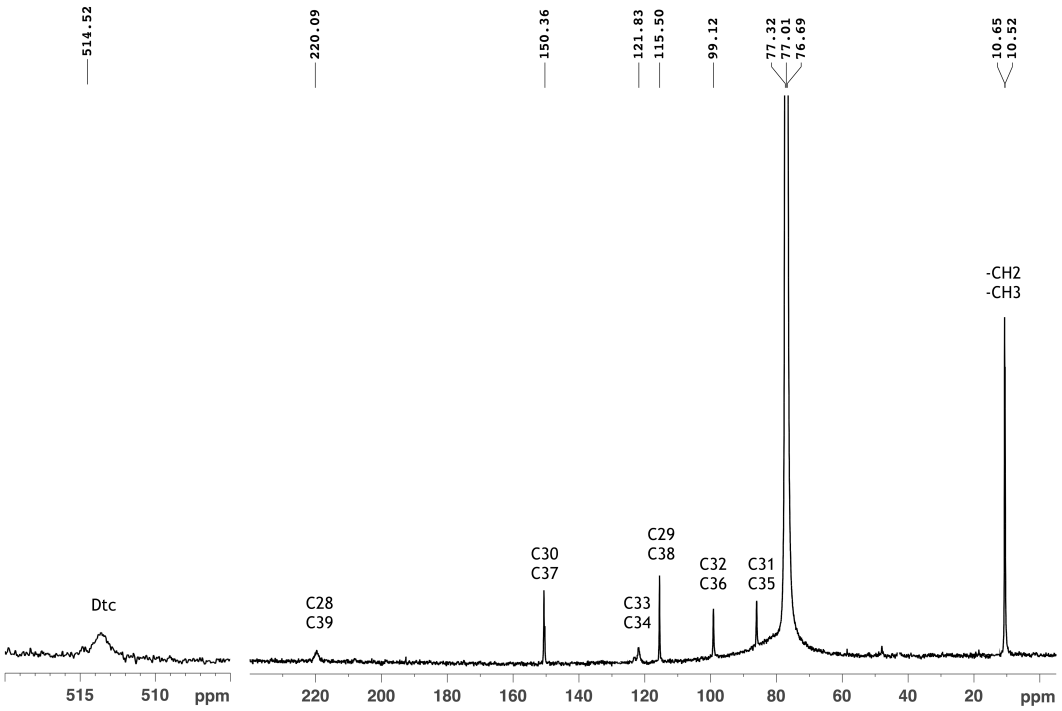

Fig. 13 ^{13}C-NMR spectra (^{1}H-decoupled) of Eu-DEDTC$_3$-PHEN (**a**), Nd-DEDTC$_3$-PHEN (**b**), Yb-DEDTC$_3$-PHEN (**c**), and Er-DEDTC$_3$-PHEN (**d**) complex in $CDCl_3$ solution at 298K.

6.2.5 Comparison between systems

The protons and carbons which are closest to the paramagnetic centre in both DEDTC and PHEN ligands experience the largest paramagnetic effect of the metal centres. It is common to all four systems studied here that the calculated isotropic chemical shifts are highly sensitive to the geometry and to the DFT functional used for the $\boldsymbol{A}$–tensor calculations. As can be seen from Table S2 in the ESI of Paper III, the values of $\boldsymbol{g}$-, $\boldsymbol{D}$-tensors as well as E/D values are also highly sensitive to the geometry of the complexes. For example, the CASSCF calculations of the Eu(III) complex resulted in a value of $\boldsymbol{D}$ equal to -12.9 cm^{-1} for "H-opt" geometry; however, when the structure was fully optimised at the DFT/PBE0-disp3/COSMO level a positive value for $\boldsymbol{D}$ (6.2 cm^{-1}) was obtained. As shown in Table S4 (ESI of Paper III), the large shielding or deshielding effect seen for the proton and carbon resonance lines can be analysed based on the physical contribution to the *ab initio*/DFT calculated chemical shifts. The orbital contribution (δ_{orb}) to the total isotropic shifts (refer Eq. 31) for the DTC carbons remain almost similar for all four systems. On the other hand, the δ_{con} contribution to the DTC carbons is large and positive for Eu(III) and Er(III), but negative for Nd(III) and Yb(III) complexes, respectively. Except for Er(III), the δ_{pc} contributions on the DTC carbons are very small. The δ_{con} and δ_{pc} contributions to most PHEN carbons and protons are notable as well.

6.3 Homoleptic and heteroleptic bismuth(III) DEDTC systems

In Paper IV, structure elucidation of a homoleptic Bi(III) complex with DEDTC as well as heteroleptic complexes of Bi(III) with DEDTC and PHEN or nitrate ligands, with empirical formulae: $[Bi\{S_2CN(C_2H_5)_2)\}_3]$ (**1**), $[Bi\{S_2CN(C_2H_5)_2)\}_2(NO_3)(PHEN)]$ (**2**), and $[Bi\{S_2CN(C_2H_5)_2)\}_3$ (PHEN)] (**3**) is discussed. The molecular structures of complexes (**1**) and (**2**) are depicted in Figs. 14a and 14b, respectively. The solid-state ^{13}C and ^{15}N CP-MAS NMR spectra are displayed in Figs. 15 and 16, respectively, while the experimental and DFT/GIPAW calculated chemical shifts are listed in Tables 10 (complex **1**) and 11 (complex **2**). The experimental NMR data and powder XRD patterns of both complexes are in accord with their single crystal structural data. For example, in the ^{13}C CP-MAS NMR spectrum of (**1**), DTC carbons resulted in two partially resolved ^{13}C resonance signals at 202.08 and 200.59 ppm with relative integrated intensities of 1:2 while the ^{15}N CP-MAS NMR signals resulted in three distinctive resonance signals over a range of 186-176 ppm with an integrated intensity ratio of 1:1:1, both clearly indicating that there are at least three inequivalent DTC ligands in the asymmetric part of the unit cell. Similarly, both ^{13}C and ^{15}N CP-MAS NMR spectra of (**2**) displayed two resonance lines corresponding to DTC sites, with an integrated intensity ratio of 1:1, suggesting the presence of at least two inequivalent DTC ligands in the asymmetric part of the unit cell. In addition, complex (**2**) displayed two ^{15}N resonance lines for PHEN nitrogen atoms and one for nitrate (NO_3^-). Single crystal structure of complex (**3**) is not known. However, based on the solution-state ^1H and ^{13}C NMR (see Figs. S4 and S5 in the ESI of Paper IV) and solid-state $^{13}C/^{15}N$ CP-MAS NMR (Figs. 15c and 16c) spectral data an attempt was made to formulate the possible arrangement of molecules in the asymmetric part of the

unit cell of complex (**3**). From the ^{1}H NMR, the PHEN to DEDTC ligand ratio was deduced to be 1:3. From the ^{13}C and ^{15}N CP-MAS spectra, the approximated integrated integral ratios of signals for DTC carbons (3:1:2) and nitrogens (1:1:1:3), both suggested the presence of at least six DEDTC ligands. This in turn indicated that the asymmetric unit cell of complex (**3**) had two inequivalent mononuclear $[Bi\{S_2CN(C_2H_5)_2\}_3(PHEN)]$ units.

The $^{13}C/^{15}N$ chemical shift calculations were carried out on both "H-opt" and "full-opt" structures for complexes (**1**) and (**2**). The ^{13}C and ^{15}N NMR chemical shift calculations for the "H-opt" structure qualitatively represented the experimental spectral pattern; however, the DEDTC ligands showed deviations in terms of the chemical shift range as well as the relative chemical shift difference between the inequivalent sites. On the other hand, the NMR calculations for the "full-opt" structures resulted in lower RMSD values and the linear regression plots between the experimental and calculated $^{13}C/^{15}N$ chemical shifts showed better agreements (R^2 close to unity) with the experimental values. The observed improvement of the GIPAW calculated NMR chemical shifts for the "full-opt" structure is most probably due to the converged forces on atoms, which were still rather large in the X-ray structure, indicating a non-equilibrium state of the system.

a) b)

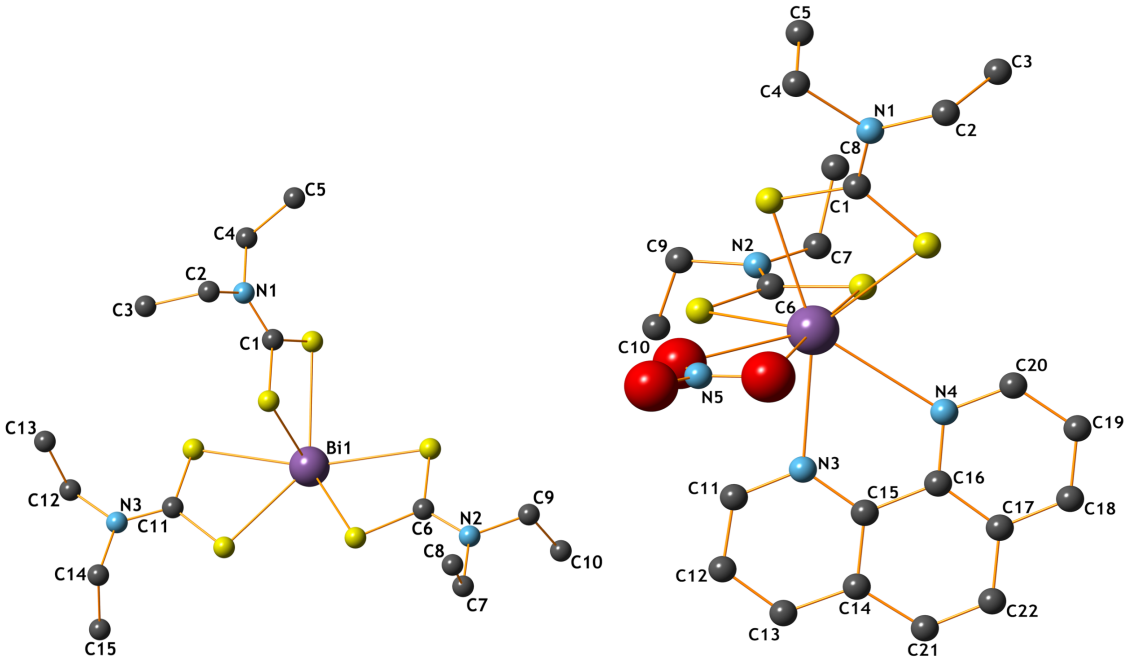

Fig. 14 Molecular structures of (**a**) complex (**1**) $[Bi\{S_2CN(C_2H_5)_2\}_3]$ and (**b**) complex (**2**) $[Bi\{S_2CN(C_2H_5)_2\}_2(NO_3)(PHEN)]$. H-atoms are omitted for clarity.

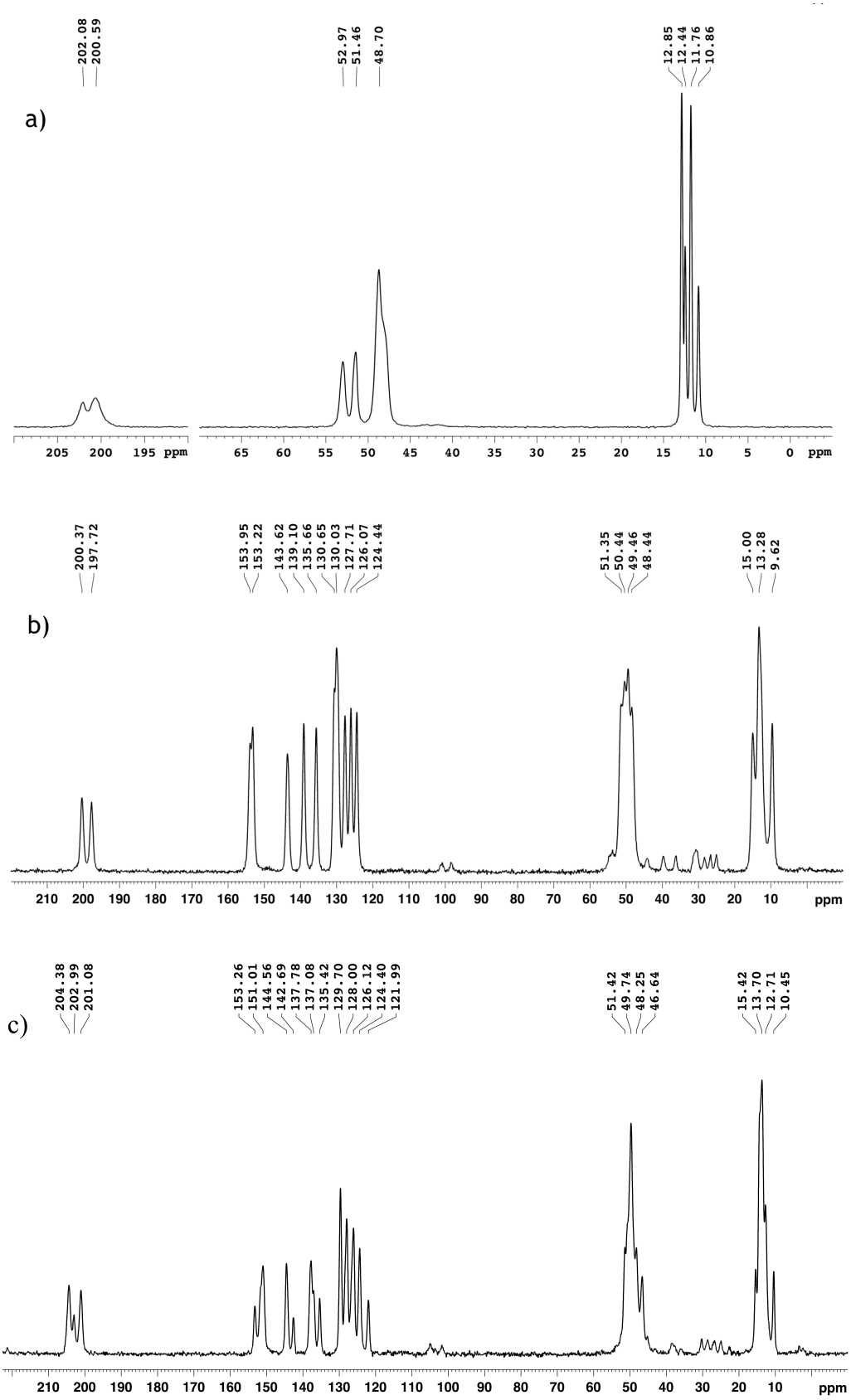

Fig. 15 ^{13}C CP-MAS NMR spectra of (**a**) complex (**1**) [Bi{$S_2CN(C_2H_5)_2$}$_3$], (**b**) complex (**2**) [Bi{$S_2CN(C_2H_5)_2$}$_2$(NO_3)(PHEN)], and (**c**) complex (**3**) [Bi{$S_2CN(C_2H_5)_2$}$_2$(PHEN)].

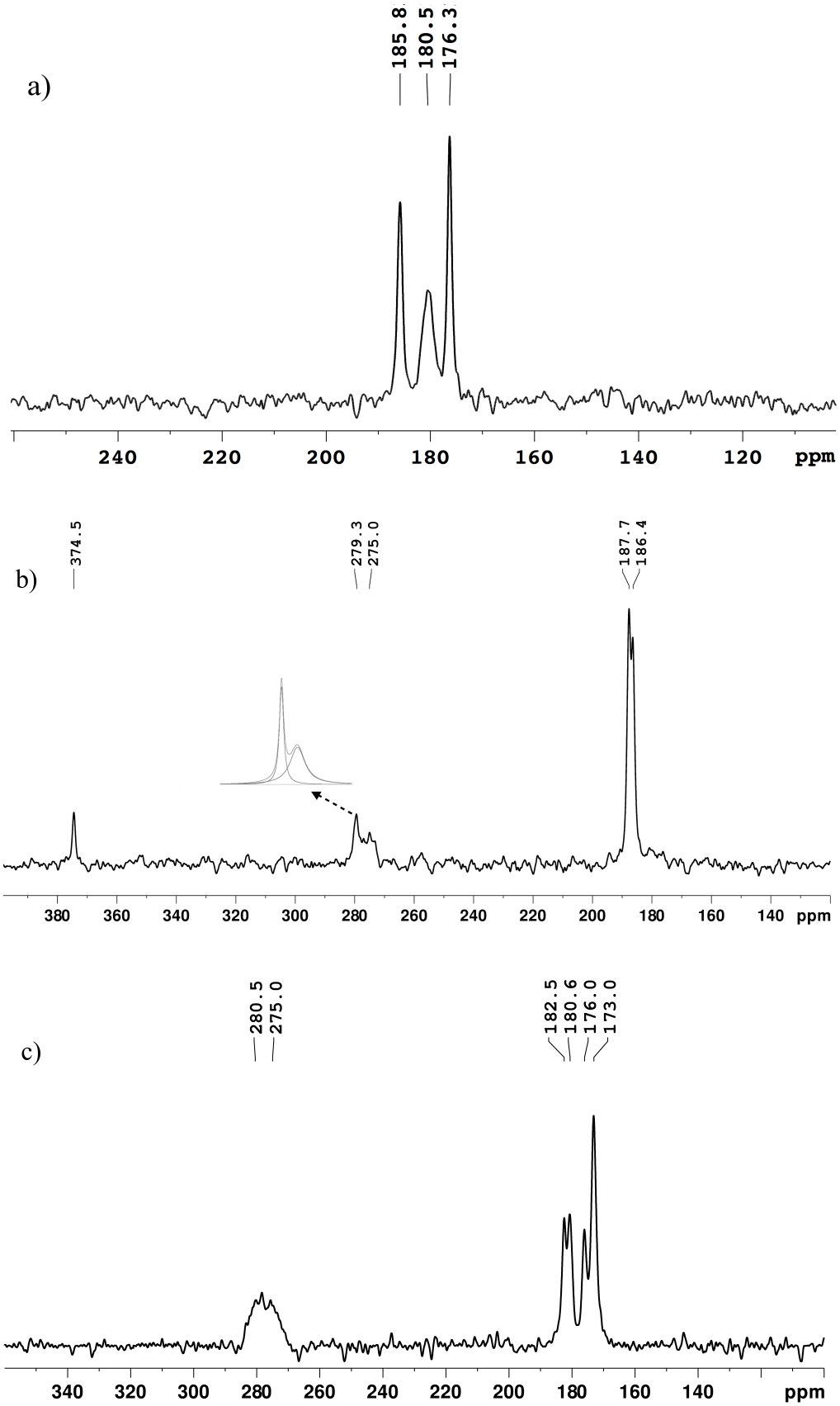

Fig. 16 ^{15}N CP-MAS NMR spectra of (**a**) complex (**1**) [Bi{$S_2CN(C_2H_5)_2$}$_3$], (**b**) complex (**2**) [Bi{$S_2CN(C_2H_5)_2$}$_2$(NO_3)(PHEN)], and (**c**) complex (**3**) [Bi{$S_2CN(C_2H_5)_2$}$_2$(PHEN)].

6.4 Polymorphism of ternary Bi(*n*-BuDTC)$_3$ complex

In Paper V, synthesis of two crystalline polymorphs of a binuclear bismuth(III) complex (polymorph I and polymorph II) with *n*BuDTC ligand and their characterisation by combined experimental (XRD and NMR) and structural and NMR chemical shift calculations by periodic DFT method are discussed. Both polymorphs have an empirical formula of [Bi{$S_2CN(n\text{-}C_4H_9)_2$}$_3$]. The observed packing polymorphism in these complexes results solvent dependent interactions between the mononuclear molecular units via secondary Bi···S bonds at the supramolecular level, yielding formation of binuclear [Bi_2{$S_2CN(n\text{-}C_4H_9)_2$}$_6$]. Polymorph I ($P\bar{1}$), obtained by recrystallisation from acetonitrile, contains two isomeric non-centrosymmetric binuclear molecules (Fig. 17a), while polymorph II ($P2_1/n$), obtained by recrystallisation from dichloromethane, exists as a single molecular form of the corresponding centrosymmetric binuclear formation (Fig 17b). Polymorph I contains four structurally inequivalent bismuth atoms and twelve inequivalent *n*BuDTC ligands, whereas polymorph II contains two structurally equivalent bismuth atoms and three structurally inequivalent *n*BuDTC ligands. Sun *et al.*[133] have reported a crystalline form of the compound (Fig. 17c) which resembles, but is not identical with, polymorph II.

Table 10. Experimental solid-state and GIPAW/PBE calculated ^{13}C and ^{15}N chemical shifts for complex (**1**).

	Atoms	H-opt	Full-opt	Expt. (±0.1)
^{13}C Chemical shifts (ppm)				
DTC	C11	203.5	203.3	202.1
	C1	199.5	202.7	200.6
	C6	197.9	202.5	200.6
-CH_2	C12	57.3	51.3	53.0
	C14	58.1	49.6	51.5
	C9	47.8	47.6	48.7
	C7	47.7	47.3	48.7
	C4	50.4	47.2	48.2
	C2	49.0	46.6	48.2
-CH_3	C8	11.7	11	12.8
	C10	10.0	9.3	12.8
	C13	7.9	8.5	12.4
	C3	7.9	8.5	11.8
	C5	9.3	7.7	11.8
	C15	7.2	6.3	10.9
	RMSD	3.3	2.9	
^{15}N Chemical shifts (ppm)				
DTC	N2	203.0	197.1	185.8
	N1	184.2	183.8	180.5
	N3	186.7	183.6	176.3
	RMSD	11.8	8.0	

Table 11. Experimental solid-state and GIPAW/PBE calculated ^{13}C and ^{15}N chemical shifts for complex (**2**).

	Atoms	H-opt	Full-opt	Expt. (±0.1)
^{13}C Chemical shifts (ppm)				
DTC	C1	196.1	202.9	200.4
	C6	199.5	201.0	197.7
PHEN	C11	155.8	157.3	153.9
	C20	156.7	156.4	153.2
	C15	146.5	145.9	143.6
	C16	139.7	145.4	139.1
	C13	138.5	143.4	135.7
	C18	132.8	138.0	130.6
	C21	128.5	133.9	130.0
	C14	130.9	132.3	130.0
	C22	125.1	132.3	130.0
	C17	121.1	131.8	127.7
	C12	123.0	127.7	126.1
	C19	123.0	126.3	124.4
$-CH_2$	C4	92.0	53.7	51.4
	C2	53.1	51.6	50.4
	C9	50.5	47.7	49.5
	C7	46.2	47.0	48.4
$-CH_3$	C5	12.3	12.2	15.0
	C3	11.5	9.4	13.3
	C8	8.3	9.2	13.3
	C10	3.7	5.1	9.6
	RMSD	9.4	3.9	
^{15}N Chemical shifts (ppm)				
$-NO_3$	N5	356.8	380.0	374.1
PHEN	N4	300.0	299.6	279.2
	N3	303.9	294.5	276.8
DTC	N1	240.1	188.3	187.7
	N2	188.4	186.0	186.4
	RMSD	29.1	12.4	

The experimental solid-state ^{13}C and ^{15}N CP-MAS NMR spectra of both polymorphs I and II are depicted in Figs. 18 and 19. Assignments of resonance lines in the solid-state ^{13}C and ^{15}N NMR spectra, assisted by chemical shift calculations at GIPAW method, are given in Tables 12 and 13. In the case of polymorph I, the DTC carbons resulted in six well resolved ^{13}C resonance signals with chemical shifts over a range of 200.2-206.1 ppm with an integrated intensity of 1:1:1:1:1:1 indicating the presence of at least six structurally inequivalent *n*BuDTC ligands in the unit cell. However, single crystal XRD structure revealed that there are, in total,

Table 12. Experimental and theoretical (GIPAW/PBE) ^{13}C and ^{15}N chemical shifts of polymorph I.

Sites	Labels [a]	H-opt [b]	Full-opt [b]	Expt. (±0.1)
^{13}C Chemical shifts				
DTC	C1, C82	205.4	207.5	206.1
(bridged)	C28, C73	203.6	205.3	205.4
DTC	C19, C100	204.1	203.7	202.3
(terminal)	C46, C55	201.8	202.8	201.4
	C37, C64	201.7	202.2	201.1
	C10, C91	198.2	200.6	200.2
-N-**C**H_2-	Avg.	56.0	54.8	54.5
-**C**H_2-CH_2-	Avg.	28.6	27.9	29.9
-**C**H_2-CH_3	Avg.	19.6	20.1	21.2
-**C**H_3	Avg.	12.5	12.8	15.1
RMSD [c]		1.6	1.3	
^{15}N Chemical shifts				
DTC	N2, N11	180.8	186.6	180.8
(terminal)	N3, N12	183.4	183.8	180.8
	N5, N8	175.0	182.1	180.2
	N6, N7	169.9	180.5	178.0
DTC	N1, N10	183.0	173.9	174.4
(bridged)	N4, N9	184.8	168.1	169.1
RMSD [c]		8.4	3.0	

[a] For atom labelling scheme, see Fig. 17a [b] The stated chemical shifts are averages of the calculated values for the two sites. [c] RMSD: Root-mean-square deviation between the experimental and calculated chemical shifts.

twelve inequivalent DTC ligands. The insufficient resolution in the NMR spectrum, however, prevents the observation of all the lines. In the ^{15}N CP-MAS NMR spectrum, five resonance signals with chemical shifts over a range of 169.1-180.8 ppm, having an integrated intensity ratio of 2:1:1:1:1, were observed, suggesting the presence of at least six inequivalent nitrogen sites in the *n*BuDTC ligands of the complex. On the contrary, both ^{13}C and ^{15}N CP-MAS spectra for the polymorph II are simpler, each showing only three resonance lines for DTC sites, with integrated intensity ratios of 1:1:1, indicating the presence of three inequivalent *n*BuDTC ligands. The ^{13}C and ^{15}N CP-MAS NMR data as well as the PXRD data (see Figs. 1a and 1b in Paper V) of polymorphs I and II agree well with their respective single crystal structural data.

Within the periodic DFT methods, the geometry of the crystal structures for polymorphs I, II, and II^s (Sun *et al.*)[133] were optimised by relaxing the positions of either only the H-atoms ("H-opt") or all atoms ("full-opt") with the outcome that the subsequent ^{13}C and ^{15}N NMR chemical shift calculations, using GIPAW approach, for the "full-opt" structures show excellent agreements (lower RMSD values) with experimental values, while the "H-opt" structures show larger deviations.

a)

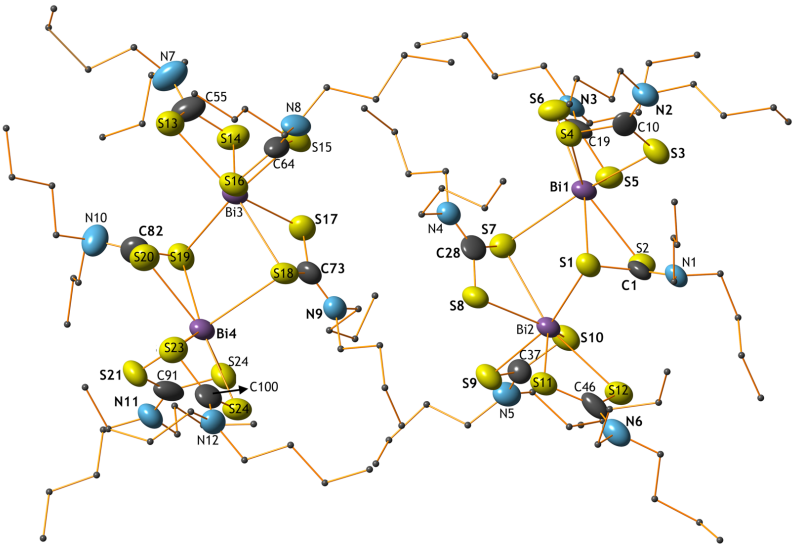

b)

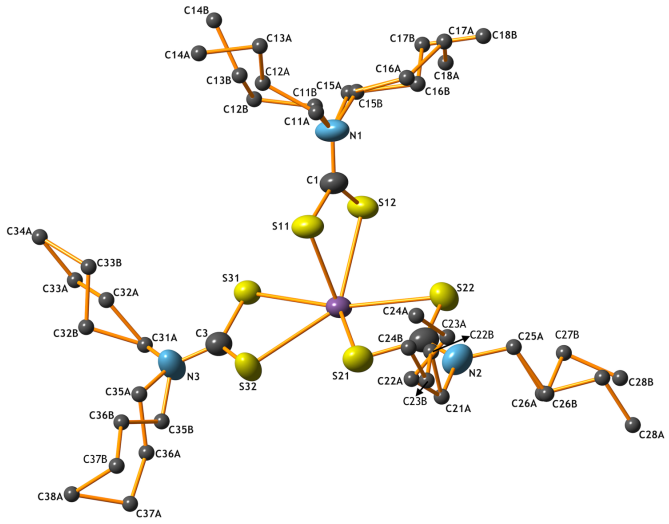

c)

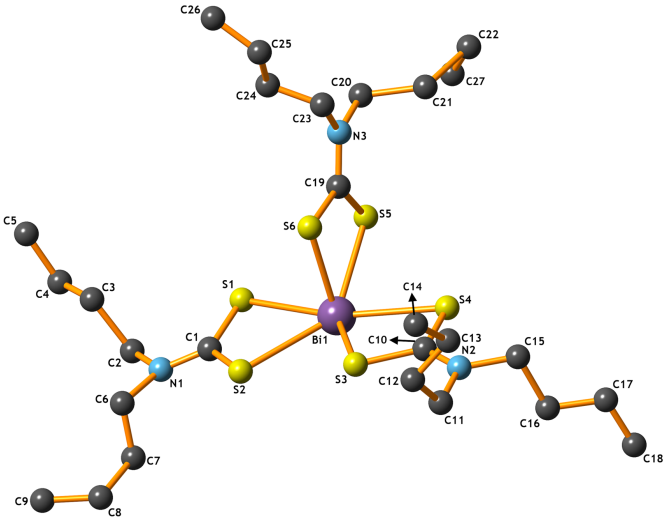

Fig. 17 Molecular structures of tris(di-*n*-butyldithiocarbamato)bismuth(III) complex, (**a**) polymorph I, (**b**) polymorph II, and polymorph II^{s} (**c**). H-atoms are omitted for clarity.

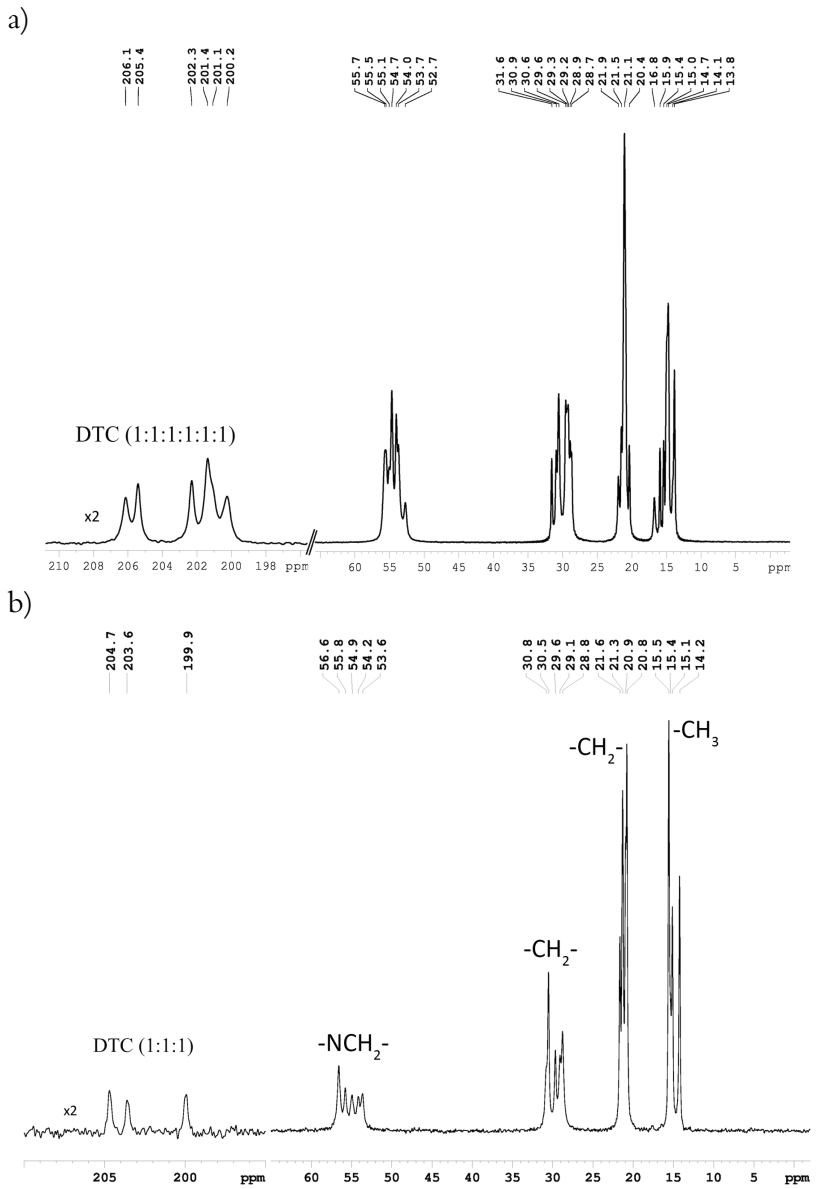

Fig 18. ^{13}C CP-MAS NMR spectra of polymorphs I (**a**) and II (**b**). For clarity, the intensities of the DTC signals are increased by a factor of 2.

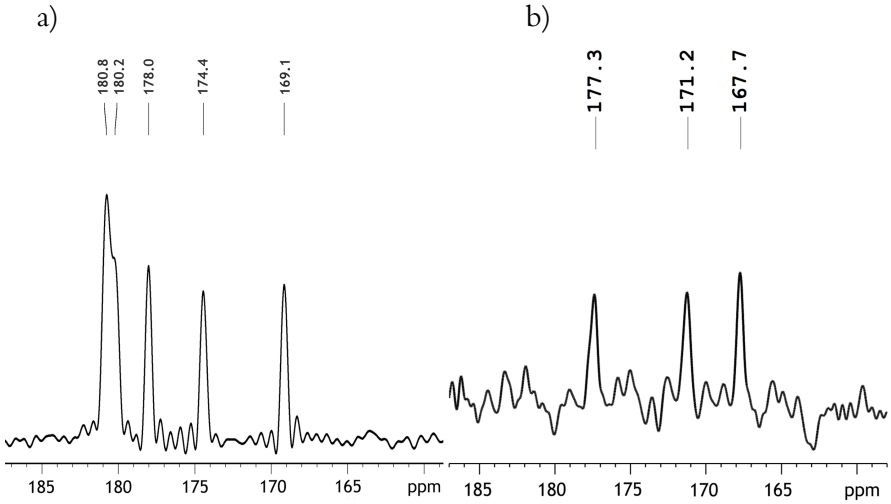

Fig 19. ^{15}N CP-MAS NMR spectra of polymorph I (**a**) and II (**b**).

Table 13. Experimental and theoretical (CASTEP/PBE) ^{13}C and ^{15}N chemical shifts for the polymorphs II and II^{s}.

Sites	Labels	H-opt[a]	Full-opt[a]	H-opt[b]	Full-opt[b]	Expt.[b] (±0.1)
^{13}C Chemical shifts						
DTC	C3	196.1	204.3	207.1	205.6	204.7
(Terminal)	C2	193.1	203.2	198.4	205.0	203.7
DTC	C1	191.4	199.9	196.7	201.3	200.0
(Bridged)						
-N-CH_2-	Avg.	55.7	55.7	57.7	56.7	55.0
-CH_2-CH_2-	Avg.	28.1	28.1	33.2	28.6	29.5
-CH_2-CH_3	Avg.	20.4	20.4	21.8	20.0	21.2
-CH_3	Avg.	14.4	14.4	15.3	14.1	15.1
RMSD[c]		6.1	0.8	3.1	1.2	-
^{15}N Chemical shifts						
DTC	N1	195.4	176.9	177.3	177.7	177.3
(Bridged)						
DTC	N3	172.6	175.0	170.1	175.8	171.2
(Terminal)	N2	157.3	169.8	163.5	169.9	167.7
RMSD[c]		12.7	2.5	3.3	2.9	-

[a] Polymorph II^{s} (Atom labelling scheme: C3=C1, C2=C10, C1=C19, N1=N3, N2=N2, and N3=N1, see Fig. 17c. [b] Polymorph II (For atom labelling scheme, see Fig. 17b) [c] RMSD: Root-mean-square deviation between the experimental and calculated chemical shifts.

A comparison of the calculated NMR chemical shifts for the "H-opt" structures of polymorphs II and II^{s} signify the structural differences between them. The DFT calculated bond parameters of the "full-opt" structures of polymorphs II and II^{s} are similar but not identical and close to the experimental bond parameters observed for polymorph II. In addition, all three *n*BuDTC ligands for polymorph II show conformational disorder, while the polymorph II^{s} does not report any such disorder. The resonance lines for DTC carbon and nitrogen atoms show some interesting patterns: the bridged DTC carbons are usually more deshielded while the terminal DTC carbons are more shielded and *vice versa* for the DTC nitrogen atoms. The ^{15}N chemical shifts are more sensitive to the subtle structural changes and show larger chemical shift range.

6.5 Comparisons of REE(III) and Bi(III) systems

The diamagnetic REE(III)s and Bi(III) complexes show some similarities as well as differences in terms of their stability, as well as structural and spectral properties. Ternary complexes of REE(III)s with DEDTC alone are least stable while analogous Bi(III) complexes are stable in both solution- and solid-state. However, inclusion of PHEN as a coordinating ligand increases the stability of the resulting heteroleptic REE(III) complexes to a large extent. Both DEDTC and *n*ButDTC ligands in Bi(III) complexes show intermolecular interactions via the weak

Bi···S bonds but the formation of heteroleptic complexes with PHEN ligand seems to hinder such intermolecular interactions in both Bi(III) and REE(III) systems. This is probably because the PHEN ligand fills the coordination void around the metal center while the coordination number increases to eight.

In the solution-state ^{1}H NMR spectra of the diamagnetic REE(III) complexes, the PHEN protons are more deshielded than in the corresponding Bi(III) systems. In the case of ^{13}C NMR spectra of diamagnetic REE(III) complexes, the signals for DTC carbons appear at ca. 206 ppm while for Bi(III) systems they appear at ca. 200 ppm, i.e. the DTC carbons in the latter systems are more shielded than in the former. This is probably due to the presence of a lone pair electrons and readily available outer *d*-orbitals for Bi ($d^{10}s^{2}$). The effect of inclusion of PHEN ligand on the chemical shift of DTC carbon in Bi(III) systems is negligibly small. However, it is difficult to observe such trends in the solid-state ^{13}C NMR spectra as the chemical shift range for DTC carbons appear between 200-208 ppm for both REE(III)s and Bi(III) systems.

7 Conclusions

NMR and X-ray diffraction experimental techniques have long been used for structural study of molecules and materials. Quantum mechanics and ready availability of supercomputers have facilitated calculations of electronic and molecular structure and properties of molecules from first principles. In this thesis, a combination of state-of-the-art experimental and theoretical methods were used to study structures and NMR properties of molecules and molecular crystals containing heavy atoms, such as REE(III)s and Bi(III). The presence of heavy atoms in these molecules result in relativistic and electron correlation effects, both of which influence on the NMR properties. Therefore, inclusion of relativistic corrections for NMR property calculation is recommended when treating such systems. Direct and significant effect of the structural changes on the magnetic resonance properties of the metal complexes were observed in all cases providing the framework of structure elucidation. This is of special interest for REEs because they are known to exhibit similar chemical and physical properties.

The diamagnetic REE(III)s and bismuth(III) complexes with DEDTC and PHEN ligands have all provided unique NMR fingerprint area around the metal centre both in liquid and solid phases. Periodic-DFT based framework was applied to get complementary and refined structural and NMR parameters, such as shielding constants and chemical shifts of all diamagnetic systems. The structural variations of Y(III) and La(III) complexes are thoroughly discussed in Papers I and II, respectively. The solid-state ^{13}C and ^{15}N NMR spectra of the diamagnetic REE(III) and bismuth(III) complexes were in accord with their structural data obtained by single crystal XRD. The relativistic contributions due to scalar (SR) and spin-orbit (SO) correlations for the calculated $^{1}H/^{13}C/^{15}N$ chemical shifts of diamagnetic REE complexes were analysed using two-component ZORA/DFT. The relativistic heavy atom (HA) effects on the NMR property of neighbouring light atoms (LA) or 'HALA effects' was found important mainly for the atoms which are closest to the metal centre. The isotropic chemical shifts calculated at the SR level already showed very good correlations with the experiments. The so-called 'crystal-lattice effects' on the NMR parameters were calculated by combining DFT calculations on molecular and periodic solid-state models. The absence of 'crystal-lattice effects' in ADF calculations of NMR parameters for molecular crystals found to decrease the chemical shift correspondence in crystallographically inequivalent atoms whereas the NMR calculations using GIPAW method, which takes into account of such solid-state effects, was found to reproduce the experimentally observed trends in the solid-state.

In Paper III, solution-state ^{1}H and ^{13}C NMR spectral patterns of selected paramagnetic REE(III) complexes were analysed. The experimental paramagnetic NMR (pNMR) chemical shifts, as well as the sizable difference of the ^{1}H and ^{13}C NMR shifts for the isoelectronic REE complexes, are well reproduced by the advanced calculations using *ab initio*/DFT approach. The accuracy of this approach is very promising for further applications to demanding pNMR problems involving paramagnetic *f*-block elements.

In Papers IV and V, solid-state ^{13}C and ^{15}N CP-MAS NMR, XRD, and periodic DFT methods were used to get complementary structural information of various bismuth(III) complexes, which were otherwise unattainable. For all solid-state NMR calculations in this

thesis, it was observed that the $^{13}C/^{15}N$ chemical shifts observed for "H-opt" structures show larger deviations from the experiments when compared to "full-opt" structures. The observed discrepancy was mainly due to the uncertainties in atomic positions from diffraction measurements as well as the large forces on atoms. The close-to-equilibrium structure is a prerequisite to get reasonable assignments of NMR spectra, as without vibrational averaging of modelled parameters it is the best approximation of the real (temperature) averaged structure corresponding to the experimentally observed NMR chemical shifts.

The results presented in this thesis demonstrate that a multidisciplinary approach of combined experimental NMR and XRD techniques along with computational modelling and property calculations is highly efficient in studying molecular complexes and solids containing heavy metal systems, such as rare-earths and bismuth.

References

1. Connelly, N.G., (Ed.) Elements, in *Nomenclature of Inorganic Chemistry: IUPAC recommendations 2005*, 51-52, Royal Society of Chemistry (2005).
2. Cornell, D. H. Rare earths from supernova to superconductor. *Pure Appl. Chem.* **65**, 2453-2464 (1993).
3. Klinger, J.M.A historical geography of rare earth elements: From discovery to the atomic age. *The Extractive Industries and Society,* **2**, 572-580 (2015).
4. Long, K.R., Van Gosen, B.S., Foley, N.K. & Cordier, D., The principal rare earth elements deposits of the United States: a summary of domestic deposits and a global perspective in *Non-Renewable Resource Issues* (Eds. Sinding-Larsen, R. & Wellmer, F.-W.), 131–155, Springer Netherlands (2012).
5. Voncken, J. H. L. in *The rare earth elements,* 53–72, Springer International Publishing, 2016).
6. E.U. Commission (2014), Report on critical raw materials for the EU. *Retrieved April*, *30* (2015)
   Available https://ec.europa.eu/growth/sectors/raw-materials/specific-interest/critical_en (Accessed on 25th Aug, 2017)
7. Blengini, G.A., Nuss, P., Dewulf, J., Nita, V., Peirò, L.T., Vidal-Legaz, B., Latunussa, C., Mancini, L., Blagoeva, D., Pennington, D. and Pellegrini, M., E.U. methodology for critical raw materials assessment: Policy needs and proposed solutions for incremental improvements. *Resour. Policy* **53**, 12-19 (2017).
8. Golev, A., Scott, M., Erskine, P. D., Ali, S. H. & Ballantyne, G. R. Rare earths supply chains: Current status, constraints and opportunities. *Resour. Policy* **41,** 52–59 (2014).
9. King, A. H., Eggert, R. G. & Gschneidner, K. A. The rare earths as critical materials, in *Handbook on the Physics and Chemistry of Rare Earths* **50,** 19–46, Elsevier (2016).
10. Gosen, B. S. V., Verplanck, P. L., Long, K. R., Gambogi, J. Robert, R., & Seal, I. I. The rare-earth elements: vital to modern technologies and lifestyles. US Geological Survey (2014).
11. Jha, A. R. *Rare Earth Materials: Properties and Applications*, CRC PRess Inc. 1-331, (2014).
12. Ye, S., Xiao, F., Pan, Y. X., Ma, Y. Y., & Zhang, Q. Y. Phosphors in phosphor-converted white light-emitting diodes: Recent advances in materials, techniques and properties. *Mater. Sci. Eng. Rep.*, *71*(1), 1-34 (2010)
13. Xie, F., Zhang, T. A., Dreisinger, D. & Doyle, F. A critical review on solvent extraction of rare earths from aqueous solutions. *Miner. Eng.* **56,** 10–28 (2014).
14. Liu, Y., Cao, Y., Huang, L., Gao, M. & Pan, H. Rare earth–Mg–Ni-based hydrogen storage alloys as negative electrode materials for Ni/MH batteries. *J. Alloys Compd.,* **509**(3), 675-686 (2011).
15. Alonso, E., Sherman, A. M., Wallington, T. J., Everson, M.P., Field, F.R., Roth, R. & Kirchain, R.E., Evaluating rare earth element availability: A case with revolutionary demand from clean technologies. *Env. Sci. Tech.* **46**, 3406-3414 (2012).

16. Preinfalk, C. & Morteani, G., Industrial applications of rare earth elements, in *Lanthanides, Tantalum and Nniobium: Mineralogy, Geochemistry, Characteristics of Primary Ore Deposits, Prospecting, Processing and Applications Proceedings of a workshop in Berlin, November 1986.* Vol. 7. (Eds. Möller, P., Černý, P. & Saupé, F.) 359–370, Springer Science & Business Media (2013).
17. Goonan, T. G. Rare earth elements: End use and recyclability. No. 2011-5094, US Geological Survey (2011).
Available http://pubs.usgs.gov/sir/2011/5094/ (Accessed on 25th Aug 2017).
18. Bleiwas, D.I., Potential for recovery of cerium contained in automotive catalytic converters: *U.S. Geological Survey Open-File Report* (2013). Available http://digitalcommons.unl.edu/usgspubs/114/ (accessed on 25th Aug 2017).
19. Sadeghbeigi, R. *Fluid catalytic cracking handbook: An expert guide to the practical operation, design, and optimization of FCC units* (Elsvier Inc. 2012).
20. Mineral commodity summaries, US Geological Survey, 32-33 (2009).
21. Ojebuoboh, F. K. Bismuth—Production, properties, and applications. *J. Min. Met. Mater.* **44,** 46–49 (1992).
22. Naumov, A. V. World market of bismuth: A review. *Russ. J. Non-Ferr Met.* **48**, 10-16 (2007).
23. Yang, Y., R., Xu, L., Guo, N., Li, W., Feng, K., & Miao, Y. Bismuth complexes: synthesis and applications in biomedicine. *J. Coord. Chem.* **68,** 379–397 (2015).
24. Jordens, A., Cheng, Y. P. & Waters, K. E. A review of the beneficiation of rare earth element bearing minerals. *Miner. Eng.* **41,** 97–114 (2013).
25. Gupta, C. K., and N. Krishnamurthy. Extractive metallurgy of rare earths. *Int. Mater. Rev.* **37** (1) 197-248 (1992).
26. Rare earth elements profile-British geological survey, (2011).
Available https://www.bgs.ac.uk/downloads/start.cfm?id=1638 (Accessed on 25th Aug 2017)
27. Chakhmouradian, A. R. & Wall, F. Rare earth elements: minerals, mines, magnets (and more). *Elements* **8,** 333–340 (2012).
28. Chen, Ji, (ed.) *Application of Ionic Liquids on Rare Earth Green Separation and Utilization*, 3-85, Springer (2015).
29. Izatt, S. R., McKenzie, J. S., Izatt, N. E., Bruening, R. L., Krakowiak, K. E., & Izatt, R. M. Molecular recognition technology: a green chemistry process for separation of individual rare earth metals, in *White Paper on Separation of Rare Earth Elements*, 1-13 (February 20, 2016).
30. Binnemans, K., Jones, P. T., Blanpain, B., Van Gerven, T., Yang, Y., Walton, A., & Buchert, M. Recycling of rare earths: a critical review. *J. Clean. Prod.*, **51**, 1-22 (2013).
31. Schüler, D., Buchert, M., Liu, R., Dittrich, S., & Merz, C. Study on rare earths and their recycling. *Öko-Institut eV Darmstadt*, 1-162 (2011).
Available http://resourcefever.eu/publications/reports/Rare%20earths%20study_Oeko-Institut_Jan%202011.pdf (Accessed on 25th Aug 2017).

32. Tanaka, M., Oki, T., Koyama, K., Narita, H., & Oishi, T. (2012). Recycling of rare earths from scrap, in the *Handbook on the physics and chemistry of rare earths* (Eds. Bunzli J.-C.G. and Pecharsky, V.K.), **43**, 159-204 (2012).
33. He, D., Yang, J., Tang, C., Chen, Y. & Tang, M. Separation of Bismuth From a Bismuth Glance Concentrate Through a Low-Temperature Smelting Process. *Min. Proc. Ext. Met. Rev.* **34,** 73–80 (2013).
34. Krenev, V. A., Drobot, N. F., & Fomichev, S. V. Processes for the recovery of bismuth from ores and concentrates. *Theor. Found. Chem. Eng.*, **49**(4), 540-544 (2015).
35. Huang, C. H. (Ed.) *Rare earth coordination chemistry: fundamentals and applications*. (John Wiley & Sons, Ltd. 2010).
36. Garje, S. S. & Jain, V. K. Chemistry of arsenic, antimony and bismuth compounds derived from xanthate, dithiocarbamate and phosphorus based ligands. *Coord. Chem. Rev.* **236,** 35–56 (2003).
37. Shannon, R. D. Revised effective ionic radii and systematic studies of interatomic distances in halides and chalcogenides. *Acta. Cryst. A* **32,** 751–767 (1976).
38. Binnemans, Koen. Rare-earth beta-diketonates, in the *Handbook on the physics and chemistry of rare earths* (Eds. Gschneidner, K.A., Bunzli J.-C.G., and Pecharsky, V.K.) **35**, 107-272 (2005)
39. Ren J., Wang W., Luo J., Zhou G., Tang F., Progress of flotation reagents of rare earth minerals in China. *J. Rare Earth.*, **21**(1) 1-8, (2003).
40. Nakamura, S. & Suzuki, N. A new trend in the synergistic extraction of rare-earth (III) complexes with various β-diketones and 1,10-phenanthroline. *Polyhedron,* **5**, 1805-1813 (1986).
41. Singh, D.K., Singh, H. & Mathur, J. N. Extraction of rare earths and yttrium with high molecular weight carboxylic acids. *Hydrometallurgy,* **81(**3*),* 174-181 (2006).
42. Tabushi, I., Kobuke, Y., Nakayama, N., Aoki, T. & Yoshizawa, A. Chelating resin functionalized with dithiocarbamate for the recovery of uranium from seawater. *Ind. Eng. Chem. Prod. Res. Dev.* **23,** 445–448 (1984).
43. Lewis, F.W., Harwood, L.M., Hudson, M.J., Drew, M.G., Desreux, J.F., Vidick, G., Bouslimani, N., Modolo, G., Wilden, A., Sypula, M., & Vu, T.H., Highly efficient separation of actinides from lanthanides by a phenanthroline-derived bis-triazine ligand. *J. Am. Chem. Soc.* **133,** 13093–13102 (2011).
44. Hardwick, W.H. & Moreton-Smith, M. The determination of uranium by solvent extraction. Part I. The separation of uranium-233 from irradiated thorium as the diethyldithiocarbamate complex. *Analyst,* **83,** 9-13 (1958).
45. Pyykko, P. Relativistic effects in structural chemistry. *Chem. Rev.* **88,** 563–594 (1988).
46. Kaupp, M., L. Malkina, O., G. Malkin, V. & Pyykkö, P. How do spin–orbit-induced heavy-atom effects on NMR chemical shifts function? validation of a simple analogy to spin–spin coupling by density functional theory (DFT) calculations on some iodo compounds. *Chem. Eur. J.* **4,** 118–126 (1998).
47. Pyykkö, P., Görling, A. & Rösch, N. A transparent interpretation of the relativistic contribution to the NMR "heavy atom chemical shift." *Mol. Phys.* **61,** 195–205 (1987).

48. Bučinský, L., Jayatilaka, D. & Grabowsky, S. Importance of relativistic effects and electron correlation in structure factors and electron density of diphenyl mercury and triphenyl bismuth. *J. Phys. Chem. A* **120,** 6650–6669 (2016).
49. Atkins, P. W. & Friedman, R. S. *Molecular Quantum Mechanics*. (OUP Oxford, 2011).
50. Raghavachari, K., & Anderson, J. B. Electron correlation effects in molecules. *J. Phys. Chem.,* **100**(31), 12960-12973 (1996).
51. Sinha, S. P., (Ed.) Systematics and the Properties of the Lanthanides. **109**, Springer Science and Business Media, (2012).
52. Martineau, C., Cadiau, A., Bouchevreau, B., Senker, J., Taulelle, F., & Adil, K. SMARTER crystallography of the fluorinated inorganic–organic compound $Zn_3Al_2F_{12}$·$[HAmTAZ]_6$. *J. Chem. Soc., Dalton Trans.* **41,** 6232–6241 (2012).
53. Ashbrook, S. E. & McKay, D. Combining solid-state NMR spectroscopy with first-principles calculations - a guide to NMR crystallography. *Chem. Comm.* **52,** 7186–7204 (2016).
54. Harris R.K., Wasylishen R.E., Duer, M.J., (Eds.) NMR Crystallography, Wiley: Chichester (2009).
55. Harris, R. K. NMR crystallography: the use of chemical shifts. *Solid State Sci.* **6,** 1025–1037 (2004).
56. Lenthe, E.V., Baerends, E.-J. & G. Snijders, J. Relativistic regular two-component Hamiltonians. *J. Chem. Phys.* **99,** 4597–4610 (1993).
57. Lenthe, E.V., Snijders, J. G. & Baerends, E. J. The zero-order regular approximation for relativistic effects: The effect of spin–orbit coupling in closed shell molecules. *J. Chem. Phys.* **105,** 6505–6516 (1996).
58. Joyce, S. A., Yates, J. R., Pickard, C. J. & Mauri, F. A first principles theory of nuclear magnetic resonance *J*-coupling in solid-state systems. *J. Chem. Phys.* **127,** 204107 (2007).
59. J. Pickard, C. & Mauri, F. All-electron magnetic response with pseudopotentials: NMR chemical shifts. *Phys. Rev. B* **63,** 245101 (2001).
60. Clark, S. J. *et al.* First principles methods using CASTEP. *Z. Kristallogr. Crysta. Mater.* **220,** (2005).
61. R. Yates, J., J. Pickard, C. & Mauri, F. Calculation of NMR chemical shifts for extended systems using ultrasoft pseudopotentials. *Phys. Rev. B* **76,** 024401 (2007).
62. Kerridge, A. The complete-active-space self-consistent-field approach and its application to molecular complexes of the *f*-elements, in the *Computational Methods in Lanthanide and Actinide* (Ed. Michael D.), John Wiley & Sons (2015).
63. Barysz, M. & Sadlej, A. J. Two-component methods of relativistic quantum chemistry: from the Douglas–Kroll approximation to the exact two-component formalism. *J. Mol. Struct-Thermochem.* **573,** 181–200 (2001).
64. Pantazis, D. A. & Neese, F. All-Electron Scalar Relativistic Basis Sets for the Lanthanides. *J. Chem. Theory Comput.* **5,** 2229–2238 (2009).
65. Komorovsky, S., Repisky, M., Ruud, K., L. Malkina, O. & G. Malkin, V. Four-component relativistic density functional theory calculations of NMR shielding tensors

for paramagnetic systems. *J. Phys. Chem. A* **117,** 14209–14219 (2013).
66. Gohr, S., Hrobárik, P., Repisky, M., Komorovsky, S., Ruud, K., & Kaupp, M. Four-component relativistic density functional theory calculations of EPR *g*- and hyperfine-coupling tensors using hybrid functionals: validation on transition-metal complexes with large tensor anisotropies and higher-order spin-orbit effects. *J. Phys. Chem. A* **119,** 12892–12905 (2015).
67. Atkins, P. (Ed.) *Shriver and Atkins' inorganic chemistry*. Oxford University Press, USA, (2010).
68. Harris, K.D.M., Tremayne, M. & Kariuki, B. M. Contemporary Advances in the Use of Powder X-Ray Diffraction for Structure Determination. *Angew. Chem. Int. Ed. Engl.* **40,** 1626–1651 (2001).
69. Rietveld, H. A profile refinement method for nuclear and magnetic structures. *J. Appl. Crystallogr.*, **2**(2), 65-71 (1969)
70. Harris, K. D. M. & Tremayne, M. Crystal Structure Determination from Powder Diffraction Data. *Chem. Mater.* **8,** 2554–2570 (1996).
71. Suryanarayana, C. & Norton, G. M. *X-Ray Diffraction: A Practical Approach*. Springer Science & Business Media (1998).
72. Levitt, M. H. (Ed.) *Spin dynamics: basics of NMR*. Wiley, New York (2008).
73. Keeler, J. (Ed.) *Understanding NMR spectroscopy*. John Wiley & Sons, (2011).
74. Duer, M. J. (Ed.). *Solid state NMR spectroscopy: principles and applications*. John Wiley & Sons (2008).
75. La Mar, G. N., Horrocks, W. D., & Holm, R. H. (Eds.) *NMR of paramagnetic molecules: principles and applications*. Elsevier (2016).
76. Rdpmeester, J. A. Application of solid state ^{13}C NMR to the study of polymorphs, clathrates and complexes. *Chem. Phys. Lett.*, **74**(3), 536-538 (1980).
77. Mathias, L. J. (Ed.) *Solid state NMR of polymers*. Springer Science & Business Media (2013).
78. Brown, S. P. Applications of high-resolution 1 H solid-state NMR. *Solid State Nuc. Mag. Reson.*, **41**, 1-27 (2012).
79. Hatfield, G. R., & Carduner, K. R. (1989). Solid state NMR: Applications in high performance ceramics. *J. Mater. Sci.*, **24**(12), 4209-4219 (1989).
80. Roberts, G., & Lian, L. Y. (Eds.). *Protein NMR spectroscopy: practical techniques and applications*. John Wiley & Sons (2011).
81. Bakhmutov, V. I. (Ed.) *Solid-State NMR in Materials Science: Principles and Applications*. CRC Press Inc. (2011).
82. Harris, R. K. Applications of solid-state NMR to pharmaceutical polymorphism and related matters. *J. Pharma. Pharmacol.*, **59**(2), 225-239 (2007).
83. Hartmann, S. R., & Hahn, E. L. Nuclear double resonance in the rotating frame. *Phys. Rev.*, **128**(5), 2042 (1962).
84. Haeberlen, U., *High resolution NMR in Solids Selective Averaging: supplement 1 advances in magnetic resonance*. **1**, Elsevier (1976).
85. Mehring, M. (Ed.) High resolution NMR Spectroscopy in Solids, in the *NMR basic*

principles and progress, (Eds. Diehl, E., Fluck, E., Kosfeld, R.), **11**, Berlin Heidelberg-New York, Springer (1976).
86. Andrew, E. R., Bradbury, A., & Eades, R. G. Removal of dipolar broadening of nuclear magnetic resonance spectra of solids by specimen rotation. *Nature*, **183**(4678), 1802-1803 (1959).
87. Pines, A., Gibby, M. G. & Waugh, J. S. Proton-enhanced nuclear induction spectroscopy. A method for high resolution NMR of dilute spins in solids. *J. Chem. Phys.* (1972).
88. Schrödinger, E. An undulatory theory of the mechanics of atoms and molecules. *Phys. Rev.*, **28**(6), 1049 (1926).
89. Negele, J. W. & Orland, H. *Quantum many-particle systems*. Westview (1988).
90. Born, M., & Oppenheimer, J. R. *Ann. Physik.* **84** 458 (1927). in English by Blinder S.M., On the quantum theory of molecules (1998). http://www.chm.bris.ac.uk/pt/manby/papers/bornop.pdf (Accessed on 25th Aug. 2017)
91. Atkins, P. W. & Friedman, R. S. *Molecular Quantum Mechanics*. OUP Oxford (2011).
92. Cramer, C. J. *Essentials of computational chemistry: theories and models*. John Wiley & Sons (2013).
93. Kohn, W. & Sham, L. J. Self-consistent equations including exchange and correlation effects. *Phys. Rev.* **140,** A1133–A1138 (1965).
94. Nakajima, T., Yanai, T. & Hirao, K. Relativistic electronic structure theory. *J. Comput. Chem.* **23,** 847–860 (2002).
95. Reiher, M. & Wolf, A. *Relativistic Quantum Chemistry: The Fundamental Theory of Molecular Science*. John Wiley & Sons (2014).
96. Dyall, K. G. & Jr, F. K. *Introduction to Relativistic Quantum Chemistry*. Oxford University Press (2007).
97. Rösch, N., Matveev, A., Nasluzov, V. A., Neyman, K. M., Moskaleva, L., & Krüger, S. Quantum chemistry with the Douglas-Kroll-Hess approach to relativistic density functional theory: Efficient methods for molecules and materials. *Theor. Comput. Chem.*, **14**, 656-722 (2004).
98. Chang, C., Pelissier, M. & Durand, P. Regular two-component Pauli-like effective Hamiltonians in Dirac theory. *Physica Scripta* **34,** 394 (1986).
99. Møller, C. & Plesset, M. S. Note on an approximation treatment for many-electron systems. *Phys. Rev.* **46,** 618–622 (1934).
100. Knowles, P. J., Andrews, J. S., Amos, R. D., Handy, N. C., & Pople, J. A. Restricted Møller—Plesset theory for open-shell molecules. *Chem. Phys. Letters*, *186*(2-3), 130-136. (1991).
101. Helgaker, T., Jorgensen, P., & Olsen, J. *Molecular electronic-structure theory*. John Wiley & Sons (2014).
102. Bartlett, R. J. & Musiał, M. Coupled-cluster theory in quantum chemistry. *Rev. Mod. Phys.* **79,** 291–352 (2007).
103. Olsen, J. The CASSCF method: A perspective and commentary. *Int. J. Quantum Chem.* **111,** 3267–3272 (2011).

104. Dolg, M. (Ed.) *Computational Methods in Lanthanide and Actinide Chemistry*. John Wiley & Sons (2015).
105. Lenthe, E.V., & Baerends, E.J. Optimized Slater-type basis sets for the elements 1–118. *J. Comput. Chem.*, **24**(9), 1142-1156 (2003).
106. Velde, G.T., Bickelhaupt, F.M., Baerends, E.J., Fonseca Guerra, C., van Gisbergen, S.J., Snijders, J.G., & Ziegler, T. Chemistry with ADF. *J. Comput. Chem.* **22**(9), 931-967 (2001).
107. Kaupp, M., Michael, B. & Malkin, V. G. (Eds.) *Calculation of NMR and EPR parameters: theory and applications*. Wiley-VCH Verlag GmbH & Co. KGaA (2006).
108. Grunenberg J. (Ed.) *Computational Spectroscopy: Methods, Experiments and Applications*. John Wiley & Sons (2011).
109. Moon, S. and Patchkovskii, S. First-principles calculations of paramagnetic NMR shifts, in *Calculation of NMR and EPR Parameters: Theory and Applications* (Eds. M. Kaupp, M. Bühl and V. G. Malkin), Wiley-VCH Verlag GmbH & Co. KGaA, Weinheim, FRG. (2004).
110. Kurland, R. J. & McGarvey, B. R. Isotropic NMR shifts in transition metal complexes: The calculation of the Fermi contact and pseudocontact terms. *J. Magn. Reson.* **2,** 286–301 (1970).
111. Vaara, J., Awais Rouf, S. & Mareš, J. Magnetic couplings in the chemical shift of paramagnetic NMR. *J. Chem. Theor. Comput.* **11,** 4840–4849 (2015).
112. Rouf, S. A., Mareš, J. & Vaara, J. ^{1}H Chemical shifts in paramagnetic Co(II) pyrazolylborate complexes: A first-principles study. *J. Chem. Theor. Comput.* **11,** 1683–1691 (2015).
113. Cherry, P. J., Rouf, S. A. & Vaara, J. Paramagnetic enhancement of nuclear spin-spin coupling. *J. Chem. Theor. Comput.* **13,** 1275–1283 (2017).
114. Brown, E. Bloch electrons in a uniform magnetic field. *Phys. Rev.* **133,** A1038–A1044 (1964).
115. Monkhorst, H. J. & Pack, J. D. Special points for Brillouin-zone integrations. *Phys. Rev. B* **13,** 5188–5192 (1976).
116. Blöchl, P. E. Projector augmented-wave method. *Phys. Rev. B* **50,** 17953–17979 (1994).
117. Yates, J. R., Pickard, C. J. & Mauri, F. Calculation of NMR chemical shifts for extended systems using ultrasoft pseudopotentials. *Phys. Rev. B* **76,** 024401(2007).
118. Regulacio, M. D., Tomson, N. & Stoll, S. L. Dithiocarbamate precursors for rare-earth sulfides. *Chem. Mater.* **17,** 3114–3121 (2005).
119. Yin, H. D., Hong, M. & Wang, C. H. Synthesis and crystal structures of bismuth(III) complexes with dithiocarbamate $[Bi(S_2CNEt_2)_3]_2$ and $[Bi(S_2CNC_4H_8)_2(NO_3)]$. *Ind. J. Chem. A* **44** (07)1401-1405 (2005).
120. Raston, C. L., G. L. Rowbottom, and A. H. White. Synthesis and crystal structure of the mixed-quadriligand bismuth complex $[Bi(S_2CNEt_2)_2(NO_3)\cdot$[1,10-Phen]. *J. Chem. Soc., Dalton Trans.* **6**, 1352-1359 (1981).
121. Sheldrick, G. M. SADABS: Program for performing absorption corrections to single-

crystal X-ray diffraction patterns, *University of Göttingen, Göttingen, Germany (2002)*.
122. Sheldrick, G. M. A short history of SHELX. *Acta Crystallographica Section A: Foundations of Crystallogrphy* **64**, *112-122* (2008).
123. Spek, A. L. Single-crystal structure validation with the program PLATON. *J. Appl. Crystallogr.* (2003).
124. Varand, V. L., Glinskaya, L. A., Klevtsova, R. F. & Larionov, S. V. Synthesis and crystal and molecular structure of mixed-ligand compounds $Eu(S_2CN(C_2H_5)_2)_3$ (2,2′-Bipy) and $Eu(S_2CN(C_2H_5)_2)_3$(1,10-Phen). *J. Struct. Chem.* **39,** 244–252 (1998).
125. Kuz'mina, N. P., Ivanov, R. A., Ilyukhin, A. B. & Paramonov, S. E. Crystal structure of tris(diethyldithiocarbamato)ytterbium complex o-phenanthroline. *Russ. J. Coord. Chem.* **25,** 635–638 (1999).
126. Ahlrichs, R., Armbruster, M.K., Bachorz, R.A., Bär, M., Baron, H.P., Bauernschmitt, R., Bischoff, F.A., Böcker, S., Crawford, N., Deglmann, P. & Sala, F.D.,TURBOMOLE 6.5, Universität Karlsruhe, (2009).
127. Pye, C. C., Ziegler, T., Lenthe, E.V., & Louwen, J. N. An implementation of the conductor-like screening model of solvation within the Amsterdam density functional package—Part II. COSMO for real solvents. *Canad. J. Chem.*, **87**(7), 790-797 (2009).
128. Pye, C. C., & Ziegler, T. An implementation of the conductor-like screening model of solvation within the Amsterdam density functional package, in the *Theoretical Chemistry Accounts: Theory, Computation, and Modeling. Theor. Chim. Acta*, **101**(6), 396-408 (1999).
129. Frisch, M.J., Trucks, G.W., Schlegel, H.B., Scuseria, G. E., Robb, M.A., Cheeseman, J. R., Scalmani, G., Barone, V., Petersson, G.A., Nakatsuji, H., Li, X., Caricato, M., Marenich, A., Bloino, J., Janesko, B.G., Gomperts, R., Mennucci, B., Hratchian, H.P., Ortiz, J.V., Izmaylov, A.F., Sonnenberg, J.L., Williams-Young, D., Ding, F., Lipparini, F., Egidi, F., Goings, J., Peng, B., Petrone, A., Henderson, T., Ranasinghe, V.G., Zakrzewski, D., Gao, J., Rega, N., Zheng, G., Liang, W., Hada, M., Ehara, M., Toyota, K., Fukuda, R., Hasegawa, J., Ishida, M., Nakajima, T., Honda, Y., Kitao, O., Nakai, H., Vreven, T., Throssell, K., Montgomery, J.J.A., Peralta, J.E., Ogliaro, F., Bearpark, M., Heyd, J.J., Brothers, E., Kudin, K.N., Staroverov, V.N., Keith, T., Kobayashi, R., Normand, J., Raghavachari, K., Rendell, A., Burant, J.C., Iyengar, S.S., Tomasi, J., Cossi, M., Millam, J.M., Klene, M., Adamo, C., Cammi, R., Ochterski, J.W., Martin, R.L., Morokuma, K., Farkas, O., Foresman, J.B., & Fox, D.J., *Gaussian 09, revision D. 01*, Gaussian, Inc., Wallingford CT (2009).
130. Neese, F. The ORCA program system. *WIREs Comput. Mol. Sci.* **2,** 73–78 (2012).
131. Komorovsky, S., Repisky, M., Ruud, K., L. Malkina, O. & G. Malkin, V. Four-component relativistic density functional theory calculations of NMR shielding tensors for paramagnetic systems. *J. Phys. Chem. A* **117,** 14209–14219 (2013).
132. Regulacio, M.D., Pablico, M.H., Vasquez, J.A., Myers, P.N., Gentry, S., Prushan, M., Tam-Chang, S.W. and Stoll, S.L., Luminescence of Ln(III) dithiocarbamate complexes (Ln= La, Pr, Sm, Eu, Gd, Tb, Dy). *Inorg. Chem.*, **47**(5), 1512-1523 (2008).
133. Sun, R.-Z., Guo, Y.-C., Liu, W.-M., Chen, S.-Y. & Feng, Y.-Q. Syntheses, Crystal

Structures and Antibacterial Activities of Complexes [$(C_9H_{18}NS_2)_3$ M (III)](M= Sb and Bi), *Chin. J. Struct. Chem.* **31**, 655-660 (2012).

134. Van Gaal, H.L.M., Diesveld, J.W., Pijpers, F.W. & Van der Linden, J.G.M., ^{13}C NMR spectra of dithiocarbamates. Chemical shifts, carbon-nitrogen stretching vibration frequencies and π bonding in the NCS_2 fragment. *Inorg. Chem.*, **18**(11), 3251-3260 (1979).
135. Ivanov, A.I. & Antzutkin, O.N., Natural abundance ^{15}N and ^{13}C CP/MAS NMR of dialkyldithiocarbamate compounds with Ni(II) and Zn(II), In *New Techniques in Solid-State NMR* (Ed. Klinowski, J.), *Top. Curr. Chem.,* **246**, 271-337, Springer Berlin Heidelberg (2005).